University of Zurich[UZH]

Analysis of Multi-Track Backscatter Time Series for Cryospheric Applications and their Feasibility for Snow Depth Classification

GEO 610 Master's Thesis

Author
Gwendolyn Dasser
15-729-700

Supervised by
Dr. David Small
Dr. Hendrik Wulf

Faculty representative
Prof. Dr. Alexander Damm

30.03.2021
Department of Geography, University of Zurich

University of Zurich[UZH]

GEO 610 – Specialized Master Thesis

Analysis of Multi-Track Backscatter Time Series for Cryospheric Applications and their Feasibility for Snow Depth Classification

Author:
Gwendolyn Dasser
student-ID: 15-729-700
gwendolyn.dasser@uzh.ch

Supervisor:
Dr.
David Small

Faculty Representative:
Prof. Dr.
Alexander Damm-Reiser

Co-Supervisor:
Dr.
Hendrik Wulf

March 30, 2021

A thesis submitted for the degree of

Specialized Master in Remote Sensing

Department of Geography, University of Zürich

Abstract

Understanding the spatio-temporal behaviour of snow cover enables informed decisions concerning water resource management, risk assessment and hydroelectric power production. Information on snow cover plays an important role in weather and climate research. In this study, we work toward improving the identification of wet snow areas and the retrieval of snow depth using Local Resolution Weighting (LRW) radar composites. Created from Sentinel-1A and -1B Radiometrically Terrain Corrected (RTC) backscatter products, they offer high spatial and temporal resolution. For a test site in the Bernese Alps, the composites acquired within periods ranging from 36 hours to six days are used to generate wet snow maps. The homogeneity of such LRW composites is examined by assessing slope dependency of the time series of snow covered image samples. By including optical imagery featuring snow extent and a temperature data set, we test new approaches for generating an optimal dry winter reference image for the use in Synthetic Aperture Radar (SAR) wet snow detection. Benefits as well as limitations of current LRW composites are discussed, when validating their use for wet snow classification in mountainous terrain. By applying the method by Lievens et al. (2019), we assess the method's feasibility to detect snow depths on high spatial (1000 to 30 m) and temporal (6 days) resolution. Validation was performed by using external reference information (liquid water content maps for wet snow retrieval and snow water equivalent for snow depth retrieval). Results indicated the usage of LRW composites and γ° convention to offer major improvements for cryospheric applications. Further research could assess the impact of signal to noise ratio at even higher resolution composites (10 m) and strive for the physical explanation between snow depth and Sentinel-1 backscatter.

Acknowledgments

The generous support of several people allowed this thesis to evolve. First and foremost, I would like to thank Dr. David Small for his dedicated supervision. His valuable expert feedback supported me in letting this thesis take form. I thank Dr. Hendrik Wulf for co-piloting my studies and for guiding my attention towards snow depth retrieval and thereby disclosing a whole new, fascinating chapter in my studies. I also thank Dr. Hans Lievens for taking the time to answer my questions and provide me with scripts which enabled me to compile intercomparisons.

I would like to express my appreciation to Isabelle Helfenstein and Marius Rüetschi. Isabelle supported me while developing a scientifically structured thesis and provided invaluable assistance to mastering my studies. Marius was always available for intriguing discussions on the fascinating topic of remote sensing of the cryosphere. During such meetings with Isabelle and Marius, whether these were in person or via telecon, I would always be encouraged on my path in research and find my motivation and scientific drive renewed.

Furthermore, I thank the unification of coffee-machines, allowing all those flexible coffee-breaks with my dear friends at the University, which have - repeatedly - made my days throughout the course of my studies. I highly appreciated the coffee-talks with Dr. Elias Mendez, who's esteemed availability, in case of any arousing question, helped me in making these first steps on the path of scientific research.

Last but not least, I would like to express my gratitude to my family, who have not only enabled my studies, but were also of valuable support during my process of learning. Especially, I thank my mother for her continuous and cherished assistance to improve my English skills and for the corresponding proofreading. Here, as part of my family, Tobias and Tanja deserve special appreciation: Tanja, for her continuing readiness to listen and provide some thoughts on my endless soliloquies concerning my studies and Tobias, for being so patient and calming in times of pressure.

Glossary

Acronyms

CLC	CORINE Land Cover
DEM	Digital Elevation Model
EoC	Error of Commission
EoO	Error of Omission
EPSG	European Petroleum Service Group
GSD	Ground Sampling Distance
GTC	Geometrical Terrain Correction
IMIS	Intercantonal Measurement and Information System
IW	Interferometric Wide swath mode
JIM	JULES Investigation Model
LiDAR	Light Detection And Ranging
LRW	Local Resolution Weighting
LWC	Liquid Water Content
MODIS	Moderate Resolution Imaging Spectroradiometer
OA	Overall Accuracy
RADAR	Radio Detection And Ranging
RI	Reference Image
RTC	Radiometric Terrain Correction
S1	Sentinel-1
SD	Snow Depth
SAR	Synthetic Aperture RADAR
SC	Snow Cover
SWE	Snow Water Equivalent
TCD	Tree Cover Density
TmaxD	Daily maximum Temperature
VH	Cross-polarization mode: Vertically polarized signal transmitted, Horizontally polarized received
VH/VV	Cross-polarization ratio: VH - VV [dB] polarization difference
VV	Co-polarization mode: Vertically polarized signal transmitted, and Vertically polarized received

Organizations

Copernicus	Europe's eyes on Earth: Land monitoring service by the European Union
ESA	European Space Agency
ExoLabs	Earth observation solutions
GLAMOS	Swiss glacier inventory
NASA	National Aeronautics and Space Administration
MeteoSwiss	Swiss federal office of meteorology and climatology
SLF	WSL institute for snow and avalanche research
swisstopo	Swiss federal office of topography
WSL	Swiss federal institute for forest, snow and landscape research

Projections and Geometries

The projection conventions summarized here are described in chapter 2.2, illustrated in Fig. 2.3 and defined following Small (2011).

β	RADAR backscatter coefficient
β°	RADAR brightness, backscatter with reference area defined in the slant range plane
σ°_E	Backscatter with reference area defined tangent to a local ellipsoid based ground model
γ°_E	Backscatter with ellipsoid-based reference area defined perpendicular to the line of sight
γ°_T	Terrain-flattened backscatter with reference area defined perpendicular to the line of sight: Radiometric terrain (RTC) corrected backscatter
γ°_c	Composite backscatter with reference area defined perpendicular to the line of sight: Weighted sum of contributing RTC backscatter values

Contents

List of Figures

List of Tables

1 Introduction

1.1 Motivation

Understanding the spatio-temporal behaviour of snow cover can enable informed decisions concerning water resource management, risk assessment and hydroelectric power production (Wendleder et al., 2018; Nagler et al., 2018; Dietz et al., 2012). Snow's high albedo strongly influences the Earth's energy balance. Multiple studies have indicated an indirect impact of snow cover on the atmospheric circulation (Seager et al., 2010). Observing changes in snow cover over time is therefore crucial for climate change mitigation strategies (Lyu et al., 2017; Wendleder et al., 2018; Dietz et al., 2012) and promises to enable advancements in numerical weather prediction. Knowledge of the spatial distribution of snow depth is of major relevance for avalanche risk assessment and accurate run-off modelling.

Synthetic Aperture Radar (SAR) has been claimed to offer a promising approach to monitor large scale cryospheric environments (Truckenbrodt et al., 2019; Arslan, 2006). It has already been successfully applied (e.g. Nagler et al., 2018; Jäger, 2016; Small, 2012). Being independent of daylight and not restricted by weather conditions, SAR also offers high temporal resolution. In applications of radar backscatter (e.g. forest observation), wet snow cover can lead to spurious signals due to its strong dielectric characteristic (Rüetschi et al., 2019). Accurate knowledge of snow extent, snow melt, occurrence and depth allows one to mitigate such artifacts.

1.2 Current state of research

Pure, fresh snow typically reflects a high proportion of light in the visible (VIS) spectrum, resulting in its albedo reaching up to 90% (Dietz et al., 2012). Reflectance of snow decreases significantly within the infrared frequency spectrum (Singh et al., 2010). This contrast allows to distinguish snow from other land cover classes using optical sensors (Lillesand et al., 2015). However, space-borne optical snow detection approaches are restricted to cloud free conditions (Wendleder et al., 2018).

Microwave based remote sensing allows to gather information concerning surface roughness and dielectric properties of a surface also during cloudy conditions (Tsai et al., 2019). Shallow and dry snowpacks are transparent at microwave frequencies, for the wavelength is far larger than the size of snow crystals and hence the attenuation length of snowpacks is long (Marin et al., 2020; Rees, 2006). The presence of liquid water within the snowpack, however, changes the dielectric property of the snowpack so that the microwave signal is primarily attenuated (Largeron et al., 2020).

Such SAR based wet snow detection is performed by calculating a ratio between the corresponding backscatter image and a reference image (Tsai et al., 2019; Piesbergen et al., 1995; Rott et al., 1995; Fortin et al., 1995; Bernier et al., 1992). This reference image features only dry or no snow coverage. Using a simple thresholding approach on the difference image, wet snow can be detected.

Recent studies introduced either a synergy between SAR and passive microwave images (e.g. Zhou et al. (2017)) or a combination of SAR and optical images (e.g. Nagler et al. (2018) and Wendleder et al. (2018)) to map wet snow cover.

Optical data sets are used both for the extraction and creation of auxiliary data sets to minimize SAR backscatter misclassifications (e.g. land cover maps; Wendleder et al. (2018)) as well as to create a reference image for the validation of SAR wet snow products (Jäger, 2016).

Hitherto, no standard approach for a reference image creation has been established. As applied in earlier studies, the reference images used e.g. in Wendleder et al. (2018) or Nagler et al. (2018) feature the study site in snow-free or dry snow cover conditions. The radar reference image is often either a single acquisition image or an average of multiple images acquired during favourable conditions. These studies are prone to stochastic corruption within the validation process due to change in-between acquisition times. An approach to minimize such corruption is essential to enable a comparison of the performance of various extraction methods.

Diverse studies strove to retrieve snow depth using SAR based techniques with moderately successful results (Shi et al., 2000; Rutter et al., 2019; Guneriussen, 1997). Also, approaches based on interferometry were attempted (Varade et al., 2020; H. Li et al., 2017). Using a synergy between cross-polarization Sentinel-1A and -1B backscatter products, as well as optical snow cover extent information, Lievens et al. (2019) published estimates of dry snow depth variability. Their change detection approach was based on an increase of the probability of depolarization on snow crystals compared to ground backscatter. This approach was further developed in Lievens et al. (2021). However, this paper is at present online open for reviewing but was disclosed at a too short notice to allow implementation of changes in the applied algorithms in this project or to follow the suggestions of parameter improvements.

SAR images over a single region are often acquired in multiple geometries. Data acquired from different orbits/flight-tracks will be referred to as multi-track. Small (2011) introduced a robust process of Radiometric Terrain Correction (RTC). The resulting image is based on "terrain-flattened" gamma-nought (γ°_{T}) backscatter and corrected for geometry as well as for radiometry using a Digital Elevation Model (DEM). This use of a DEM stands in contrast to conventional ellipsoid correction. Multi-track composites that include the usage of ascending and descending tracks even over mountainous terrain were developed in Small (2012) and optimized in Small et al. (2021). The study of Howell et al. (2019) indicated γ°_{T} backscatter to be the most robust approach for the detection of wet snow and melt onset. Using this multi-track approach, the orbital revisit time enabled the creation of higher temporal resolution data sets than single-track approaches, used in previous SAR wet snow detection, were able to generate (e.g. used in Nagler et al. (2018)). It has already been successfully used in studies featuring spatial resolution of 400 m and 90 m, respectively (Small et al., 2021; Vögtli et al., 2018).

1.3 Study aim

In this study we work towards improving the identification of wet snow areas and the retrieval of snow depth using multi-track composites featuring temporal resolution down to a 36 h revisit time. This was made possible with standard Sentinel-1A and -1B Radiometrically Terrain Corrected (RTC) backscatter products (Small, 2012). Using a combination of high resolution optical and radar data sets, we test approaches for the generation of an optimal dry winter radar reference image used in SAR wet snow detection. We examine the performance of the current LRW algorithm in relation to land cover classes and elevation by analyzing slope dependent time series. We conduct state-of-the-art wet snow detection on diverse spatial resolutions and polarization states and assess statistical performance. We examine the applicability of the method by Lievens et al. (2019) to a regional scale test site (Bernese Alps). Thereby, we assess its feasibility for an accurate snow depth classifications using correlation and causation validation approaches. Also, we conduct snow depth extraction not only on up to 100 m GSD, as in the currently reviewed Lievens et al. (2021), but up to 30 m.

1.4 Research questions and hypotheses

Within this study, we focus on the following research questions and corresponding hypotheses:

Research Question 1:
What opportunities offer multi-track backscatter composites for wet snow mapping in alpine areas?

Hypotheses:

1.1 LRW composites are homogeneous: Variance over time of the S1 LRW image between East and West facing slopes are minimal and found variances can be attributed to acquisition timing.

1.2 VV-polarized backscatter information achieves a more similar trend across slope directions and offers more homogeneous composites than VH-polarized data.

1.3 Elevation and land coverage (especially vegetation) influence the resulting time series and the reliability of this slope dependency approach for LRW homogeneity testing.

Research Question 2:
Which approach for the generation of a dry winter reference image achieves highest accuracies in wet snow detection when compared to model based LWC maps?

Hypothesis:

2. Creating a median composite image over the winter months relevantly improves wet snow mapping compared to a single composite or a median of three based approach, when compared to liquid water content maps.

Research Question 3:
Are multi-track backscatter composites sensitive to snow depth when applying the method of Lievens et al. (2019)?

Hypotheses:

3.1 By applying the method of Lievens et al. (2019) a correlation between snow depth and the VH/VV-backscatter difference is achieved.

3.2 By applying the Granger test a forecasting chain between IMIS snow depth measurements, snow depth retrieved from S1 and snow depth approximated from a snow water equivalent model is found.

1.5 Outline

In the next chapter, the study site is presented and available data sets are described. Chapter 3 then explains the applied methodologies, before the results are presented in chapter 4. Results are discussed in chapter 5 and possible improvements are propounded. After an outlook into the future of remote sensing of the cryosphere, the conclusions are drawn in chapter 6.

2 Data

This chapter outlines the data sets used throughout the thesis. Therefore, an introduction to the test site is provided. First, the origin of the used SAR images is described and the process of LRW generation explained. Then, optical imagery is delineated, followed by an outline of the validation data sets provided by SLF and MeteoSwiss. A description of additional used information such as land cover data, digital elevation model and temperature, is provided.

2.1 Study area

2.1.1 Bernese Alps

The study area of this thesis is located in the Bernese Alps in Switzerland (see Fig. 2.1). The area covers 3'042 km^2 and extends from 5'102'000 to 5'180'000 m North and from 361'000 to 420'000 m East in UTM zone 32 coordinates. *Thun* is the largest city within the region. The area's terrain is dominated by mountains. The elevation ranges between 465 and 4509 m.a.s.l. with mount *Weisshorn* being the highest mountain present.

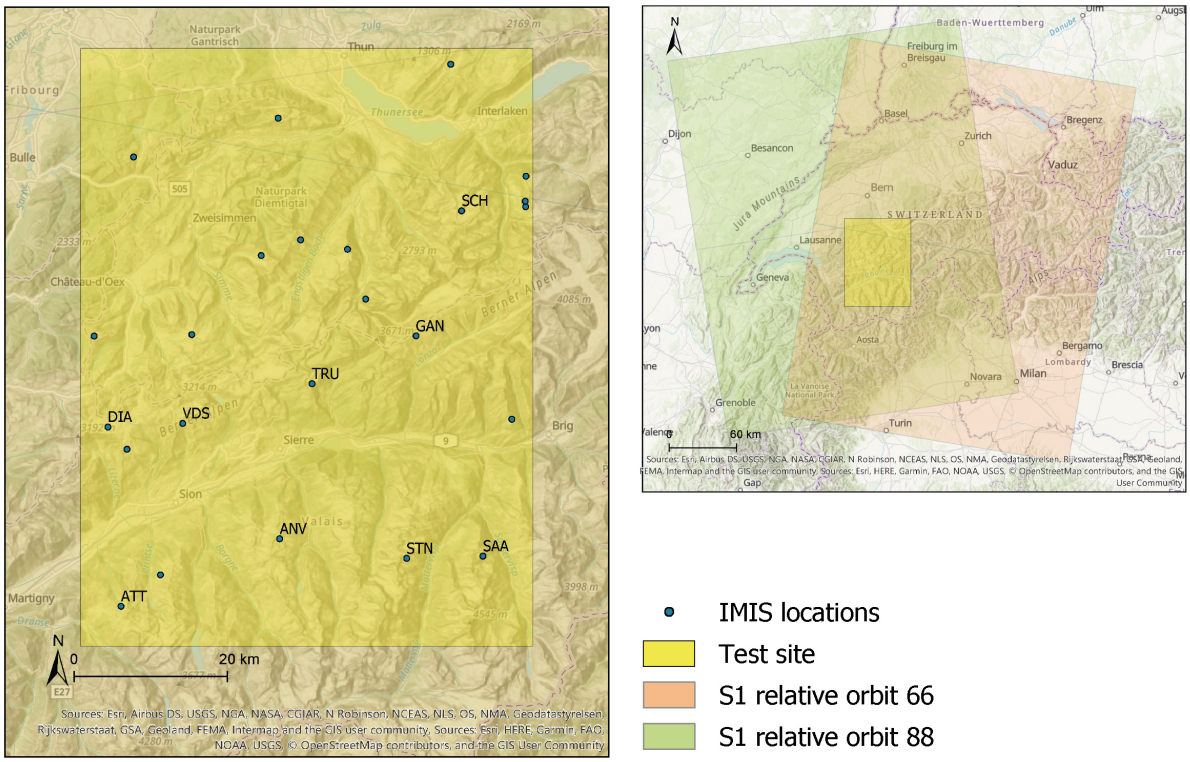

FIGURE 2.1: Map and inset map featuring the main study (yellow) area in the Bernese Alps and Sentinel-1 relative orbits 66 (orange) and 88 (green). Dots represent locations of IMIS stations. The nine labelled IMIS locations are used for snow depth validation. A detailed view of the location of these nine stations is provided in Fig. 5.1.

The test site includes Lake *Thun* and the western part of Lake *Brienz*. Higher elevated areas are dominated by bare rock and around 4 % of the entire test site is covered by glaciers (calculated using GLAMOS). Below the tree line, however, CORINE data (European Environment Agency, 2018a) suggests coniferous forest to be the most common land cover class. Pastures dominate in the valleys, with the exception of settlements near the two lakes.

Typical mean values of the daily maximum temperature in the "Bernese Alps" (location: 46.42 °N 7.75 °E, 2447 m.a.s.l.) vary between -4 and +13 °C, while mean daily temperature minima vary between -11 and +5 °C over the course of the seasons (see Fig. 2.2; MeteoBlue, 2021). The amount of precipitation is typical for a central European climate and varies between 60 to 140 mm per month, with higher precipitation during the summer (see Fig. 2.2).

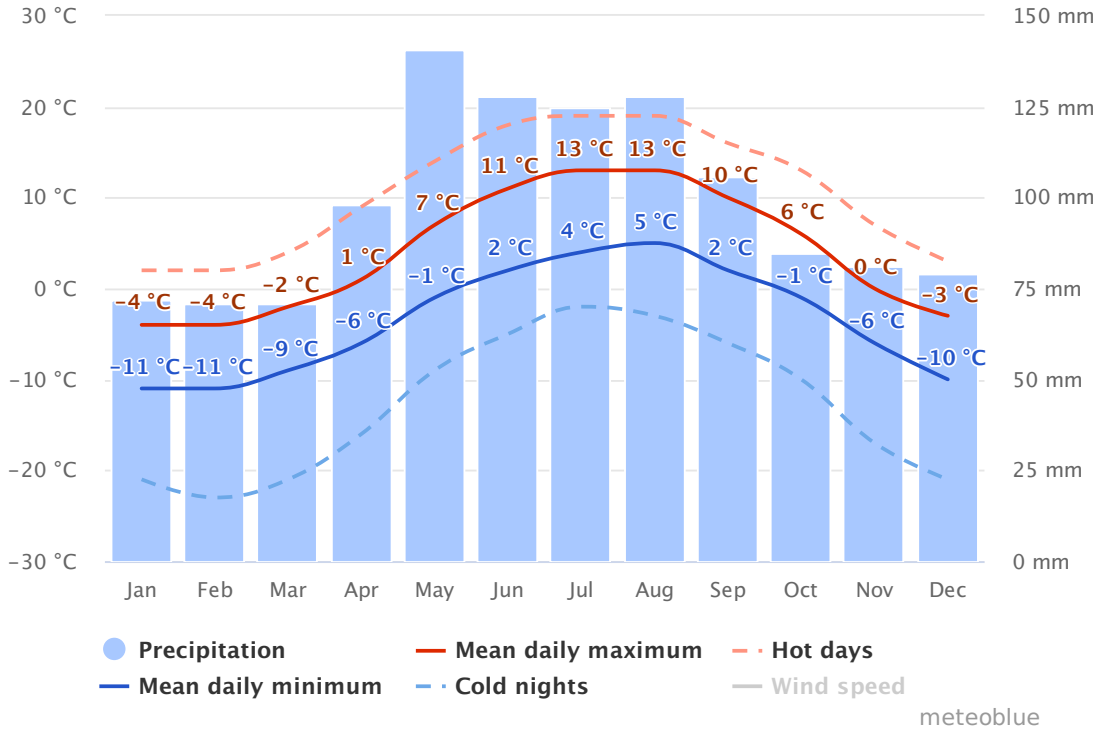

FIGURE 2.2: Modelled mean temperature, precipitation and wind speed for the "Bernese Alps" over the last 30 years from MeteoBlue (2021): Measuring station 46.42 °N 7.75 °E, 2447 m.a.s.l..

2.1.2 Suitability of the study site

The Alps offer a highly dynamic environment including steep slopes. The valley of *Lauterbrunnen*, which lies South of *Interlaken*, is one of the steepest in Europe. As a result, this area represents an optimal study area to test LRW composites from Sentinel-1 imagery. The footprint of Sentinel-1's ascending and descending tracks overlap in central Switzerland (see Fig. 2.1). By using ascending and descending tracks, the composite represents the scene's state within a time span of 36 hours (Small, 2012). The concentration on this rather small region therefore enables the construction of a homogeneous time series with relatively high temporal consistency.

2.2 SAR imagery

2.2.1 Sensor characteristics

In this study, Synthetic Aperture Radar (SAR) composites were used based on Sentinel-1A and -1B backscatter data (see Table 2.1). The European Space Agency (ESA)'s Sentinel-1 (S1) satellites were launched in April 2014 and 2016, respectively (ESA, 2021). Together, they offer an orbit repeat interval of six days (see Table 2.1). Both satellites carry a C-band SAR, operating at central frequency of 5.405 GHz. Each is able to capture and provide data in four operating modes. S1 satellites are capable of interferometric wide (IW) swath mode, extra wide swath mode, stripmap mode and wave mode. Depending on the chosen operating mode, the spatial resolution can vary between 5 to 80 m and is characterized by the number of looks (single look or a variable number of multiple-looks). S1-B, however, has a slightly higher sensitivity than its sister satellite S1 (Schmidt et al., 2020). This bias especially effects the cross-polarized information VH. Schmidt et al. (2020) detected an offset of between 0.03 and 0.61 dB over so-called lower backscatter regions such as Greenland ice.

2.2.2 Radiometric calibration

Following the definition of Small (2011), radar backscatter (β) describes "a ratio between the scattered power (P_s) and incident power (P_i) at ground level":

$$\beta^\circ = \frac{P_s}{P_i} \tag{2.1}$$

Fig. 2.3 displays three conventional reference areas. While reference area A_β is defined on the slant range plane, the corresponding radar brightness is referred to as beta nought β°.

A_σ on the other hand is defined on the displayed ground area. Instead of this widely applied sigma nought σ° (Nagler et al., 2016) backscatter can be projected onto a plane, which is perpendicular to the sensor's line of sight and reach, so called γ°_E. This is the projection, which is closest to real live view of the sensor and as such preferable (Small et al., 2021; Rohner, 2014; Small, 2011). The normalization area $A_{\gamma(r,a)}$ (see Fig. 2.3) is calculated individually for each range (r) and azimuth (a) coordinate to achieve terrain-flattened γ°_T (Small et al., 2021):

$$\gamma^\circ_T = \beta^\circ * \frac{A_\beta}{A_\gamma(r,a)} \tag{2.2}$$

Radar backscatter images of steep terrain are typically afflicted by geometry-induced effects. Steep terrain can result in shadow, foreshortening or even layover of the received signal (Small, 2011). These effects can be modelled and masked during orthorectification of the data onto a DEM. However, radiometric effects of the terrain remain in simple Geocoded Terrain Corrected (GTC) image products. Only by applying radiometric terrain correction (Small, 2011) the backscatter does become relatively "flat" in relation to the terrain: terrain-induced radiometric distortions (Jäger, 2016) are then mitigated. These corrections become extremely important in regions with steep terrain. However, even Radiometrically Terrain Corrected (RTC) products retain the variations in local resolution that are inherent to GTC products.

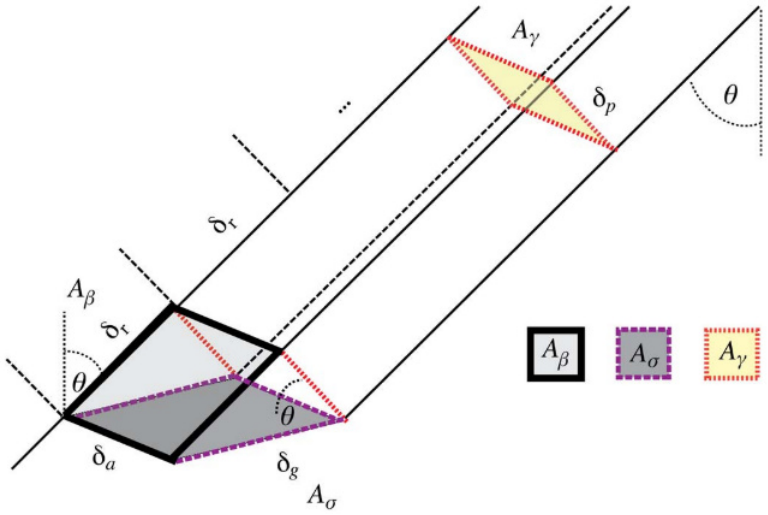

FIGURE 2.3: Illustration featuring reference areas by Small (2011).

2.2.3 Local resolution weighting (LRW) composites

Most SAR sensors, including the ones used in the S1 mission, are right-looking. In the Northern hemisphere, this results in the acquired image of a descending flight track illuminating towards the South-Eastern side of mountains, whereas ascending images illuminate towards the South-Western side of mountainous regions. In an ideal case, by combining two such images one can form a normalized view of the complete terrain. The spatial resolution can be improved by making use of multiple contributing images, also enabling multi-temporal noise reduction in the composite image.

Radiometrically terrain-corrected (RTC) images using the γ°_T convention can be combined, especially ascending and descending orbits, to produce composite backscatter products. In Small (2012) and Small et al. (2021) it was shown how shadowing effects can be mitigated by producing composites from such RTC images, which are weighted based on the local resolution. The Sentinel-1 satellites acquire all data in a right-looking configuration; by using both ascending and descending orbits, mountainous terrain is viewed from substantially different directions: a weighted combination of the acquired data according to its local resolution takes advantage of the high local resolution on backslopes, and allows compensation for missing data (shadow) in an individual orbit (Small, 2011).

The local area (A_i) observed by RADAR systems is inversely proportional to the local image resolution (Small, 2012). Small et al. (2021) exploit this relation and calculate weights Wi based on the sum of resolutions for each image i of the present non-shadowed RTC image input samples $\gamma_{i,\ldots,M}$.

$$W_i = \frac{1}{A_i} * \sum_{j=1}^{M} \frac{1}{A_j} \tag{2.3}$$

These weights are then applied to the corresponding geometry sample location of backscatter γ°_T to create the estimated backscatter composite γ°_c, so-called Local Resolution Weighting (LRW) composites (Small et al., 2021; Small, 2012). As described by the equation (see Equ. 2.4), these do not include information from shadowed pixels but a combination of images from different flight tracks (Small et al., 2021).

$$\gamma^\circ_c = \sum_{i=1}^{M} W_i * \gamma^\circ_i \tag{2.4}$$

TABLE 2.1: Overview of relevant satellite missions for this thesis. "Orb.rep.int." stands for orbit repeat interval, "Nom. resol." for nominal resolution and f^{-1}, λ for frequency and wavelength, respectively. Sources: (ESA, 2021; NASA, 2021a; NASA, 2021b; NASA, 2021c)

Mission	Orb.rep.int.	Sensor	f^{-1}, λ	Channels/Bands	Nom. resol.[m]
Sentinel-1A Sentinel-1B	6 days	C-band SAR	5.405 [GHz]	dualpol (VV,VH)	IW: 20
Sentinel-2A Sentinel-2B	5 days	MSI	442-2202 [nm]	13 spectral bands	10/20/60
Landsat 7 Landsat 8	16 days	ETM+ OLI/TIRS	450-2350 [nm] 430-2290 [nm]	8 spectral bands 10 spectral bands	15/30/60 15/30/100
MODIS Terra MODIS Aqua	16 days	MODIS	620-14685 [nm]	36 spectral bands	250/500/ 1000

Throughout this thesis we work on such γ_c° products. The data used, was recorded in IW swath mode and was acquired between January 2018 and September 2020. It features dual-polarized channel information (VV, VH) and was arranged as a ground range detected high-resolution (GRDH) product time series. The product's original sample interval (in both ground range and azimuth) was 10 m, corresponding to a nominal resolution of 20 m. These LRW composites are presented in Swiss coordinates: CH1903+/LV95 (EPSG: 21781).

Each LRW image is a composite of an ascending and a descending image, acquired on S1 relative orbits 66 and 88 at 05:34 and 17:20 UTC respectively, or (dependent on the seasonal activation of daylight savings time) 06:34 and 18:20 or 07:34 and 19:20 local time (see Fig. 2.1). By combining input data, where ascending and descending passes are 36 hours apart, a relatively tight time-tagging was achieved over the test site.

Over the complete time frame of two and a half years (see Fig. 2.4), S1 time series were gap free, although six images were ignored due to missing data (e.g. one of the ascending or descending geometries was not acquired due to a short-term failure or planned unavailability of one of the satellites, Hajduch et al., 2019; Meadows et al., 2020). The affected composites date to June, 9-10 and November, 25-26 of 2018, February, 28-29 and September, 14-15 of 2019, as well as June, 10-11 and 22-23 of 2020 (see Fig. 2.4).

2.3 Optical imagery

2.3.1 Sensor characteristics

2.3.1.1 Sentinel-2

ESA's Copernicus programme includes a two satellite constellation mission called Sentinel-2 (see Tab. 2.1). Sentinel-2A and -2B were launched in June 2015 and March 2017, respectively (ESA, 2021). Together, the satellites offer a five-day orbit repeat interval at the equator. Each features a swath width of 290 km. Both carry a MultiSpectral Instrument (MSI). These MSIs are capable of measuring data in 13 spectral bands between 442.3 to 2202.4 nm, with spatial resolution varying between 10 and 60 m. Over Switzerland, Sentinel-2 images are acquired around 10:30 local time.

2.3.1.2 Landsat 7 & 8

The US-American National Aeronautics and Space Administration (NASA)'s first Landsat satellite was launched in 1972. Since then, multiple satellites within the continuing mission to observe Earth from Space were developed and sent into orbit. Currently operating are Landsat 7 and 8, which were launched in 1999 and 2013, respectively (NASA, 2021c). Landsat 7 and 8 each offer an orbit repeat interval of 16 days at an altitude of 705 km. Acquisition of Landsat 7 and 8 data takes place at 10:30 over Switzerland local time.

Mounted on Landsat 7 is the Enhanced Thematic Mapper (ETM+) sensor (Ihlen et al., 2019a). It detects light in 8 different bands. Bands 1-5 and 7 are light from the visible to short wave infrared part of the EM spectrum (450 to 2350 nm). The sensor offers spatial resolutions between 15 and 30 m. Band 6 acquires thermal data in 60 m spatial resolution, whereas band 8 gathers panchromatic information with a spatial resolution of 15 m.

Landsat 8 carries an Operational Land Imager (OLI) sensor and a Thermal Infrared Sensor (TIRS) (Ihlen et al., 2019b). The first includes 9 bands, of which bands 1-7 are at wavelengths from 430 to 2290 nm, featuring a spatial resolution of 30 m. Band 8 is panchromatic from 500 to 680 nm, featuring a 15 m resolution, whereas band 9 measures cirrus information (1360 - 1380 nm) at 30 m spatial resolution. TIRS, on the other hand, focuses on thermal infrared and includes only two bands, both providing 100 m spatial resolution at 10'600 to 11'190 nm and 11'500 to 12'510 nm, respectively.

2.3.1.3 MODIS Aqua & Terra

NASA's sister satellites Terra and Aqua carry a Moderate Resolution Imaging Spectroradiometer (MODIS; NASA, 2021a; NASA, 2021b). Terra was launched in 1999 and follows a descending node. Aqua, on the other hand, was released in 2002 and follows the corresponding ascending node. They orbit around the earth at a height of 705 km. Acquisition of images over the test site take place at 10:30 for Terra and 13:30 for Aqua (in local time).

MODIS acquires data in 36 different bands (NASA, 2021d) between 620 and 14385 nm. Band dependent MODIS' spatial resolution varies between 250 and 1000 m. The cross-track swath dimension of MODIS is 2330 km.

2.3.2 ExoLabs snow cover product

The Swiss company ExoLabs Earth Observation Solutions is a spin off from the University of Zurich and was founded in 2017 (ExoLabs, 2021). The company's goal is to provide individually customized software solutions, data products and scientific knowledge in the working area of remote sensing. ExoLabs developed a 'Continuous Snow Monitoring System for Snow Cover, Snow Depth and Snow-Water-Equivalent', called COSMOS (ExoLabs, 2021).

Using sensor fusion of Sentinel-2A/-2B, Landsat 7/8 and MODIS Aqua/Terra data, a daily snow occurrence likelihood product is generated (Wulf et al., 2020). Key characteristic is its 20 m spatial resolution (see Tab. 2.1) and gap-free coverage of Switzerland and the European Alps. This resolution is gained by applying machine learning techniques to model snow probability beneath local cloud cover (hence, the products name 'proba[bility] extrapolated'). Additional data sets like elevation, land cover and solar radiation are used in this analysis (Wulf et al., 2020).

The comprehensive data set provided by Exolabs investigated within this thesis includes data from between June 2018 and August 2020 (see Fig. 2.4). The images feature 20 m spatial resolution and near-daily coverage. For 10 out of 262 analyzed days, no snow cover product was available, due to data unavailability and processing issues.

Table 2.2: Overview of replaced optical composites [YYYY.MM.DD]. No replacement required in 2020.

missing date	substitution date	missing date	substitution date
2018.12.19	2018.12.18	2019.05.12	2019.05.11
2018.12.23	2018.12.24	2019.06.12	2019.06.11
2018.12.27	2018.12.28	2019.07.11	2019.07.12
2019.01.13	2019.01.12	2019.11.07	2019.11.08
2019.04.12	2019.04.11	2019.11.26	2019.11.27

In these cases, the next available image was used instead (see Table 2.2). To account for the acquisition of all composite parts of the S1 images, snow occurrence was checked on both acquisition days (within the 36 hour period of the S1 acquisitions). This information concerning snow occurrence likelihood is provided in UTM32T (EPSG: 32632) and contained digital numbers between 1 and 255. The data is available in a nation wide coverage.

2.4 Liquid water content (LWC) and snow water equivalent (SWE) maps

The Institute for Snow and Avalanche Research (SLF) is a subsidiary of the Swiss Federal Institute for Forest, Snow and Landscape Research (WSL) with its research focus on mountainous ecosystems (SLF, 2021b). Core objectives of the research facility are the monitoring, forecasting and prevention of natural hazards in such regions.

SNOWPACK was developed by SLF to enhance the nationwide avalanche prediction (Lehning et al., 1999). With it, three-phased snowpacks can be modelled continuously over space on the main basis of IMIS point measurements (see section IMIS data). The collected data contains snow depth measurements as well as local weather information (Lehning et al., 2002). An error catching system prevents implausible point data by comparing the measured snow depths with neighbouring stations. SNOWPACK was found to be one of the most sophisticated models for representing snow structure, whereas it offers higher vulnerability towards misrepresentation of turbulent fluxes (Essery et al., 2013). The present snow model incorporates the multi-layer JULES Investigation Model (JIM) (Winstral et al., 2019). Originally, JIM was designed to examine the sensitivity to parameterization of processes in snowpacks (Essery et al., 2013). JIM was initially developed for the sensitivity assessment of three-layered snowpacks towards various parameters and variables (Moeser et al., 2016). Full information concerning configurations used during modelling within the multi-model framework of JIM can be found in Winstral et al. (2019). SNOWPACK also accounts for water percolation effects. This leads to an offset between initial snow melt within the top snow layer and run off information.

The usage of SNOWPACK data allowed the availability of snow water equivalent (SWE) and liquid water content (LWC) information at a daily interval between January 2018 to August 2020 (see Fig. 2.4). The maps provide a spatial resolution of 1000 m and are projected in CH1903+ LV95 (EPSG: 21781). While LWC is provided as a volume-percentage, SWE is described with units of millimeter.

Table 2.3: Aggregation of CORINE land cover classes.

Class group	CORINE classes
Urban area	$CLC <= 11$
Agriculture	$11 < CLC <= 22$
Forest	$22 < CLC <= 25$
Scrubland	$25 < CLC <= 29$
Bare soil	$29 < CLC <= 33$
Glaciers/perpetual snow	$CLC = 34$
Water bodies	$40 <= CLC$

2.5 Snow depth point measurements from IMIS

The Intercantonal Measurement and Information System (IMIS) provides snow depth measurements. The stations are operated by either SLF or MeteoSwiss, the Federal office for meteorology and climatology, (Winstral et al., 2019). The relevant spatio-temporal subset was used in this thesis. These measurement sites are illustrated in Fig. 2.1. The measurement stations are generally located in a "windless" position (Lehning et al., 1999), and measured manually once per day between 7 and 7:30 am. Every half hour, the automatic measuring system delivers snow depth information (Würzer et al., 2018). Gap free information between January 2018 and August 2019 is available (see Fig. 2.4).

2.6 Land cover: Copernicus and GLAMOS

Coordination of Information on the Environment (CORINE) land cover (CLC) was a project initiated by EU commission to standardize data collection of biophysical traits of the Earth's surface across Europe (European Environment Agency, 2018a). CLC is run by Copernicus land cover services (European Environment Agency, 2018a). Its current version from 2018 classifies the Earth's surface into 44 different land cover classes (European Environment Agency, 2018a) using Sentinel-2 and Landsat 8 for gap filling.

CLC was used to create a water body mask as well as a coarsely classified overview image of the area. For the latter, the following classes were computed (see Tab. 2.3). To account for the multiple spatial resolutions required, a median based nearest neighbour re-sampling method was applied to ensure adherence of classes.

High resolution maps featuring tree cover density information (TCD; European Environment Agency, 2017) were utilized. These were made available by Copernicus' land cover monitoring program. Tree cover density describes a pixel's proportional crown coverage. Here, a vertical projection of tree crowns to a horizontal Earths surface is used (European Environment Agency, 2018b). The data ranges between 0 and 100%, whereby values of zero indicate no tree occurrence.

The TCD version used, dated from 2018. The data was provided with a 10 m grid interval. Spatial re-sampling was performed using a median based scanning method during re-projection of ETRS89-extended (EPSG: 3035, for further information see: MapTilerTeam, 2019) to UTM32T.

A glacier mask was prepared based on data from GLAMOS - the Swiss glacier inventory (SGI 2010) (GLAMOS, 2010). This inventory is based on aerial photographs from 2008 to 2011 and includes all Swiss glaciers. The data is opensource and freely available on the GLAMOS homepage as a shapefile (GLAMOS, 2010). GLAMOS was preferred over CORINE data for the generation of a glacier mask as, in the latter, glaciers and perpetual snow build one class and can not be distinguished.

2.7 Digital elevation model

The federal office of topography (swisstopo) provides open elevation data with nationwide coverage. The DEM swissALTI3D was used to describe the test site's vegetation-free surfaces in metres above sea level (Swisstopo, 2018). swissALTI3D is generated every six years, using a combination of stereo air photos and airborne laser scanning (ALS). The latest version was used, which is based on a patchwork of LiDAR overflights between 2012 and 2019. The used version features a spatial resolution of 2 m.

2.8 Temperature

The federal office for meteorology and climatology (MeteoSwiss) provided daily maximum air temperature maps, which were used in this thesis. Present temperature maps were based on in-situ data gained from approximately 90 measuring sites spread across Switzerland (Meteoswiss Climatology, 2017). Temperature values were provided in Degrees Celsius [°C], and signify near-surface air temperature. They were measured with a temporal interval of 10 minutes over the two and a half years (see Fig. 2.4). The data set was provided at 2200 m spatial resolution in the projection format ETRS89-extended (EPSG: 3035). A detailed account of the resampling procedure of the temperature data set is provided in the methods' section.

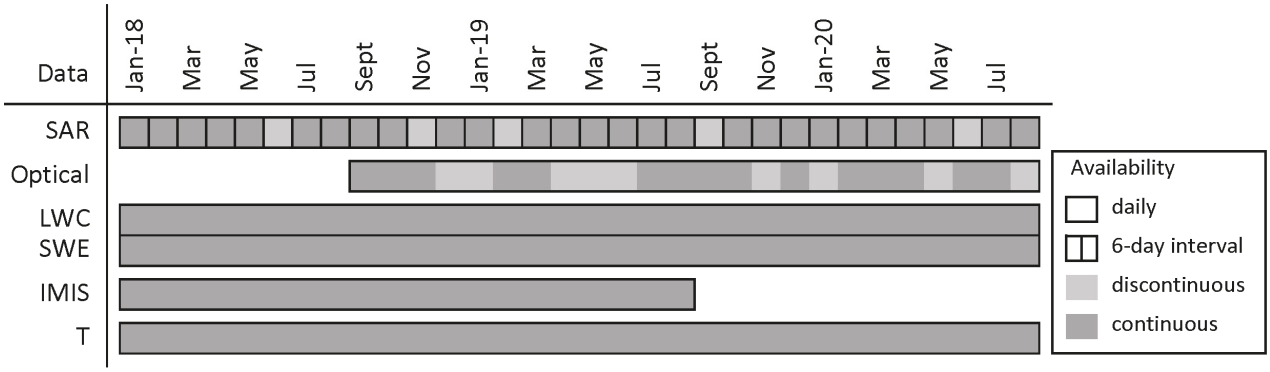

FIGURE 2.4: Degree of data availability over the observed time series. Discontinuous availability indicates months including relevant data unavailability due to weather effects or sensor unavailability. Daily interval was available for all but SAR imagery, which featured a six-day interval. For easier readability shortnames were used for input data: 'SAR' stands for 'LRW composites', 'Optical' for 'snow cover likelihood images', 'LWC' and 'SWE' represent 'liquid water content' and 'snow water equivalent'. 'IMIS' indicate the measurements by IMIS stations and 'T' the temperature measurements.

3 Methods

In a first part, this chapter provides an overview into snowpack characteristics at microwave frequencies (3.1). Based on this theoretical dispute, the processing chains as conducted for the present thesis are described. First, the performed pre-processing steps for all data sets used are delineated (3.2). Then, the procedure of LRW composite testing (3.3) is described before outlining the conducted steps during wet snow mapping and the validation for the examination of the influence of reference image generation (3.4). Finally, the performed snow depth retrieval is summarized and the validation procedure explained (3.5).

3.1 Snowpack characteristics at microwave frequencies

The interactions between microwave radiation and snow are complex (Jäger, 2016) and the topic is still a subject of current scientific research. The radiations' path is typically described using a three layered radiative transfer model (see Fig. 3.1), including the two interfaces air-snow and snow-ground (D. Li et al., 2017). Hence, the signal received at the sensor is first scattered at the air-snow (surface scattering), then at the snow-ground (volume scattering) and finally at the snow-air interface (surface scattering) on its way back to the sensor. The measured signal is mainly a result of the synergy between scattering effects at the interfaces and volume scattering within the snowpack.

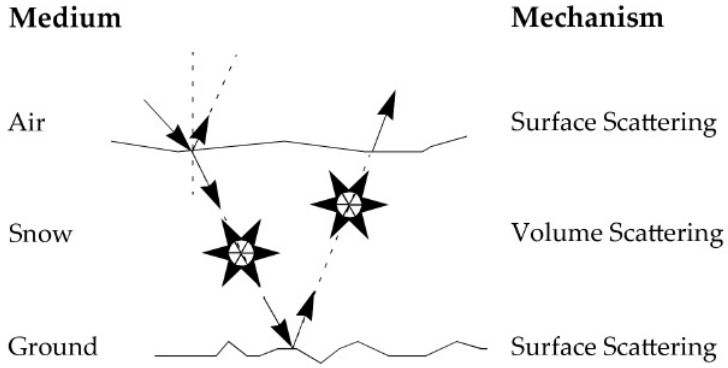

FIGURE 3.1: Radiative transfer model of a microwave signal interacting with a snowpack by Rohner (2014).

The amount of interaction between a radar signal and an object is directly dependent on the object's attenuation length at microwave frequencies. Dry snowpacks are characterized by a large attenuation length at microwave frequencies and are therewith generally invisible to radar signal (Rees, 2006). Deviations occur in cases of usage at higher frequencies than 10 GHz or the presence of very deep snowpacks (in the range of tens of meters; Rees, 2006; H. Li et al., 2017). As a result, it is not possible to differentiate dry snow from no-snow pixels by just analyzing the backscatter signal (Rott et al., 1995). In such cases, main backscattering occurs at the snow-ground interface, whereby snow can be neglected due to its transparency, and the interface becomes an air-ground interface.

Wet snow detection from SAR images is possible due to the strong signal attenuation caused by the high dielectric contrast between frozen and liquid water: a multi-temporal change detection can easily highlight a change in state. The radar backscatter is highly sensitive to liquid water occurrence. As a result, the relatively weak radar backscatter from a melting snowpack is mainly dominated by surface scattering (Rüetschi et al., 2019): a clear diminution of the signal is measurable (Rees, 2006) and a penetration depth is decreased to around 3 cm for C-band SAR (Tsai et al., 2019). Therefore, a reference image during no snow or dry snow circumstance is required for the process of wet snow retrieval. By assessing the amount of the attenuated signal in comparison to a reference image, the localization of wet snow is possible. This is achievable by using a simple thresholding approach (e.g. Nagler et al., 2016).

Key factors influencing the scattering behaviour of a snowpack are the applied radar frequency and the snowpacks' liquid water content (e.g. D. Li et al., 2017; Dietz et al., 2012). Other influencing factors include snow depth (Lievens et al., 2019) and the land cover type (Dietz et al., 2012).

Lievens et al. (2019) were able to correlate in-situ snow depth measurements to S1 backscatter information using an empirical change detection algorithm. Their approach is based on a cross ratio and thereby exploits the effect of the snowpack's volume scattering. This scattering effect leads to a higher likelihood of the backscatter having been re-polarized and consequently more signal is measured in the cross-polarized state. This relation allows a minimization of background noise by enabling a normalization using the magnitude of received co-polarization information.

3.2 Pre-processing

All remote sensing data was provided as Level 3 products, following the definition by NASA (1986). For most data sets, pre-processing was therefore mainly restricted to a re-projection into UTM zone 32T (EPSG: 32632), a resampling to multiple target resolutions, and a cropping to the test site extent. In addition to these steps, erroneous LRW composites due to satellite failures or unavailabilities were identified and replaced.

3.2.1 Main data preparation

The LRW processing at 10 m had originally been generated using the swissALTI3D in Swiss map coordinates. To allow for inter-compatibility with other (optical) data, all SAR data were re-projected into UTM32T and cropped to the target site extent. Spatial target resolutions of 30, 100 and 1000 m were correspondingly generated by down-sampling the data from the initial data set using a median based scan-line algorithm. After caching the so far prepared S1 γ°-composites, a conversion into decibel-space was performed using the following equation, as the available data was provided in linear backscatter units:

$$S1\ backscatter\ [dB] = 10.0\ *\ log10\ (S1\ backscatter\ [-]) \tag{3.1}$$

By analyzing an overall S1 backscatter time series, problematic composites were identified. Six identified composites (see data chapter) were discarded completely and replaced, using a mean image calculated from the LRW composite before and after the missing composite. Such mean images are calculated throughout the thesis on a pixel by pixel basis (with locations r, a) using the following equation:

$$\mu(r,a) = \frac{1}{N}\sum_{i=1}^{N} A_i(r,a) \tag{3.2}$$

N indicates the amount of scalar observations, meaning the amount of images over which the mean is calculated (here: $N = 2$). A_i represents a vector, containing the corresponding values. Voids were ignored during such calculations and replaced by the next available scalar.

Optical snow cover information was down-sampled by using a median based approach (see Equ. 3.3) and up-sampled by using a bi-linear scan algorithm. Both were cropped to the test site extent. The first batch was re-scaled from digital numbers to percentages. The second batch was re-projected to the defined target projection style to assure uniformity.

$$median = \frac{N-1}{2} \tag{3.3}$$

The elevation and land cover data sets were re-projected into the target grid of UTM32T. To account for the multiple (reduced) spatial resolutions needed, the DEM was bi-linearly interpolated, whereas the classified information of the land cover data set and the glacier mask were re-sampled using a nearest neighbour approach.

Temperature data from MeteoSwiss, as described in the previous chapter, was re-projected and cropped to the observed scene. However, its spatial resolution was too coarse to enable adequate usage at 30 m resolved applications. This was especially the case, as the test site is located in mountainous terrain.

3.2.2 Resampling of temperature data

The approach described by Gao et al. (2012) and also in Jäger (2016) enables an improvement of temperature accuracy by resampling from a coarse resolution temperature onto a DEM grid by using a local lapse rate (L). The processing chain is summarized in Fig. 3.2.

The difference in height (Δh) between coarse and high resolution is calculated by subtracting the elevation of the subpixel (h_x) featuring high spatial resolution ($x\ [m] = 10, 30, 100, 1000$) to the elevation of the corresponding pixel of the coarsely resolved input temperature data set (h_{2200}):

$$\Delta h\ [m] = h_{2200}\ [m] - h_x\ [m] \tag{3.4}$$

Diverging from the approach by Gao et al. (2012) and Jäger (2016), we used a static literature value for the local lapse rate (L): the so-called environmental lapse rate of -6.5/1000 $[\frac{^\circ C}{m}]$ (Daly et al., 2009). This enabled us to circumvent the need for ERA5 or ERA-interim input data, which itself offered a maximal spatial resolution of around 13 km^2 (0.125 °C) and was not of relevant accuracy when applied to high resolution images. After testing multiple values for lapse rate approximation, including an elevation based differentiation between dry and wet adiabatic lapse rates, the increase in accuracy within the observed test site was negligible. Therewith, the choice of lapse rate was made in favour of an already well established static value.

Based on this difference in height and the local lapse rate, the change in temperature was approximated. Where T_{ref} stands for the original, input temperature at coarse resolution, and T for the elevation-corrected temperature of the sub-pixel with elevation hx from Equ. 3.4:

$$T\ [^\circ C] = T_{ref}\ [^\circ C] + L[\frac{^\circ C}{1000m}] * \Delta h\ [m] \tag{3.5}$$

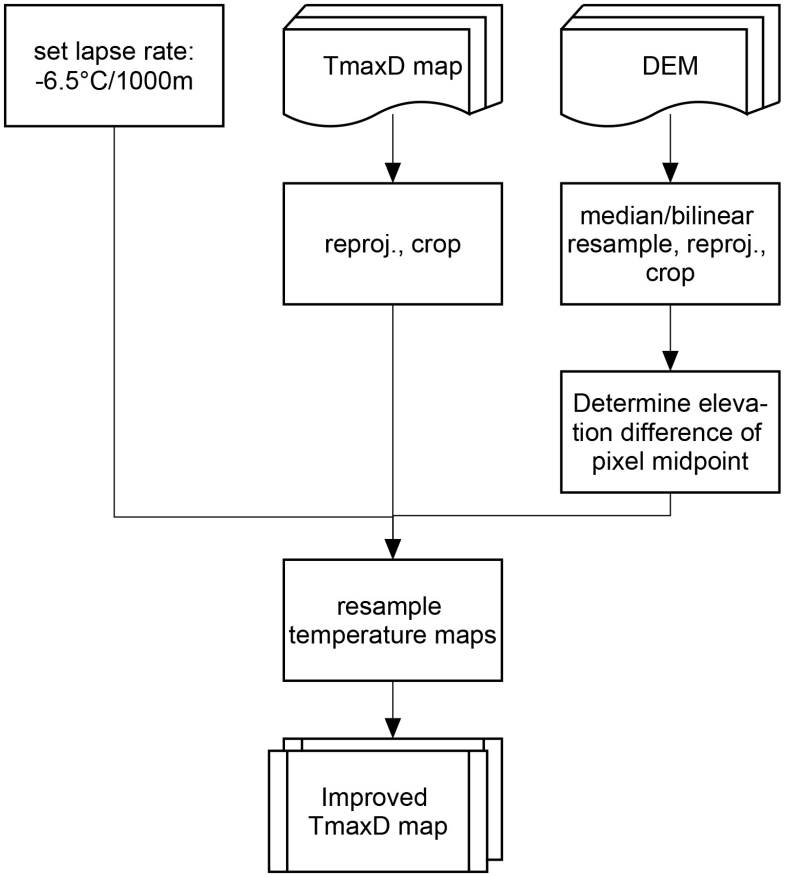

FIGURE 3.2: Flowchart, featuring process chain performed during temperature resampling.

After resampling, a Savitzky-Golay finite impulse response filter (Savitzky et al., 1964) with a polynomial degree (m) of five was initiated, fitting a sliding window over 300 m to smooth out boundaries. It was calculated using Equ. 3.6, where C_i represents convoluting values and N the filter coefficient taken from the Savitzky-Golay table according to the selected m.

$$Y_j = \frac{\sum_{i=-m}^{i=m} C_i \; y_{j+i}}{N} \tag{3.6}$$

3.2.3 Preparation of validation data sets

LWC and SWE data were re-projected and cropped to fit the observed scene. To approximate a validation also at a 100 m scale, the information was bi-linearly interpolated. The locations of IMIS stations were re-projected from Swiss map to UTM coordinates. Out of the 182 stations, 25 were situated inside the observed scene and thus selected for further usage (see Fig. 2.1). Snow depth information was re-scaled from centimeters to the SI unit of meters.

3.3 LRW composite testing using slope oriented S1 time series

By analyzing slope orientation dependent differences within each LRW image, the homogeneity of such LRW composites was examined. Observing this difference in behaviour over time allows to gather a deeper understanding of the relation between slope, orientation, and backscatter characteristics. Similar snow conditions over corresponding terrains were hereby assumed.

The process of generating a slope-dependent time series is illustrated in Fig. 3.3 and was performed for three channels: co-polar (VV), cross-polar (VH) and the cross-polarization ratio (VH/VV). The first two were needed for wet snow detection, whereas the latter has recently been used as the basis for snow depth retrieval from S1 backscatter (Lievens et al., 2019). The calculated ratio (see Equ. 3.1) in linear space is equivalent to the difference in backscatter intensity between the cross- and co-polarized signals in dB space.

$$CR\ [dB] = 10.0\ *\ log10\left(\frac{VH\ backscatter\ [-]}{VV\ backscatter\ [-]}\right) \tag{3.7}$$

The processing chain can be subdivided into four main steps: 1) First, data was pre-processed as previously discussed, then 2) the auxiliary data masks were generated. 3) The class masks were applied and 4) after having utilized post-processing measures, a median time series for each class was plotted.

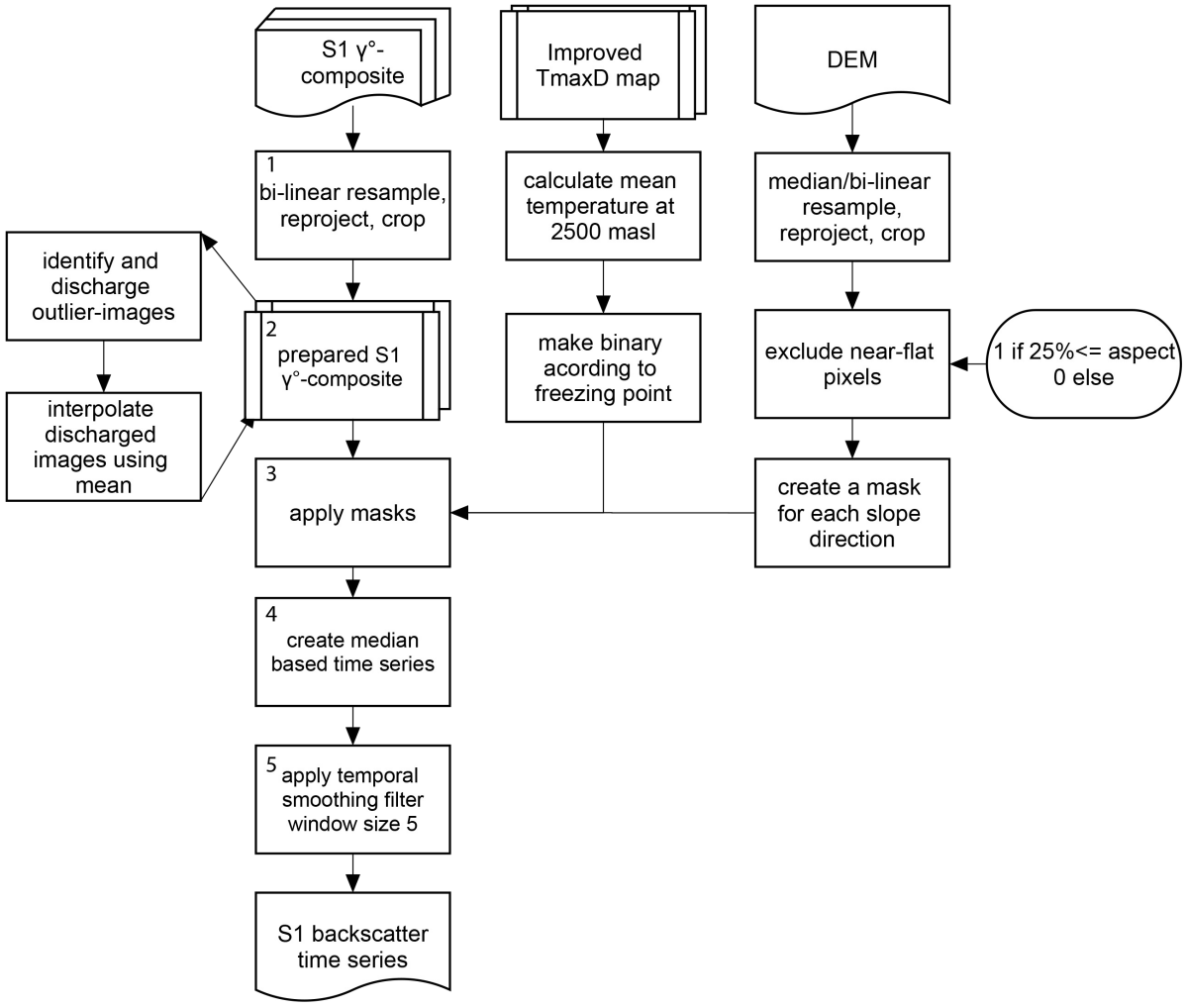

FIGURE 3.3: Flowchart, featuring performed processing chain for the example of aspect dependent time series generation. For further analysis input data also included optical snow cover likelihood maps and CORINE land cover information.

Slope masks were achieved by using the available DEM and extracting the direction in which each pixel decreases most rapidly on a WGS84 projected version of the DEM. Using the thresholds of 45, 135, and 315 degrees, the aspect image (range 0-359, where 0 indicates North) was then masked

into four images, each featuring a cardinal direction. Insufficiently steep terrain was removed from consideration by using an iteratively defined threshold of 15 degrees, ensuring that only slight slopes were not included in the different aspect subsets.

All time series were underlaid by a coloured mask indicating maximum daily temperature in relation to the freezing point at a defined standard elevation level of 2500 m.a.s.l.. To account for the 36 hour range, which each LRW composite encompasses, a mean over the two corresponding days was extracted. An elevation mask was created featuring elevations between 2250 and 2750 m.a.s.l. and corresponding pixels were used to calculate the mean temperature. The mean temperature time series was used to produce a freezing state: temperatures above or below the freezing point were defined following the application of a 3-image kernel temporal filter.

To gain an understanding of the magnitude of multiple factors possibly influencing the created time series, the pixel composition was further examined. A time series was then generated in relation to all prominently represented land cover classes (agriculture, forest, scrubland, non-vegetated, glacier and perpetual snow). To incorporate and quantify the degree of elevation based effects, an elevation-dependent time series was produced. Three thresholds were thereby set at 1000, 2000 and 3000 m.a.s.l. and applied to the digital elevation model.

In all cases, the output time series was prepared by calculating the median backscatter of the corresponding class in each LRW composite. A median based approach was chosen to minimize bias through fluctuate and thermal noise (see Equ. 3.3). The calculation was implemented using a 3x3-pixel kernel. Present values (N [*count*]) were sorted before extracting the median.

3.4 Wet snow mapping

3.4.1 Reference image (RI) generation

Earlier studies have already shown that dry snow LRW composites acquired during the winter surpass summer based composites (Jäger, 2016). This is a likely result of changes caused by a longer temporal offset influencing the calculated difference image. In this thesis, we therefore preferred dry winter over no-snow summer pixels for the creation of a reference image.

Fig. 3.4 displays the performed chain of processes. As input data served the re-sampled temperature data, the prepared LRW composites and optical snow cover maps.

Based on histogram analysis, a threshold is defined which offers a sensible fulcrum between ensuring no wet snow contamination in the considered pixels, while still guaranteeing that enough pixels are available for a relevant calculation. The threshold was set to -2 °C. Dry snow properties are assumed when snow occurs during colder conditions.

To prepare the required masks of snow cover over the 36 h time frame, within which the SAR composites were acquired, the optical images available for both these acquisition dates were analyzed. Each sample's characteristics were thereby examined independently. When the likelihood of a sample in at least one of the two images was above 50%, snow was henceforth assumed to dominate the corresponding S1 pixel's signature.

Three types of reference images (RI) were calculated using the described, re-sampled temperature and optical images that indicated snow coverage:

- Single reference image:
  A single LRW composite was identified that was generated using images acquired during the coldest conditions available under the time series. As the bulk of the test site was under conditions colder than the threshold of -2 °C, there was neither a need to search for colder

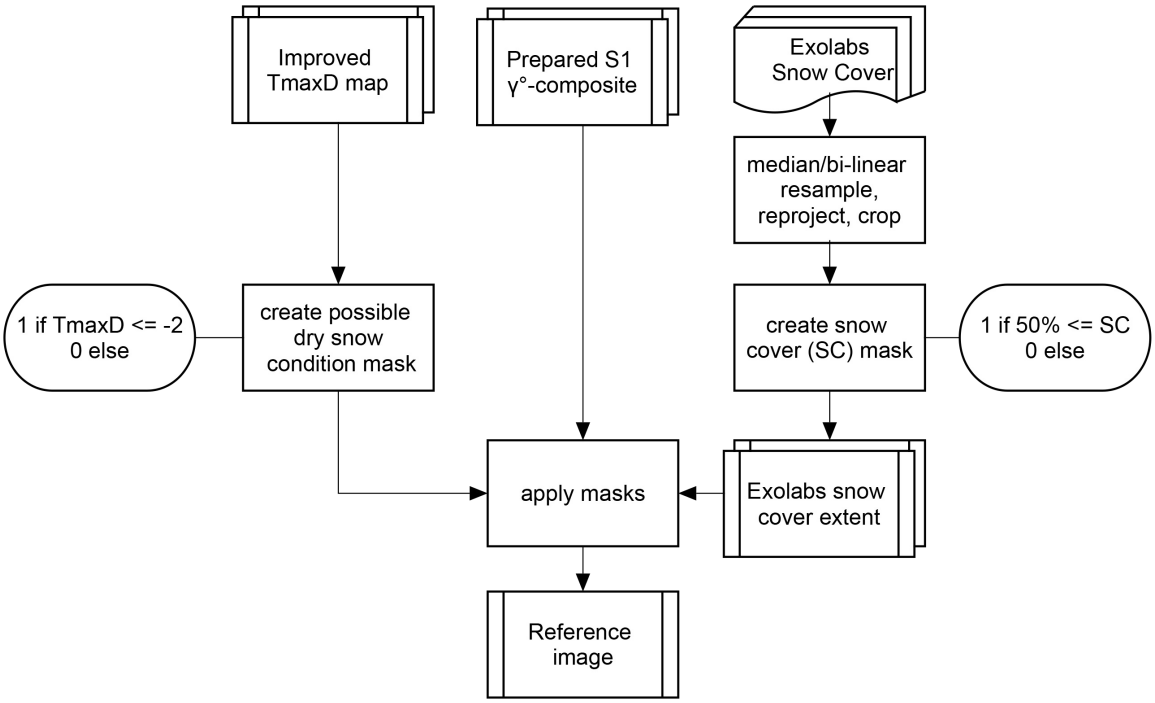

FIGURE 3.4: Flowchart, featuring process chain performed during reference image generation. Intermediate products, generated in an earlier flowchart, are indicated using rectangular features with double bars at the sides.

acquisitions before the available data, nor to supplement the image with no-snow summer pixels. To minimize the effect of possible wet snow contamination, areas featuring insufficient conditions were masked out.

- Median of three reference images:
  A median γ° backscatter image was calculated using the three images acquired during coldest circumstances as the input to account for possible speckle noise occurrences (see Equ. 3.3, $N = 3$). Thereby, only backscatter signal of pixels under dry or no-snow conditions were considered. Areas where none of the acquisitions were under amply favourable conditions, were masked out.

- Winter season reference image:
  A γ° backscatter image was calculated by using a full dry winter season approach. Hereby, a median image of all LRW composites acquired during the three winter months December to February was generated (see Equ. 3.3, $N = 3 * 15$). However, only pixels with either no snow occurrence shown in the optical image or dry snow conditions were considered. The number of contributions from along the temporal axis utilized for the calculation of each corresponding median therefore varied from one spatial sample to another.

3.4.2 Wet snow retrieval

After having pre-processed all data sets and generated a reference image, the performed processing chain can be split into 4 main steps. These are illustrated in the flow chart in figure 3.5. In a first step 1) difference images were produced by the pixel-wise subtraction of the reference image from the corresponding LRW composite. 2) By using a thresholding approach, pixels featuring possible wet snow signals were identified. 3) Land cover masks were applied. 4) Smoothing filters in both temporal and spatial space were applied to minimize the effect of speckle or thermal noise.

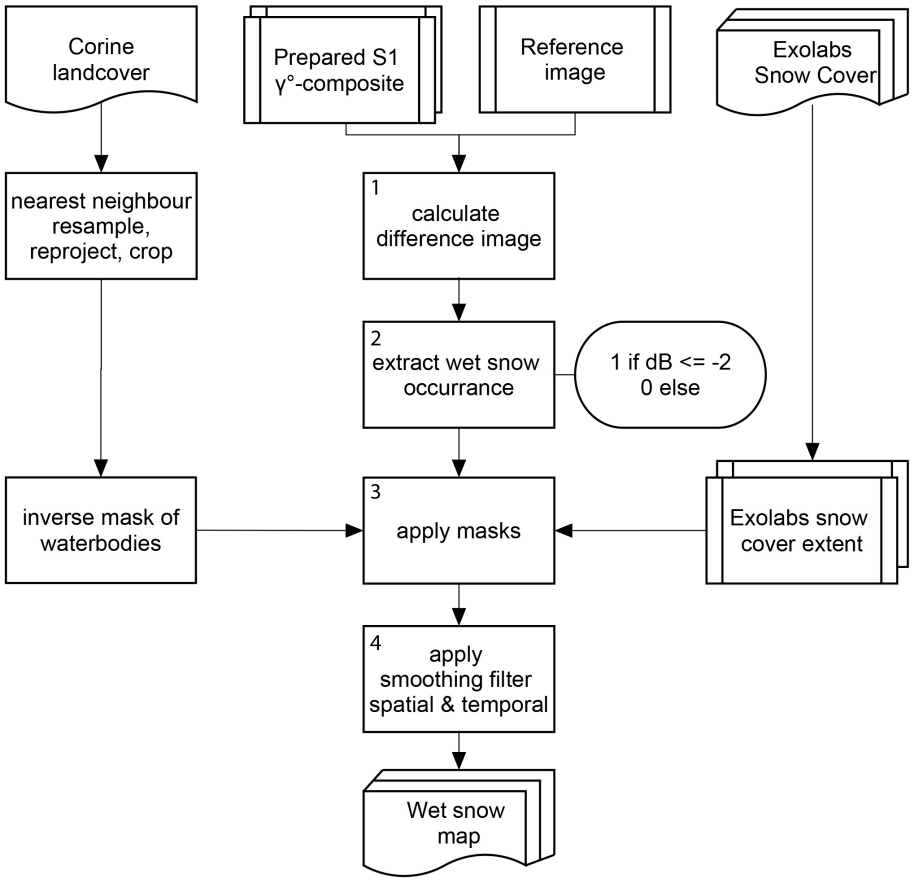

FIGURE 3.5: Flowchart featuring process chain performed during wet snow retrieval. Intermediate products, generated in an earlier flowchart, are indicated using rectangular features with double bars at the side.

Normalized γ° backscatter composites were calculated by subtracting from each LRW composite (dB values) the reference image (see Equ. 3.8). This approach was proposed by Rott et al. (1995) on σ° projected images and has, since their publication, been successfully applied by various researchers in the field of wet snow detection (Baghdadi et al., 1997; Piesbergen et al., 1995). Multiple studies have already shown the applicability of this approach on LRW composites using γ° convention (Small et al. (2021) and Jäger (2016) for Sentinel-1 and Rohner (2014) for ENVISAT ASAR).

$$\gamma^\circ_{diff}[dB] = \gamma^\circ_i[dB] - \gamma^\circ_{ref}[dB] \tag{3.8}$$

This difference image is equal to the ratio on the linear scale and can be classified into binary wet snow occurrence maps using a simple thresholding approach. Dry or no snow are indicated by a backscatter signal *above* the threshold and wet snow occurrence is detected when the signal strength is measured to be *lower* than the threshold. The initial threshold for wet snow detection proposed by Rott et al. (1995) of -3 dB was based on ERS-1 data acquired at a nominal incident angle of 23 degrees, and was revised to -2 dB (Nagler et al., 2016) for Sentinel-1 IW data. For a successful application of this threshold of -2 dB, the γ° difference images were converted into logarithmic dB space, as described in Equ. 3.1, before masking.

Water bodies were masked out using land cover information, and the optical snow cover product served to mask out snow-free areas. This allowed a minimization of false positives. During post-processing of the retrieved wet snow masks, two smoothing filters were applied to correct for speckle and thermal noise over time as well as over space. For each pixel, a temporal smoothing filter with a

window size three was used. Hereby, the pixels were replaced by the mean through three successive images (see Equ. 3.2, $N = 3$). Wet snow was chosen if the median resulted in 0.5 due to the presence of a void (a NaN value). A Gaussian spatial filter with window size 9 (3x3 pixels) was applied to spatially smooth out the image and reduce noise effects. To restore the bi-linearity of wet snow, another threshold was chosen. It was set to 0.7 and was therefore relatively high. This enabled inter-comparison between the resulting data and the comparatively coarsely resolved validation images from SLF. Furthermore, it allowed to eliminate solitary pixels, which were assumed errors.

3.4.3 Validation

The validation of the wet snow mapping algorithm was performed by comparing the results to the LWC data, which were henceforth assumed to be a higher quality independent reference. Following the theory in Rees (2006), a threshold for LWC was determined for a minimal LWC value to pass as wet snow. Based on a comparison of histograms, this threshold was set to 3 Vol-%. Binary images were generated to allow inter-comparisons with binary wet snow maps, whereby a rounded median based on the corresponding dates of S1 acquisitions was calculated.

A calculation of users, producers and the overall accuracy (OA, see Equ.: 3.9) was performed on each image pair using confusion matrices.

$$OA = \frac{Pixels\ correctly\ classified\ [count]}{Total\ amount\ of\ classified\ pixels\ [count]} \tag{3.9}$$

The errors of omission (exclusion, EoO) as well as of commission (inclusion, EoC) in regard to wet snow detection, were calculated as follows:

$$EoO = \frac{Pixels\ falsely\ classified\ as\ dry/no\ snow\ [count]}{Pixels\ featuring\ wet\ snow\ in\ ground\ truth\ [count]} \tag{3.10}$$

$$EoC = \frac{Pixels\ falsely\ classified\ as\ wet\ snow\ [count]}{Pixels\ featuring\ wet\ snow\ in\ classified\ image\ [count]} \tag{3.11}$$

To test the stability of the performed classifications, a Cohen's kappa coefficient (κ) was also generated. This measure of inter-rater reliability allows to compare the performed classification with a random classifier.

$$\kappa = \frac{Overall\ Accuracy\ -\ Producer's\ Accuracy}{1\ -\ Producer's\ Accuracy} \tag{3.12}$$

The overall accuracy, error of commission and of omission each range between 0 and 1. However, a perfect match – and therefore an ideal classification – is achieved, when OA equals 1 and both types of errors are zero. The inter-rater measure, κ, can assume values between -1 to 1. Negative values thereby indicate the classification to have produced a result worse than a performance from a random classifier. A κ of zero suggests the result of a random classifier and indicates chance agreement of the outcome. Values approaching 1 indicate the performed classification to be in perfect agreement with the validation data set, i.e. the ideal circumstance.

3.5 Snow depth retrieval

3.5.1 Retrieval

In this study, we follow an empirical change detection method to extract snow depth from S1 data as introduced by Lievens et al. (2019). However, we chose to use a γ°_{T} backscatter normalization convention (Small et al., 2021) rather than σ°_{T} in the algorithms to allow better "flattening" of terrain-induced radiometric distortions (also suggested by Lievens et al. (2021)).

The processing chain for snow depth retrieval from S1 is outlined as a flowchart in Fig. 3.6. The process is structured into six steps. After 1) calculating a cross ratio, 2) outliers were identified and discharged. The main body is concerned with 3) the computation of the snow index and 4) the snow depth. 5) Land cover classes were excluded by applying corresponding masks before the resulting information was 6) post-processed and the mean time series were created.

To retrieve snow depth from S1, a cross-polarization difference (CR) was calculated in dB as described in Equ. 3.7. Samples whose value was 3 dB above the 90^{th}- or below the 10^{th}-percentile of the time series were masked out. This threshold used by Lievens et al. (2019) was applied and was seen to minimize the effect of speckle and thermal noise.

In the next step, snow cover (SC) at the acquisition times of S1 data was estimated by using the available optical images (as described in the data chapter). Using this snow coverage information, S1 cross-polarized dB-difference pixels featuring no-snow cover were discharged. The remaining S1 information was used to calculate a snow index (SI) as seen in Equ. 3.13, following Lievens et al. (2019). By applying a maximum function (see Equ. 3.13), negative values of snow depth were eliminated by setting them to zero.

$$SI(i,t) = \begin{cases} max(\,0,\,[SI(i,t-1)\;+\;CR(i,t)\;-\;CR(i,t-1)]), & \text{if } SC = 1. \\ 0, & \text{if } SC = 0. \end{cases} \tag{3.13}$$

Here, CR was calculated as described in Equ. 3.7 and indicated the difference between VH- and VV-backscatter amplitude. This stands in contrast to the recently published usage of a weighted cross-ratio using a fitting parameter in Lievens et al. (2021).

This change detection index, SI, was then calculated into snow depth (SD) using Equ. 3.14. For this, two parameters a and b were needed, which were assumed to be constant in space and time.

$$SD_{S1}(i,t)\;[m] = \left(\frac{a}{1 - b * TCD(i)}\right) * SI(i,t) \tag{3.14}$$

Parameter a was empirically defined and calibrated by Lievens et al. (2019) to be $a = 1.1\;[\frac{m}{dB}]$. It adjusts the magnitude of S1 snow depth retrieval to minimize the mean-absolute-error between global averaged in-situ snow depth measurements and a corresponding retrieval from S1. Parameter b is used in combination with tree cover density (TCD) information (Lievens et al. (2019) used fractional tree coverage (FC), a similar MODIS based product) to account for the typical attenuation of radar signals in forested areas (Macelloni et al., 2012; Burgin et al., 2012). As a result, snow depth retrieval over forested areas is corrected using parameter $b = 0.6\;[-]$.

In Lievens et al. (2021) this approach was further developed by creating not only one, but two assisting snow indices. While the first remained equal to what we showed in Equ. 3.13, the second index was created by using the same change detection but solely on VV-polarization. The two indexes were then synthesized into one snow index based on the forest cover fraction of the

corresponding sample. Snow depth over more densely forested areas was extracted using the VV-polarized data, as co-polarized information proved more stable over vegetated zones than cross-polar information (Vreugdenhil et al., 2020). As a consequence of this, Lievens et al. (2021) also optimized parameter b to 0.7 instead 0.6. However, these changes could not be implemented in this thesis due to timing issues and so offer possible improvements for further analyses.

A water mask was created and used to exclude water bodies from snow depth retrievals. Following the approach applied in Lievens et al. (2019), also wet snow pixels were excluded at first. However, this resulted in a very small number of remaining pixels for snow depth retrieval and therefore applying this step was not satisfactory: it was removed from the provisional processing chain.

To minimize the effect of signal noise on the result, the calculated snow depth was smoothed in both temporal and spatial dimensions. A median filter with a kernel of 3x3 was applied for spatial smoothing - this allowed an adaptive smoothing according to the multiple spatial resolutions used (see Equ. 3.3, $N = 9$). Temporal convolution was performed using a median filter of three (see Equ. 3.3, $N = 3$)

3.5.2 Validation

Validation of the performed snow depth retrieval from S1 was approached from two different perspectives to account for the multiple spatial resolutions. Our validation was, in both cases, based on a time series comparison approach. At lower resolutions (1000 and 100 m), the validation was focused on a comparison with a snow depth, which was approximated based on the spatially consistent independent reference data of the snow water equivalent (SWE). The algorithm was validated at higher resolutions (10 , 30 m) by statistically comparing the resulting snowpack progression against the in-situ snow depth time series as measured at automated IMIS snow stations (SLF, 2021a).

For validation purposes, snow depth (SD_{SWE}) was processed from the external snow water equivalent (SWE) data set. To account for the composite's 36 hour inherent time-span, a mean over the corresponding two days of SWE data was calculated. The snow depth was calculated by dividing SWE through the snowpack's density:

$$SD_{SWE}(i,t)\,[m] = \frac{SWE(i,t)\,[mm]}{\rho_{dry\_snow}} \tag{3.15}$$

The dry snow density ρ_{dry_snow} was set to $357\frac{kg}{m^3}$. This value was reported by (Koch et al., 2019) at the location of *Weissfluhjoch*, in the Swiss Alps. The environmental circumstances between the measurement site at *Weissfluhjoch* and the study area of this project were assumed to be comparable. Furthermore, its value lay within the range of snow density values applied by Jonas et al. (2009) in the area of interest, and was therefore assumed to be appropriate.

As the IMIS snow depth measurements were provided at a 30 minute sample interval, the acquisition time of each of the S1 images, IMIS data could be matched with a maximum of 15 minutes offset. The mean of the matched IMIS snow depth values for each ascending and descending S1 flight track was then calculated.

A statistical comparison of the time series trends was performed using the following two approaches at nine locations. As performed in Lievens et al. (2021), both approaches were conducted, once by including snow-free conditions and once by excluding them. Nine IMIS locations were selected (see Fig. 2.1). A selection process was performed on the basis of the local elevation and land cover type. Environments located at higher elevations offered longer time spans of interest. All selected locations further featured the same land cover (non-vegetated) to enable more stable comparisons.

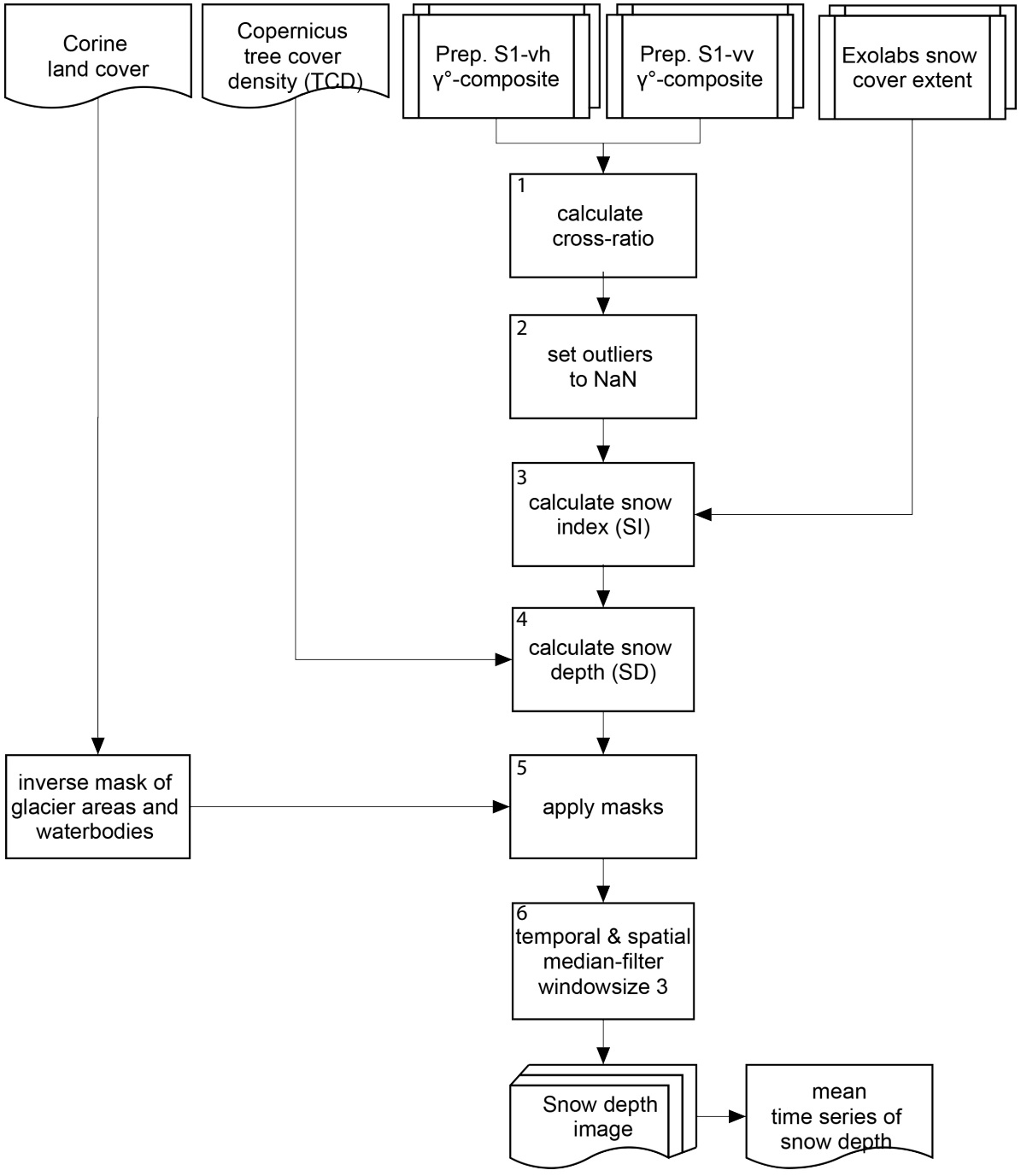

FIGURE 3.6: Processing chain as was performed for snow depth extraction. Intermediate products, generated in an earlier flowchart, are indicated using rectangular features with double bars at the sides.

3.5.2.1 Temporal Pearson Correlation Coefficient

Validation was conducted by following the process as described in Lievens et al. (2019). A temporal Pearson correlation coefficient (R_t [−]) was calculated between the validation data (SD_{SWE} or SD_{IMIS}) and the retrieved snow depth (SD_{S1}). This correlation coefficient describes the strength of the association between the temporal variability of two data sets (Derrick et al., 1993). Its value ranges between -1 to 1, where -1 and 1 describe perfect correlation (amplitude and timing) and 0 indicates no detected relationship (Sedgwick, 2012).

For each of the selected IMIS stations, the *Rt* value was calculated by describing the relation between SD_{IMIS} and SD_{S1}, as well as the one between SD_{SWE} and SD_{S1} for spatial resolution equal 100 m or 1000 m. IMIS point data was only available up to September 2019, so, the correlation coefficient was calculated between SD_{IMIS} and SD_{S1} for the time range before, whereas the one describing the relation between SD_{SWE} and SD_{S1} includes the whole time span. Calculation was performed by applying the following equation, where $\overline{A}$ and $\overline{B}$ are the mean values of arrays A and B.

$$R = \frac{\sum_m \sum_n (A_{mn} - \overline{A})(B_{mn} - \overline{B})}{\sqrt{\sum_m \sum_n (A_{mn} - \overline{A})^2 (B_{mn} - \overline{B})^2}} \tag{3.16}$$

3.5.2.2 Granger Test

The second validation approach applied an open source Granger test (Chandler, 2021). The Granger framework originated within economics (Granger, 1969). Its outcome describes how well one variable's time series can be used to *forecast* a second variable (Roebroeck, 2015). No strict causality is necessarily implied, which is why we prefer the term Granger test over Granger Causality test. However, it infers causal influences between two variables. The test has already been selectively applied in the context of remote sensing applications (e.g. Feldman et al., 2020; Núñez-Casillas et al., 2009). In this framework, the test enables the user to quantify the degree in which an environmental factor of interest forecasts the remotely measured data (Feldman et al., 2020).

The output of the Granger test is a value of the performed F-statistic as well as a so-called critical value (Chandler, 2021). The latter is mainly dependent on the defined confidence interval. It describes the value on the test distribution, which must be surpassed, to accept the working hypothesis (accept H_1, as defined below). In cases where the resulting F-value is lower than the critical value, the null hypothesis (H_0) of the factor to *not* forecast the measured signal is accepted and the working hypothesis (H_1) rejected.

For this thesis, the Granger test was used to quantify the effect of the independent snow depth estimate on (a) the measured S1 signal and (b) the corresponding snow depth retrieval. Therefore, both relations were examined: S1 to point measurements from IMIS stations, and SWE based snow depth to S1-based snow depth retrievals. In each case, the locations of nine selected IMIS stations were used. This approach enables a spatially consistent treatment of the full study area.

The hypotheses were set as follows:

- Null hypothesis:
  A.0) Snow depth measurements from IMIS (SD_{IMIS}) do not Granger forecast snow depth retrieved from S1 backscatter (SD_{S1}).
  B.0) Snow depth retrieved from S1 backscatter (SD_{S1}) does not Granger forecast snow depth calculated based on the SWE model (SD_{SWE}).

- Working hypothesis:
  A.1) Snow depth measurements from IMIS (SD_{IMIS}) Granger forecast snow depth retrieved from S1 backscatter (SD_{S1}).
  B.1) Snow depth retrieved from S1 backscatter (SD_{S1}) Granger forecasts snow depth calculated based on the SWE model (SD_{SWE}).

The confidence interval was set to 95%. This ensured a statistically relevant statement in cases where the working hypothesis was accepted. Eighteen days were set as the maximum delay (four composites) allowed for the forecasting from IMIS to S1, whereas 30 days were allowed between S1 snow depth to forecasts of SWE based snow depth. This values were defined, based on correspondence with T. Jonas from SLF and enabled to account for one month delay of snow depth detection from SWE, due to included percolation effects.

4 Results

In this chapter, an overview is provided on the achieved results for LRW-composite testing, reference image generation and snow depth retrieval. Fig. 4.1 displays a time series of the input data sets, which were used for the generation of the results. For clarity, the resulting images are primarily shown at 1000 m and 30 m resolutions based on the winter season reference image. When results are similar and visual differences minor across polarization states, co-polarized data is shown. In cases where relevant discrepancies between further reference image types, resolutions or polarization states were found, these are included. Mean statistics are presented.

4.1 Local Resolution Weighting-based composite time series

The homogeneity of LRW composites was tested by inter-comparing backscatter time series across diverse aspect orientations. In a first attempt, mean time series were calculated, displayed and summarized for selected aspects(4.1.1). Time series were generated that were restricted to a mean across snow covered pixels present in the composite (4.1.2). The effect of land coverage and elevation was examined by creating and analyzing corresponding time series.

4.1.1 Mean S1 backscatter over study area

Fig. 4.2 shows the mean backscatter evolution over time for selected slope orientations within the study area in each polarization channel. Samples characterized by a slope degree below 15% were not considered.

To enable comparisons, a temperature curve was produced based on the improved temperature information (described in 3.2.2) and included for the standard elevation of 2500 m.a.s.l.. It is based on a mean calculated across the test site of interest. The temperature behaviour over time indicates that the winter in 2018 had colder temperatures over a longer period than those in 2019 and 2020 (see Fig. 4.2). The temperature amplitude reached a minimum in the time series in February 2018 of -14.5 °C. The lowest temperatures in 2019 occurred at the end of January, reaching -12 °C. The winter of 2020, however, was characterized by relatively warm temperatures at 2500 m.a.s.l., whereby temperatures oscillated around the freezing point throughout the season, barely staying below the freezing point even over short periods of only a few days, i.e. over multiple composites.

The mean of study-area wide VV-backscatter information sampled at 1000 m ranged between -8 to -10 dB over the observed time frame of 2018 - 2020 (see Fig. 4.2). A drop of backscatter is observable during spring of each year. The drop was thereby most sudden and distinctive in 2018 (from -8.5 to -10 dB within one month) and comparably weak and lagging in 2020. The springtime decrease of backscatter during 2020 featured no clear starting point and reached minimum VV-backscatter of -9.5 dB on East and South facing slopes.

The progression of the study-area wide VH-polarized backscatter took place between -13 and -16 dB (see Fig. 4.2). The trend is comparable to the VV-polarization data reported above. A decrease in backscatter through spring is followed by an increase in backscatter throughout summer before the backscatter gradually declines again at the start of autumn.

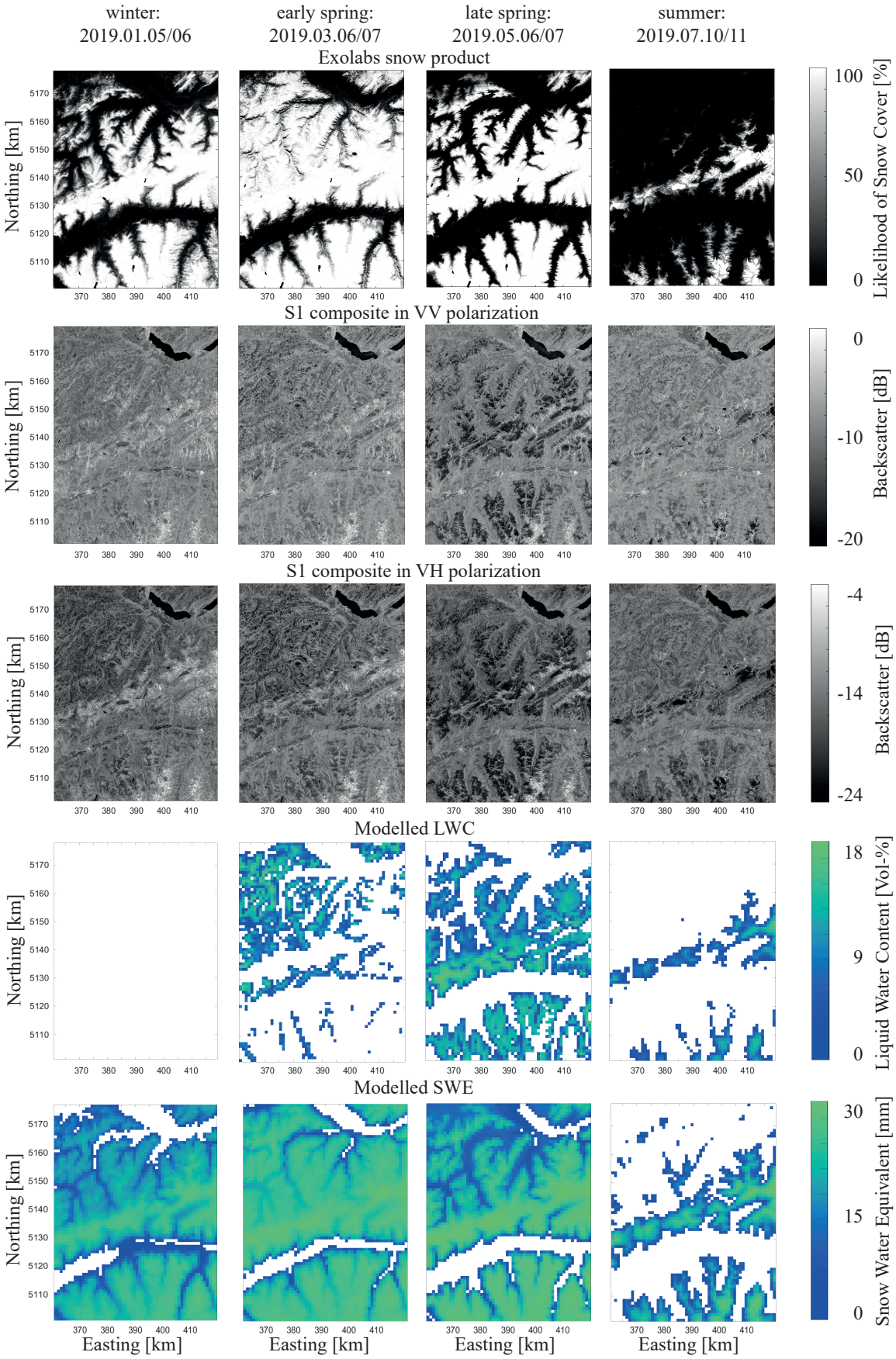

FIGURE 4.1: Input data set time series displaying Exolabs snow cover product (30 m GSD), S1 γ_c° images (30 m GSD) in VV- and VH-polarization as well as modelled liquid water content (LWC) and snow water equivalent (SWE) data (1000 m GSD). To enable comparison, mean images were calculated for snow cover, SWE and LWC over the two days of S1 acquisition.

During summer 2018, a pronounced feature was observable in all slope orientations, where the backscatter alternated from composite to composite (at 6 day intervals) with a difference of approximately 0.5 dB. This feature was also detected in the summers of 2019 and 2020, however it was less pronounced then.

During winter seasons, an increase in VH/VV-polarization dB difference was detected. During summer seasons, the dB difference's temporal evolution was highly comparable across all slope orientations, with a minor decrease towards the start of the winter season. An oscillation was visible due to the alternating feature already discussed above, also at VV-polarization.

Measured information from data facing North, featured 0.5 dB higher values than the remaining three slope orientations at both VV- and VH-polarization. Also, the dB differed in the same way, when tracking the data sampled with 1 km intervals. This behaviour was, however, not consistent over the diverse resolutions. At 100 m, the difference in amplitude was insignificant for VV- albeit not in VH-polarization. For the latter, a very similar response of backscatter was found in 100 m data, when compared to 1000 m spaced information. At both polarizations, data from 1000 m grid indicated that North-facing slopes tended to have a less abrupt decline of backscatter and a later arrival at its minimum than did slopes oriented in other directions. At a 30 m sample interval, the effect was found during winter, but not during summer. However, South facing slopes were continuously 0.5 dB below average.

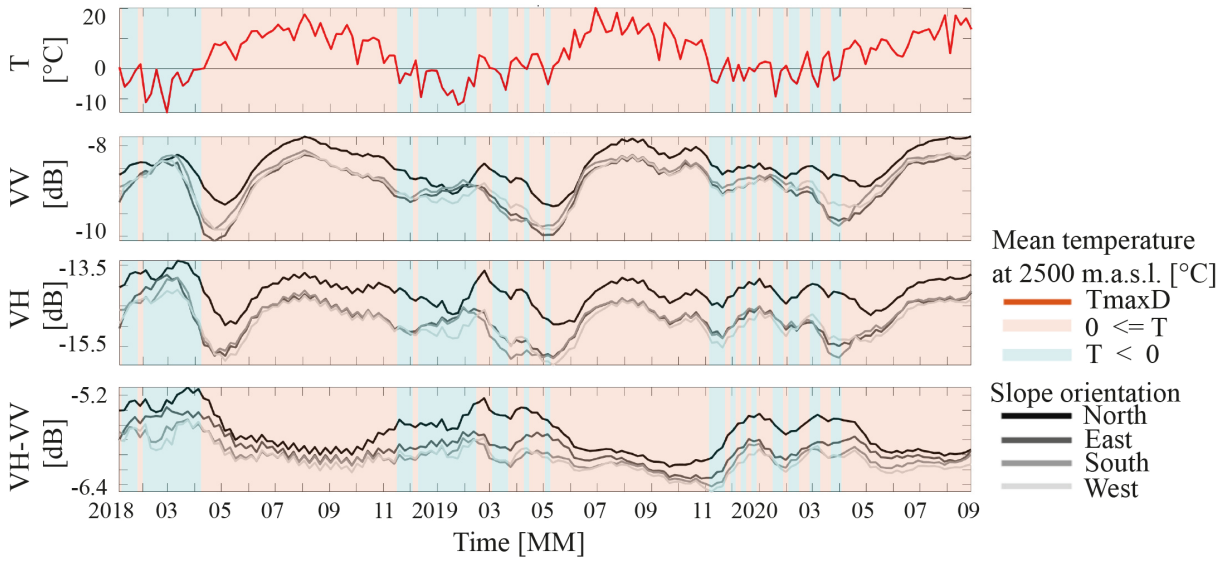

FIGURE 4.2: Time series of S1 backscatter in relation to slope direction and in comparison to temperature at 2500 m.a.s.l.. Samples are masked out if belonging to a water body or if situated in a plain (slope below 15%). The number of 1000 m samples taken into consideration at 1000 m resolution were North: 332, East: 360, South: 228 and West: 449.

4.1.2 Mean S1 backscatter of snow covered pixels and influencing factors

Fig. 4.3 displays the S1 backscatter time series for snow covered pixels in dependency of three variables: 1) aspect orientation, 2) elevation and 3) land cover class. As snow coverage was determined by using optical imagery, the time series was investigated within the time frame of two years, where all data sources were available.

The first plot indicates temperature progression over time. Based on this progression background, colour-shading was set across all plots. The shading indicates the relation between the temperature at 2500 m.a.s.l. and the freezing point (red above, blue below).

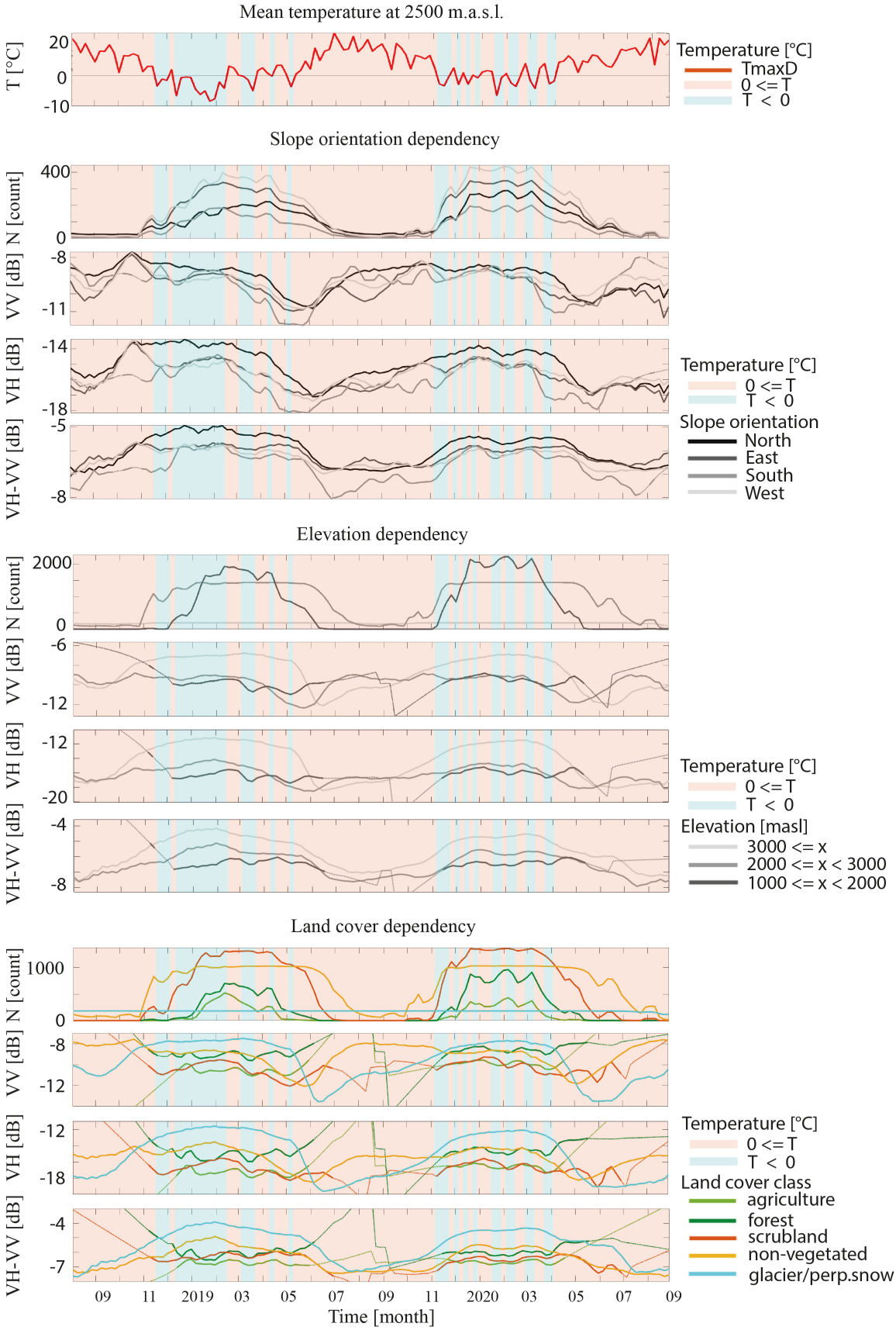

FIGURE 4.3: Mean time series (Sept. 2018 to Sept. 2020) of S1 backscatter for snow-covered pixels in dependency of 1) aspect orientation (subplots ii-v), 2) elevation (subplots vi-ix) and 3) land cover class (subplots x-xiii). First subplot (i) shows the mean 2500 m temperature over time. The shading for all subplots is based on this temperature in relation to the freezing point during the S1 acquisitions.

For each dependency of interest (see defined above 1-3), the number of samples (N) within the classes was plotted over time to enable a discrimination of the significance of the correspondingly received backscatter trend (subplots ii, vi, x). Second, the VV-polarized backscatter behaviour per class was drawn (subplots iii, vii, xi), followed by the progression of the VH-polarized information (iv, viii, xii) and the corresponding VH/VV-difference (v, ix, xiii) over time.

The aspect orientation (dependency 1) was characterized by reliable numbers of samples during the winter and spring seasons. However, especially the number of South oriented samples were of statistical insignificance during summer (see Fig. 4.3). Generally, South-facing slopes featured the smallest number of snow-covered samples, whereas the classes of West and East facing aspects featured around 400 samples each during winter.

The behaviour of snow-covered pixels across all polarization states varied less than 1 dB across the aspect directions. However, North-facing slopes generally resulted in above average backscatter values, whereas South facing aspects generally featured below average values. Both polarization states measured were characterized by a decline during spring, which occurred across all aspects. The intensity of this signal's decrease varied, however, and the cross-polarization ratio resulted in higher values during winter, gradually decreasing over the melting season until it reached minimal values at the beginning of autumn. Low values of the VH/VV-difference were present during summer, before increasing again towards an advancing winter season.

A temporal offset in minimal backscatter measurements was found across slope aspects. North facing slopes indicated later melting events, as the measured backscatter minimum is reached with a two-week delay compared to South facing aspects.

To investigate the dependency of a time series in relation to elevation (dependency 2), three classes of elevation were assigned and their mean time series generated. Across those, areas above 3000 m.a.s.l. were continuously covered with snow, whereas the amount of available snow-covered pixels below this elevation threshold were restricted to the winter seasons. Backscatter within high alpine regions had the highest variations over the time series. A sudden decrease in backscatter was found in each time series during the start of spring. However, the timing of this event was delayed and the amplitude increased with the rising elevation. The backscatter ratio reached lower dB values during summer and gradually increased towards midwinter before decreasing again towards the next summer.

Distinct differences across land cover classes as aggregated from CORINE land cover classes (see chapter data) were detected (dependency 3). The significance of backscatter over forest and agricultural areas, however, was minor, due to restricted snow coverage. The strongest amplitudes in all three polarization channels were detected in the class of glacier and perpetual snow, followed by non-vegetated class and then scrubland. Each of these three classes indicated a decrease of the measured backscatter signal during spring. Thereby, the decrease in backscatter over scrubland was restricted to 1 dB over one month, whereas the backscatter over glacier and perpetual snow covered regions dropped 4 dB between May and June.

4.2 Performance assessment of dry snow reference images

Quantification and analysis of the influence of the chosen generation procedure of dry winter reference images was performed by mapping wet snow based on corresponding reference images and assessing the resulting validity. This was tested by comparing wet snow maps to an independent reference data set that modelled the local LWC.

4.2.1 Resulting reference image

Three approaches for generating a reference image were tested: 1) a single 36 h composite, 2) an image calculated as the median of three composites and 3) an image calculated as the local median over a winter season (Dec-Feb). Each approach was tested at three spatial resolutions (1000, 100, 30 m) and two polarizations (VV, VH).

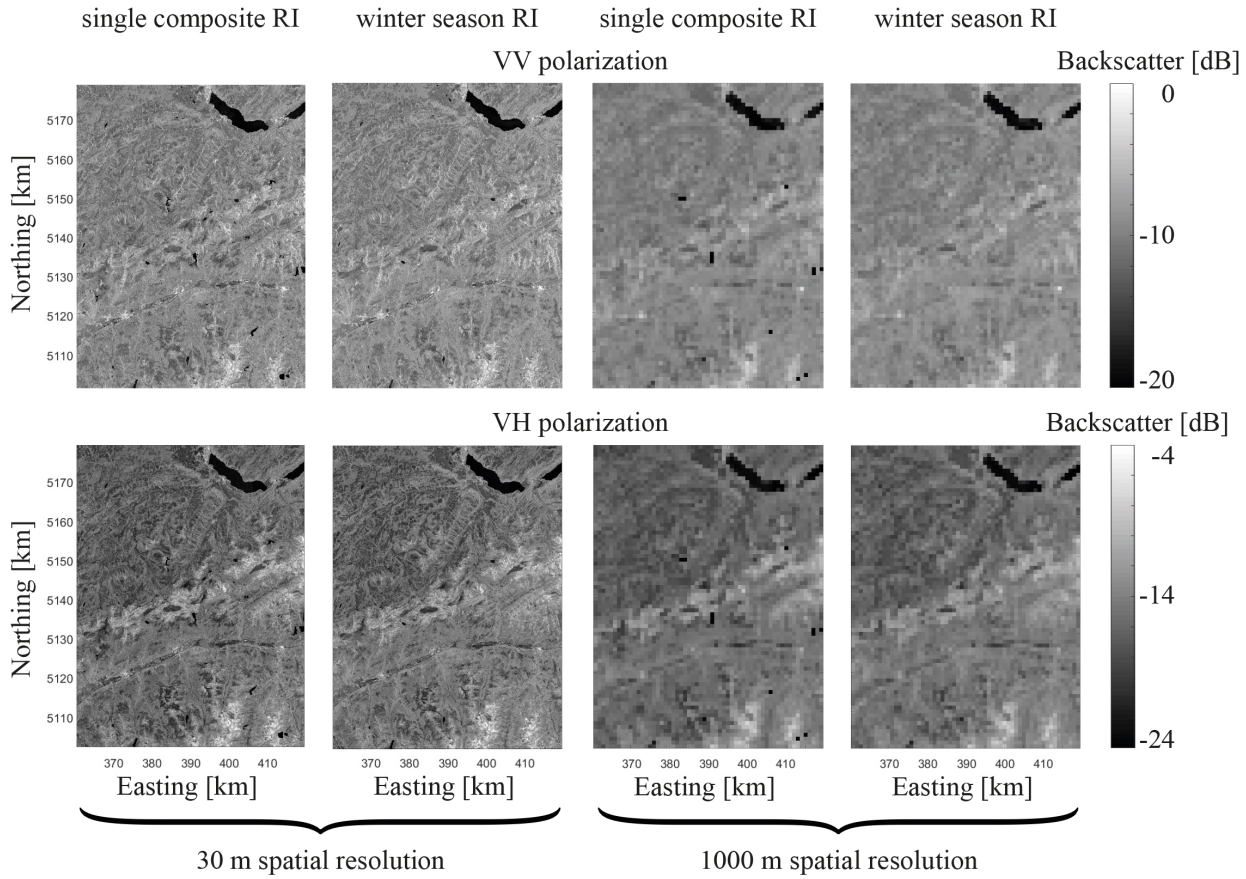

FIGURE 4.4: Reference images based on a single composite and median winter season approaches. The displayed examples show VV- and VH-polarization at 30 and 1000 m spatial resolution.

Fig. 4.4 shows an overview of a selection of the resulting reference images in comparison (non-selected images are included in the appendix, see A.2 and A.3). By cross-comparing diverse aspects, the magnitude of the following effects was observable: i) spatial resolution ii) polarization and iii) reference image generation method. A decline in spatial resolution (left vs. right quartet in Fig. 4.4) resulted in a smoothed view of the area. Between 30 and 1000 m this was observable by visual comparison and was indicated by both a loss of small features, as well as a reduction of extreme values, with increasing GSD. The best visible influence of polarization (top vs. bottom row) was the occurring change in amplitude. The mean across the test site decreased about 6 dB between the VV- and VH-polarized channels. The most prominent effect of the applied approach (left vs. right columns) were the gaps occurring in the single composite mode. These gaps, indicating the locations, where dry/no-snow conditions were not met during the acquisition, were set to voids.

Fig. 4.5 shows the results of wet snow mapping at 30 m resolution by indicating the progression over the melting season of 2019 (March-June). Optical snow cover likelihood is presented to enable an assessment of the plausibility of the resulting wet snow maps. The resulting maps showed similar results per composite, however, a general trend toward more detected wet snow was found when using the winter season approach in comparison to using a single composite as the reference image.

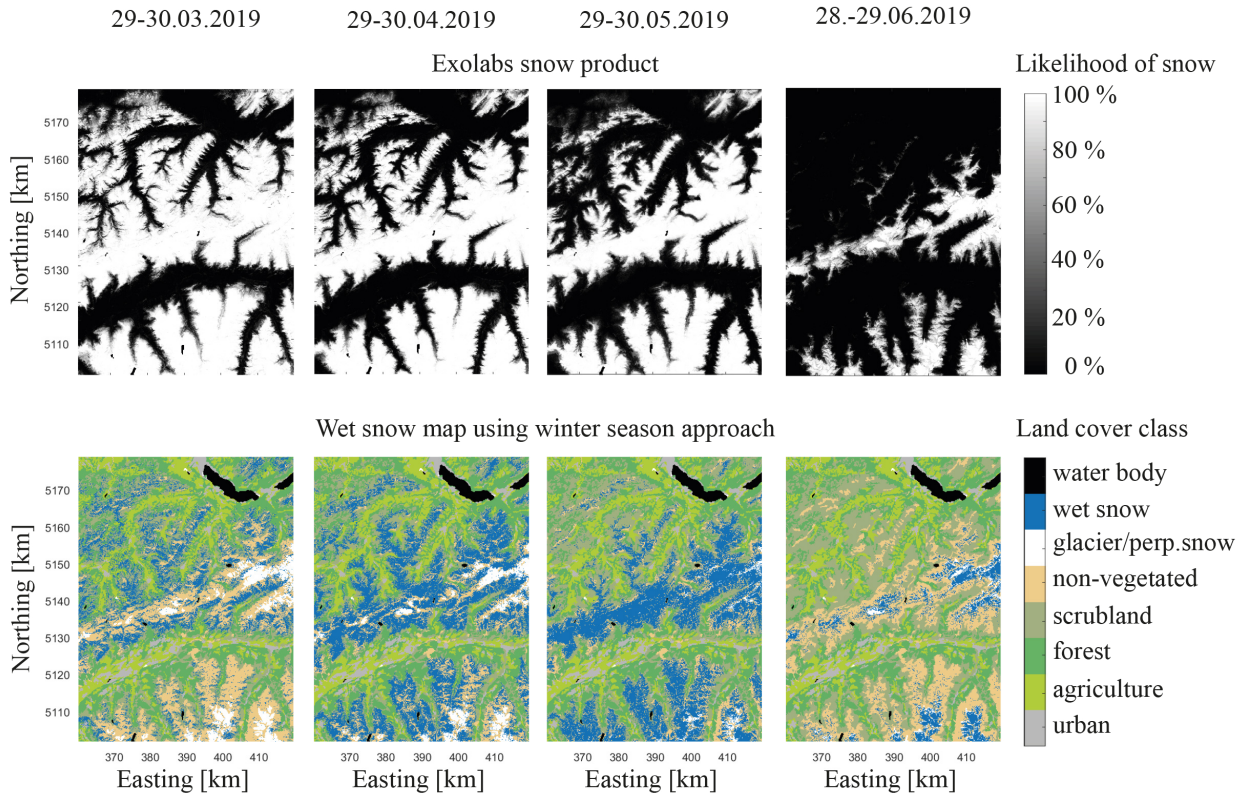

FIGURE 4.5: Example of time series of 30 m GSD optical images (top row), detected wet snow maps from VV-polarization plotted over local land cover (second row).

4.2.2 Validation of coarse resolution reference images against modelled liquid water content (LWC)

Statistical validation against LWC maps was only viable at 1000 m and 100 m sample intervals. An overview of the multiple time series enables a visual insight into the results and is shown in Fig. 4.6.

Tab. 4.1-4.4 provide an overview of the achieved mean values of the statistical results for overall accuracy (OA), Cohen's kappa coefficient (κ), error of commission (EoC) and of omission (EoO) of wet snow for the time period from Sept. 2018 to Sept. 2020. Overall accuracies across examined polarization channels and spatial resolutions (see Tab. 4.1) varied between 0.910 and 0.926. For VH-, a 1% higher mean value was achieved than in VV-polarization. κ values ranged from 0.458 to 0.513. This indicates that the conducted classification performed around 0.5% better than a random classifier (Lillesand et al., 2015). This achieved level of agreement, κ, between LWC and retrieved wet snow locations from S1 is to be understood as 'weak' or 'moderate' (see tables in McHugh, 2012; Viera et al., 2005).

4.2.2.1 Spatio-temporal error distribution

Time series of confusion maps were created to allow an examination of the spatio-temporal behaviour of the observed errors. Fig. 4.6 illustrates a four month time range during the melting season of 2019, using a full winter season reference image. Displayed are optical snow cover likelihood images, detected areas featuring wet snow, and error maps at two different thresholds for LWC.

Median accuracies at 1000 m GSD, time frame: Sept. 2018 to Sept. 2020

Table 4.1: Overall accuracy [-]

RI approach	Polarization VV	VH
single composite	0.922	0.915
median of three	0.926	0.911
median of winter season	0.925	0.910

Table 4.2: Cohen's Kappa coefficient [-]

RI approach	Polarization VV	VH
single composite	0.458	0.488
median of three	0.463	0.508
median of winter season	0.474	0.513

Table 4.3: Error of commission [-]

RI approach	Polarization VV	VH
single composite	0.344	0.494
median of three	0.497	0.610
median of winter season	0.443	0.606

Table 4.4: Error of omission [-]

RI approach	Polarization VV	VH
single composite	0.425	0.322
median of three	0.395	0.284
median of winter season	0.399	0.290

The distribution of classification errors across space was representative for all three examined years and similar across the three tested reference image approaches. Notably, wet snow areas were more often detected on South facing slopes than in other aspect orientations.

Cross-comparing statistics, a higher accuracy was achieved in all but some errors of commission, when using the 3% LWC threshold for the validation data. Lowlands and high elevation areas were generally properly classified as no or dry-snow occurs, respectively. During early melting, differences between S1 retrieval and the independent reference LWC dataset were found in the northwestern part of the test area, where S1 retrieval suggested wet snow occurrence while LWC data did not. Steep east facing slopes, however, generally indicated the contrary case. Both types of differences were mainly situated on mid elevations. With further losses of snow coverage over time the area rightfully classified as "no snow" increased. Errors of omission still edged correctly classified wet snow in high elevations. However, errors of commission disappeared, until they reappeared in September.

4.2.2.2 Error distribution in relation to land cover types

Bar charts, shown in Fig. 4.7, illustrate the relative numbers of errors of commission and omission per land cover class. Colours thereby indicate the seasonality of error occurrence. The errors generated are illustrated. A full winter season reference image was used; a liquid water content threshold of 3% was applied.

The likelihood of an error of commission decreased, when using a single composite instead of the full winter approach. However the number of errors of omission increased. VV-polarized data generally performed better by both scoring fewer errors of commission and omission than VH-polarized data. The effect was more distinct when comparing polarization results within errors of commission than within errors of omission.

A difference of error distribution across land cover classes was found. Few errors occurred in urban areas. This correlates with this class having lost the most samples during the discharging of pixels featuring below a 15% slope. The distribution of errors of omission was characterized by a distinct majority in the scrubland class, followed by forested regions. Errors of commission, however, were mostly detected over non-vegetated areas.

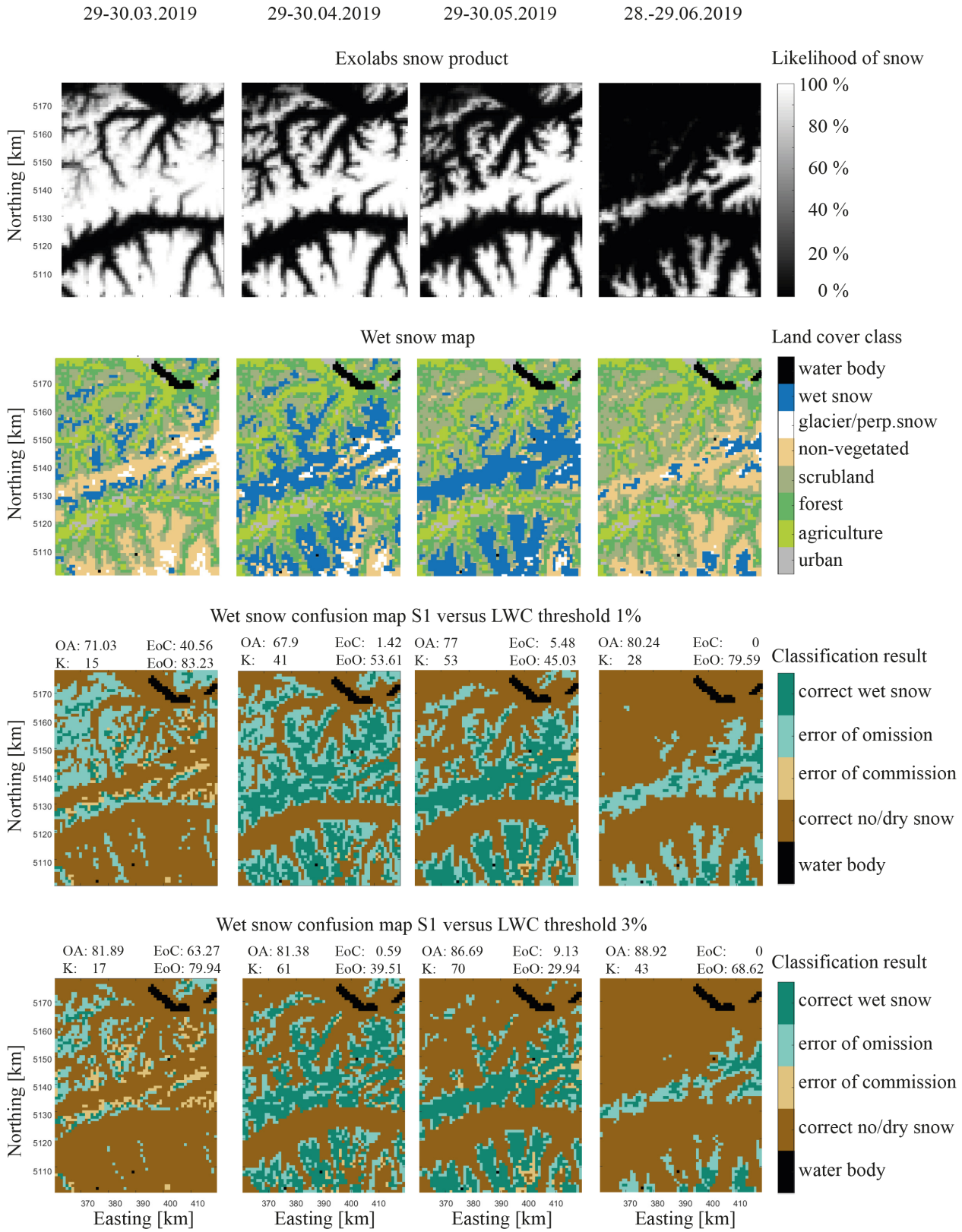

FIGURE 4.6: Example time series at 1000 m GSD of snow cover likelihood maps (top row), detected wet snow maps from VV-polarization (second row), and maps of achieved accuracies (last two rows). Validation was performed against LWC data, which had been thresholded at 1% (third row) and at 3% (fourth row). Achieved statistics (overall accuracy (OA), Cohen's kappa coefficient (κ), error of omission (EoO) and error of commission (EoC) are displayed on top of corresponding confusions maps and provided in percentages.

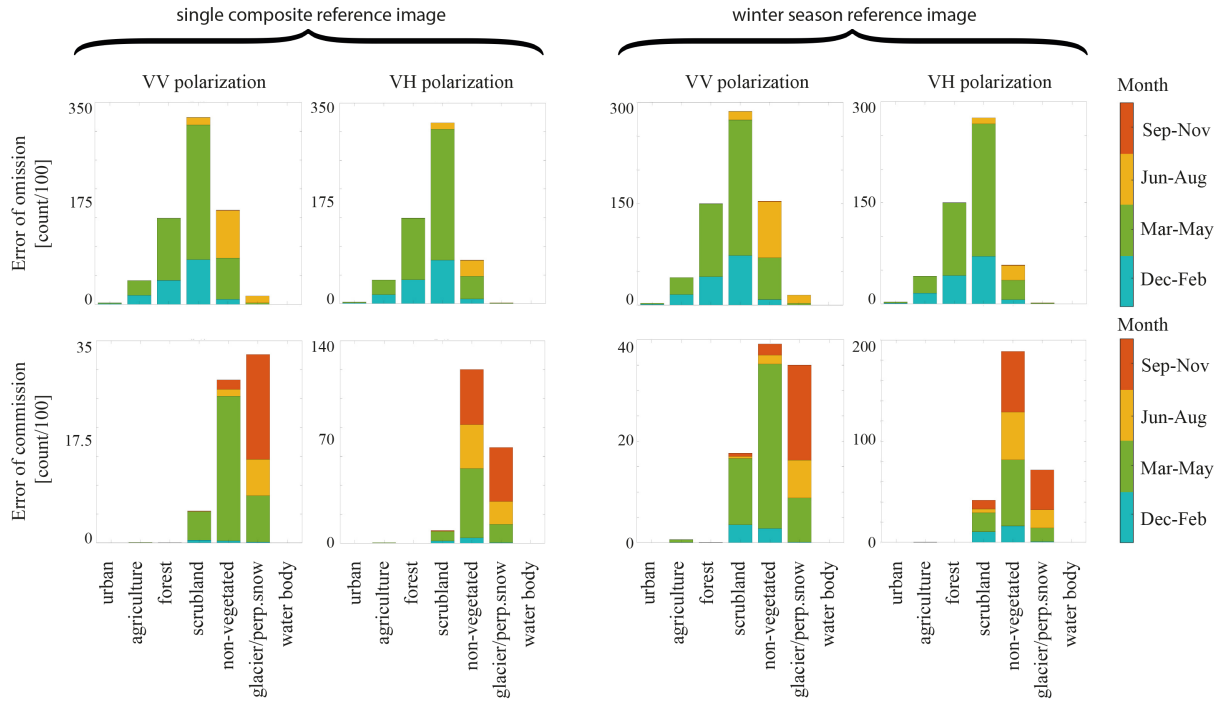

FIGURE 4.7: A selection of bar charts showing the error occurrences (commission and omission) in relation to land cover class. Colour indicates the season when the corresponding errors were generated.

These were followed by the generally higher elevated areas characterized by glacier and perpetual-snow. In cases of a single composite image approach or a LWC threshold of 1%, non-vegetated areas had a lower number of errors of commission than did regions covered by glacier or perpetual snow.

Further analysis indicated that a variation in the applied LWC threshold led to a redistribution between errors of omission and commission. Using a lower threshold led to a decrease in the number of errors of commission and to an increase in errors of omission.

4.2.2.3 Error distribution in relation to seasonality and slope orientation

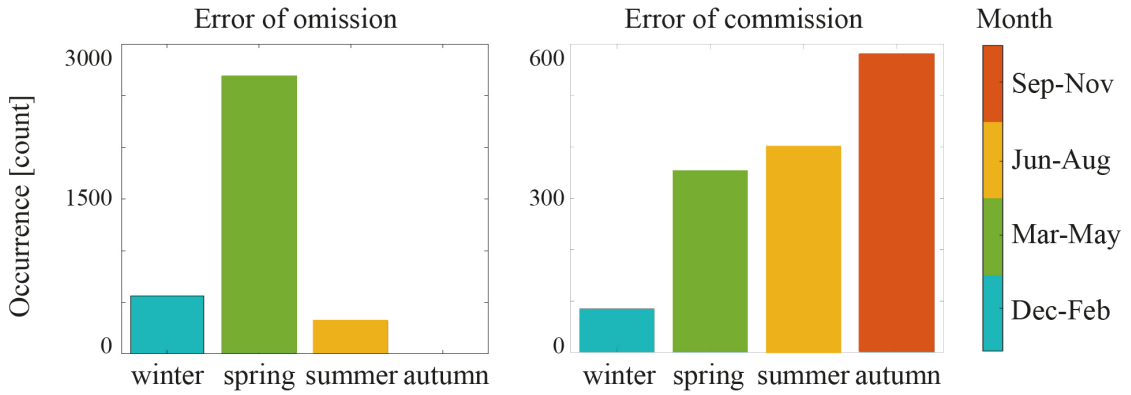

FIGURE 4.8: Bar charts showing the error occurrence (commission and omission) in relation to aspect orientation at 1000 m scale. LWC was taken for reference with a threshold of 3 Vol-% and S1 wet snow maps as input. Colours indicate the season, in which the corresponding errors were found.

The influence of seasonality and aspect on error distribution of VV- and VH-backscatter is illustrated in Fig. 4.8. The amplitudes of error occurrences varied strongly. While the highest amount of errors

of omission numbered up to 2'900 in spring, the misclassifications of errors of commission reached its maximum in autumn with nearly 600. Most errors of both omission occurred during spring (Mar-May), indicating most melting to occur during spring (melting season). Differences between S1-based retrievals and the independent reference information during autumn were mainly errors of commission caused by the reset in the LWC model: The LWC model is set to zero every September to enable building-up a new snowpack for the upcoming season.

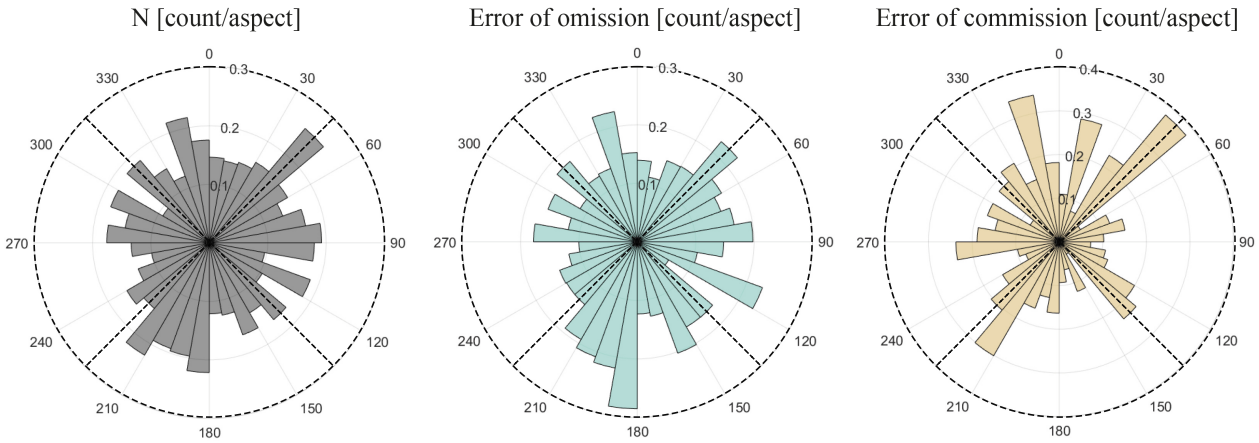

FIGURE 4.9: Polar histogram showing the normalized error occurrence (commission and omission) in relation to the local aspect (36 bins, each bin containing 10°) at 1000 m GSD using VV-mode. The samples per aspect indicate the probability of samples (N) and errors (EoC, EoO) to be classified into the corresponding aspect bin over the observed time and are as such comparable to the bar charts in Fig. 4.8. Striped lines indicate the aspects which were defined as North (top), East (right), South (bottom), West (left) during time series generation in Fig. 4.2 and 4.3.

The polar-histograms in Fig. 4.9 enable an analysis of the distribution of errors in relation to their aspect. Normalization was performed by using a probability density function, where each bar height was re-scaled as follows (MathWorks, 2021):

$$bin\ height = \frac{number\ of\ observations\ in\ bin}{total\ number\ of\ observations\ *\ width\ of\ bin} \tag{4.1}$$

The first plot shows the distribution of all samples across the test site, which were used for the generation of the slope-dependent time series. A majority of samples were identified to be facing towards South-South-West (classified as South). The distribution of errors of omission was found to assimilate this spatial-pattern. Errors of commission appeared to be under-represented in the direction of South-East, with the exception of the slope-class 120-130°. Of notable interest was also the amplitude at 210-220°.

4.2.2.4 Temporal behaviour of differences between S1-based retrievals and independent reference data set

Fig. 4.10 and 4.11 indicate the temporal changes of the calculated statistical measures for each reference image approach, in comparison to the number of snow covered pixels detected using optical images (top row).

During all three observed melting seasons (April to July, 2018-2020), whenever the reference image was set to single composite images, a general trend towards lower overall accuracy, Cohen's kappa coefficient and higher errors of omission was observed in comparison to RIs' based on a median of three or on a median over the full winter season. Fewer errors of commission, however, were

achieved by the single composite approach, when compared to the others. No conclusive trend was observed between the progression of accuracy measures between median of three and median of the full winter season. However, an increase in differences between the performance of single composite, median of three, and the winter season approach was found over time (see Fig. 4.10 and 4.11).

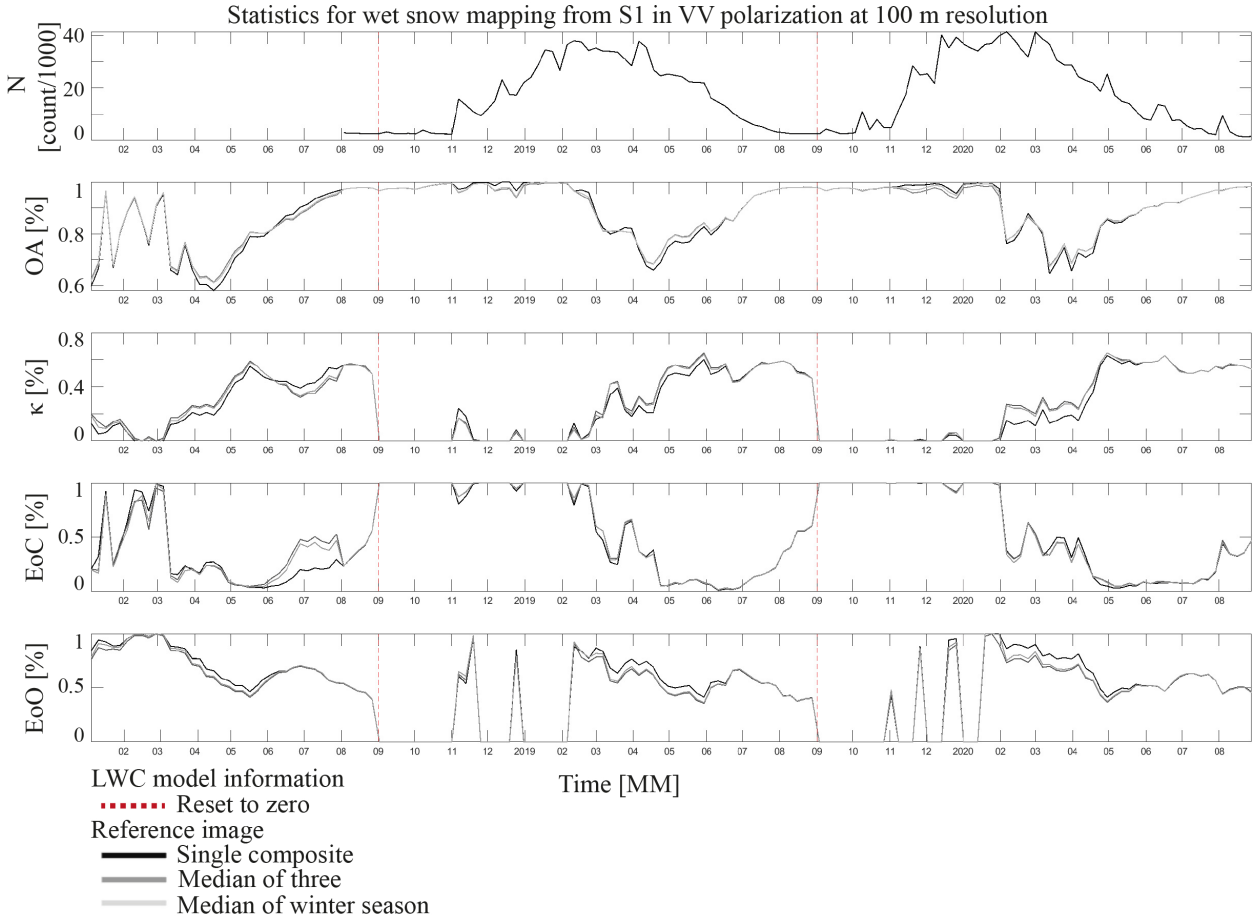

FIGURE 4.10: Achieved statistics over time in VV-mode in comparison to the number of snow covered pixels from optical imagery at 100 m GSD. Displayed are the temporal behaviours of the overall accuracy (OA), Cohen's kappa coefficient (κ), error of omission (EoO) and error of commission (EoC) at 1000 m GSD using VV-mode. S1 data for wet snow retrieval.

Relevant discrepancies between VV- and VH-polarized information were detected in summer seasons (compare Fig. 4.10 and 4.11). The error of omission from VV-polarized data strongly increased starting in June (especially in 2018), reaching a high in July, where EoO came to a value above 0.6%, before decreasing again to 0 at the beginning of September. However, no such behaviour was observable within VH-polarization information. Accordingly, κ indicated double the accuracy during July 2018, when VH- ($\kappa = 0.8\%$) was used instead of VV-mode ($\kappa = 0.4\%$).

Strongly effected by low resolutions were the statistical measures during summer. Due to the availability of only a few samples of positive detection of wet snow in the independent validation data, a single misclassification weighed strongly on the "statistical" error measures (compare appendix A.4 and A.5). The resulting fluctuations were visible in 1000 m GSD calculations but diminished strongly at increasing spatial resolution (100, 30 m), as many more samples were available. For this reason, we displayed the 100 m data here.

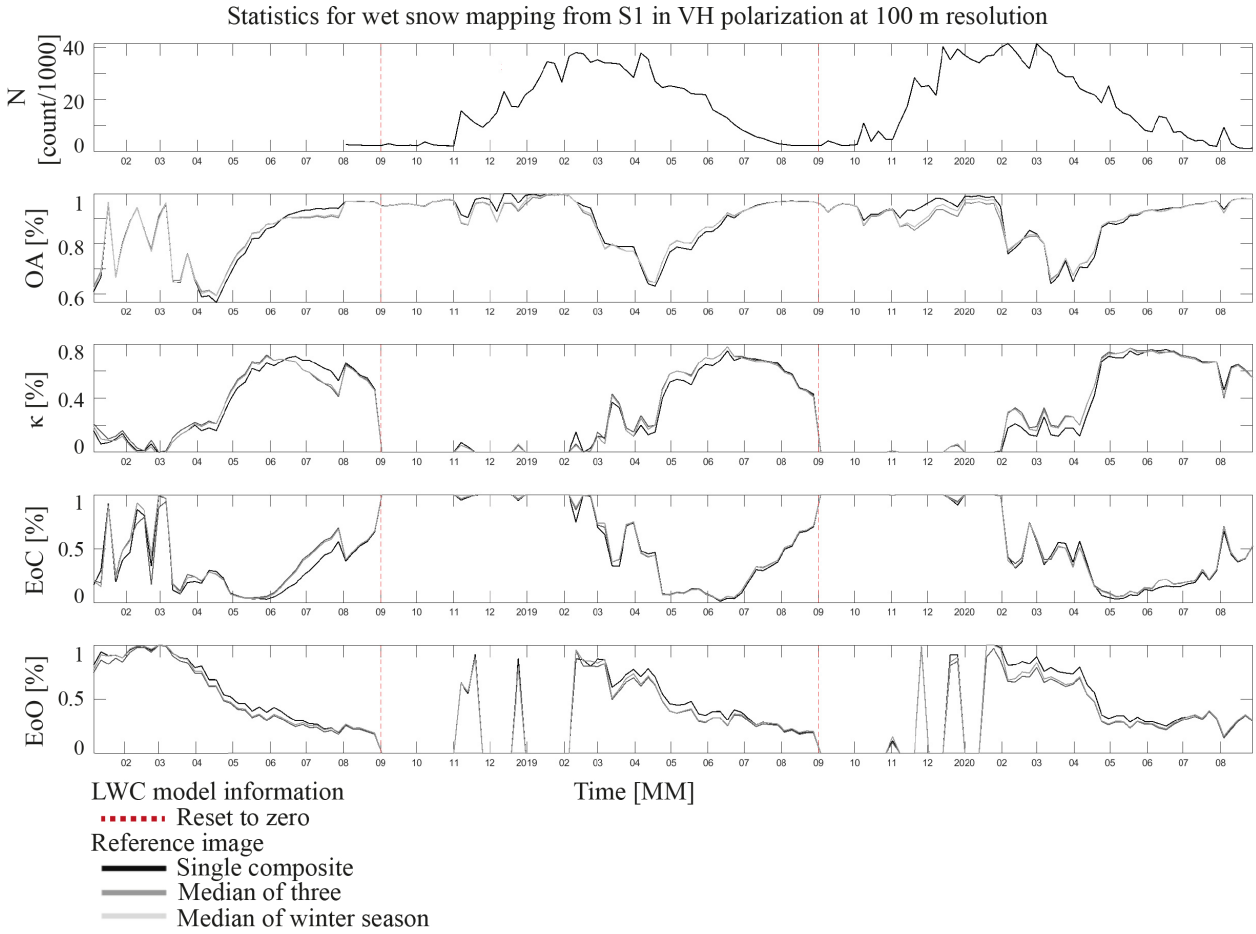

FIGURE 4.11: Achieved statistics over time based on VH-LRW composites in comparison to the number of snow covered pixels from optical imager at 100 m GSD. Displayed are the temporal behaviours of the overall accuracy (OA), Cohen's kappa coefficient (κ), error of omission (EoO) and error of commission (EoC) at 1000 m GSD.

4.3 Snow depth retrieval

As input for the retrieval of snow depth from S1, the γ_c° composites (VV- and VH-polarization) and the snow cover extent from the optical snow cover product were used. Additionally, the aggregated CORINE land cover classes and the Copernicus tree cover density information were used (see chapter 2.6). The results from snow depth retrieval using γ_c° composite backscatter time series as input are shown in Fig. 4.12, 4.13 and 4.14 for 1000 m and 30 m, respectively. Each plot shows the snow depth time series retrieved from the composites with their temporal sample interval of six days. The validation was performed on the nine illustrated locations of IMIS stations within the test site (see Fig. 2.1).

4.3.1 Temporal behaviour of retrieved snow depth

The range of values in a season of detected snow depth from S1 backscatter varied when different composite GSDs were compared. While a maximal snow depth of 9 m was retrieved at the GAN station at 2710 m.a.s.l. using 30 m GSD (see Fig. 4.14), the same location over a 1000 m grid indicated a snow depth below 1 m (see Fig. 4.12). Maximal snow depth at 1000 m GSD was retrieved at the location of VDS, where it approached 4 m. The location of STN showed the highest snow depth value in the 100 m grid with 8 m (see Fig. 4.13).

Except for the GAN and the DIA station in winter 2019, the amplitude of snow depth retrieved from S1 in comparison to the SWE model based retrievals were found similar at 1000 m GSD. Overall, larger discrepancies (1-2 m) were found, when comparing the 1000 m resolved data with point measurements (compare Fig. 4.12). This effect of amplitude offset between S1 retrievals and IMIS data was also visible at 30 m GSD, however, in the opposite direction. Whereas generally higher values were found at point scale measurements when compared to 1000 m GSD, the 30 m GSD indicated deeper snowpacks than the measurements. Visual comparison indicated the best level of amplitude agreement to be found in the 100 m resolved S1 data (see Fig. 4.13).

At 30 m GSD retrieved snow depth over time indicated fluctuations of up to 3 m within three composites (see Fig. 4.14) in both accumulative (e.g. station: TRU) and degradative direction (e.g. station: SAA). Such high fluctuations could not be found in the reference data. However, the timing in changes in snow depth coincide with temperature at both point scale measurements and areal retrievals (see Fig. 4.14).

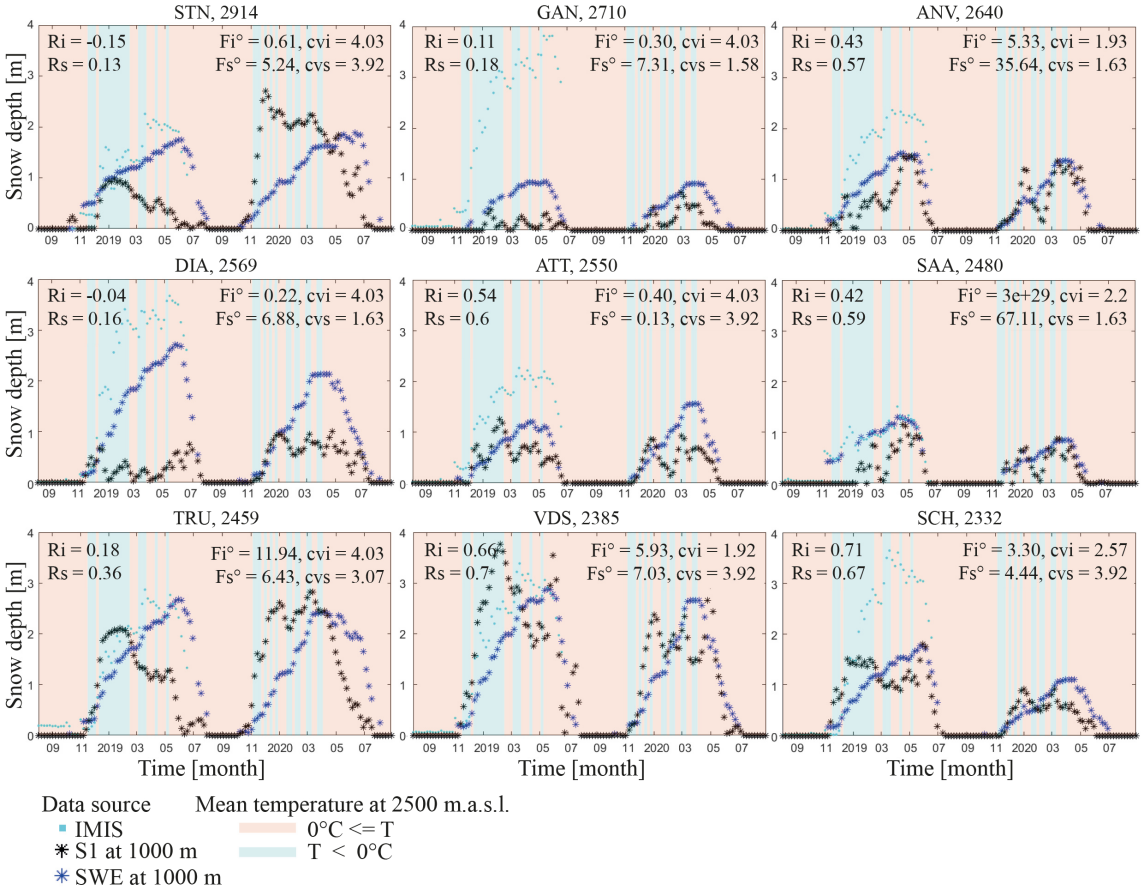

FIGURE 4.12: Snow depth time series retrieved from S1 backscatter, calculated from intermediate snow water equivalent estimate (both at 1000 m GSD) vs. values measured at IMIS stations (point measurements) in comparison. Each subplot represents an IMIS measurement location (station short name, elevation in m.a.s.l.): Stations are sorted by elevation. The shading colour indicates the daily maximum temperature at 2500 m.a.s.l. in relation to freezing point (red above, blue below, for more information see chapter 2.8). Top-left boxes depict the achieved Pearson Correlation Coefficients (R_t) between the S1 based snow depth retrieval and the local SD measured at the IMIS station (Ri, SLF, 2021b) and to SD calculated from SWE (Rs; SLF, 2021b). Top-right boxes display the calculated Granger test: F-score ($F°$) and critical value (cv) for corresponding comparisons. Values marked with '°' were calculated over the entire time series (including snow free conditions), those without were calculated solely on data acquired during snow coverage (masking was based on optical imagery, ExoLabs, 2021).

4.3.2 Validation

4.3.2.1 Correlation assessment

The correlation of the snow depth results was once tested including snow free coverage and once excluding data featuring no snow coverage (see Tab. 4.5-4.6). This masking was based on optical imagery. We displayed the results featuring correlation only during snow conditions, as this is of higher relevancy for the retrieval of snow depth using S1 imaging: By applying the snow index, no snow was masked using optical images not SAR (see the methods chapter). However, at 30 m resolution, both results (including and excluding snow free data in the calculation of the Pearson correlation coefficient (R_t)) are shown and the corresponding data at 100 and 1000 m GSD can be found in the appendix (see A.7 and A.6).

Achieved mean and median R_t between S1 retrieved snow depth and IMIS measurements as well as between S1 based retrieval and the SWE model based calculations are summarized in Tab. 4.5 and 4.6. The first table indicates statistics, when comparing the entire time series, whereas the latter displays the correlation results when only analyzing snow covered composites.

Tables featuring the mean and median resulting Pearson correlation coefficients (R_t) for snow depth retrieval from Sentinel-1, when including (Ri°) and excluding (Ri) snow free conditions.

TABLE 4.5: Ri°

	Spatial resolution [m]		
Reference source	1000	100	30
IMIS mean	0.63	0.69	0.72
IMIS median	0.69	0.74	0.75
SLF model mean	0.65	0.70	n.a.
SLF model median	0.72	0.70	n.a.

TABLE 4.6: Ri

	Spatial resolution [m]		
Reference source	1000	100	30
IMIS mean	0.32	0.49	0.39
IMIS median	0.42	0.51	0.57
SLF model mean	0.44	0.57	n.a.
SLF model median	0.57	0.59	n.a.

The comparison of the results, displayed in the two tables (Tab. 4.5 and 4.6), indicated a strong decrease in achieved correlation, when excluding acquisitions during snow free conditions. Depending on spatial resolution and stations, also negative R_t values between in-situ measurements and retrieved snow depth were received after the exclusion of snow free images (compare Fig. 4.12).

After the exclusion of no snow images, lowest R_t values between both S1 and IMIS data as well as S1 and SWE based snow depth resulted across all spatial resolutions at the STN station. At 1000 m GSD, the results indicated erroneous retrieval at the stations GAN and DIA, where retrieved snow depth repeatedly fell to zero, even-though both reference data sets indicated no such behaviour.

The difference between mean and median values varied between 0 and 20 % (see Tab. 4.5 and 4.6). Generally, larger distinctions were found between median and mean values (calculated using Equ. 3.2 and 3.3), when excluding data acquired during snow free conditions. The results achieved with mean values were continuously lower than median values (exception: SWE to S1 at 100 m GSD). Highest homogeneity was achieved at 100 m resolution.

Overall, correlation between IMIS point scale measurements and S1 retrieved snow depth increased with an increase of the applied GSD (see Tab. 4.5 and 4.6). The correlation between SWE and S1 based retrieval varied in mean, but not significantly in median values. The analysis of the progression of the S1 based snow depth retrievals and the calculated depths from the SWE model suggested results between 'weak' and 'strong' correlations, when the full time series was analyzed (McHugh, 2012). This was dependent on the resolution. An exclusion of data acquired during snow-free conditions resulted in a correlation which was to be understood as 'minimal' or 'weak' (McHugh, 2012).

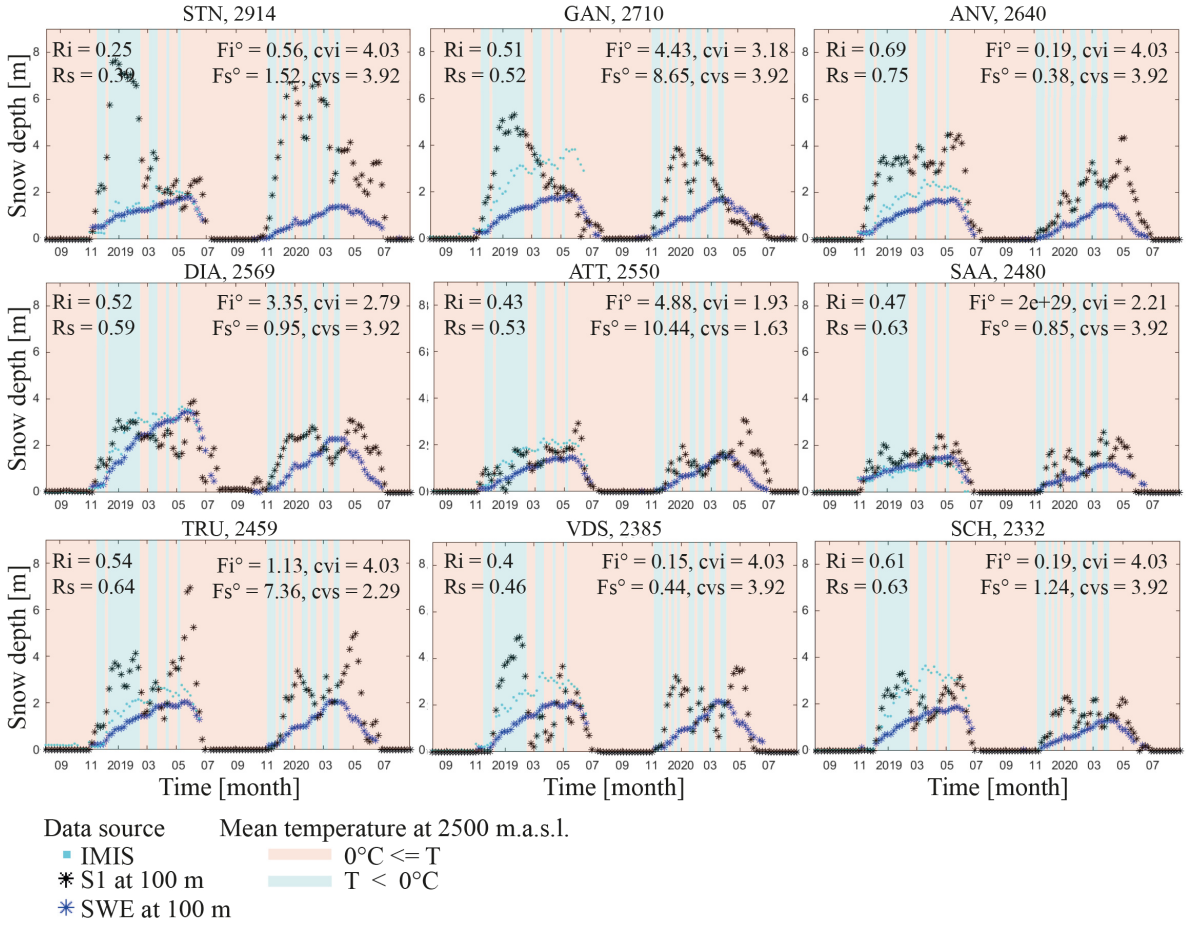

FIGURE 4.13: Snow depth time series retrieved from S1 backscatter, calculated from intermediate snow water equivalent estimate (both at 100 m GSD) vs. values measured at IMIS stations (point measurements) in comparison. Each subplot represents an IMIS measurement location (station short name, elevation in m.a.s.l.): Stations are sorted by elevation. The shading colour indicates the daily maximum temperature at 2500 m.a.s.l. in relation to the freezing point (red above, blue below, for more information see chapter 2.8). Top-left boxes depict the achieved Pearson Correlation Coefficients (R_t) between the S1 based snow depth retrieval and the local SD measured at the IMIS station (Ri, SLF, 2021b) and to snow depth calculated from SWE (Rs; SLF, 2021b). Top-right boxes display the calculated Granger test: F-score ($F°$) and critical value (cv) for corresponding comparisons. Values marked with '°' were calculated over the entire time series (including snow free conditions), those without were calculated solely on data acquired featuring snow cover (masking was based on optical imagery, ExoLabs, 2021)

4.3.2.2 Analysis of Granger forecasting relations

Specific Granger test results are indicated on the corresponding location at each GSD (see Fig. 4.12, 4.13, 4.14, and further in the appendix). The median values achieved in Granger tests are summarized in Tab. 4.7.

TABLE 4.7: Median Granger test results for snow depth retrieval from Sentinel-1 including snow-free conditions

		Spatial resolution [m]		
Relationship		1000	100	30
IMIS to S1	$F°$	3.30	1.13	2.29
	cv	4.03	4.03	3.92
S1 to SLF model	$F°$	6.88	1.24	n.a.
	cv	3.07	3.92	n.a.

The results of the IMIS location SAA indicated an error during data processing, as Fi° approached infinity at 1000 and 100 m GSD. By calculating the median and not the mean correlation, the effect of this value on the result was mitigated. Out of the nine locations, five indicated a positive forecasting relation at 1000 m GSD while four suggested the same at 100 and 30 m GSD (see Fig. 4.12, 4.13, 4.14). The lowest forecasting relation between IMIS measurements and S1 based retrieval at 30 m was found at the location of STN (see Fig. 4.14). This was also the only location consistently indicating no Granger forecasting relation across all examined GSD. The results indicated no forecasting relation between IMIS measurements and the retrieved snow depth from S1. Hypothesis A.0 was retained, stating that SD_{IMIS} does not Granger forecast SD_{S1} and hypothesis A.1 was rejected.

Granger forecasting between S1 and SWE model based snow depth results suggested possible dependency at 1000 m GSD (see Fig. 4.7). Out of the nine locations, eight achieved higher F-scores than their critical values (see Fig. 4.12). However, at 100 m GSD, only three locations indicated the same results (compare Fig. 4.13). At 1000 m GSD, a Granger relation between the S1 based retrieval and the SWE based calculation was suggested, allowing a rejection of the null hypothesis (B.0: SD_{S1} does not Granger forecast SD_{SWE}) and an acceptance of the working hypothesis (B.1: SD_{IMIS} Granger forecasts SD_{S1}). The results at 100 m GSD suggested otherwise. However, as the model was bi-linearly interpolated to 100 m, as an approximation, the validity of the reference data at 1000 m GSD was higher (see chapter 2.4).

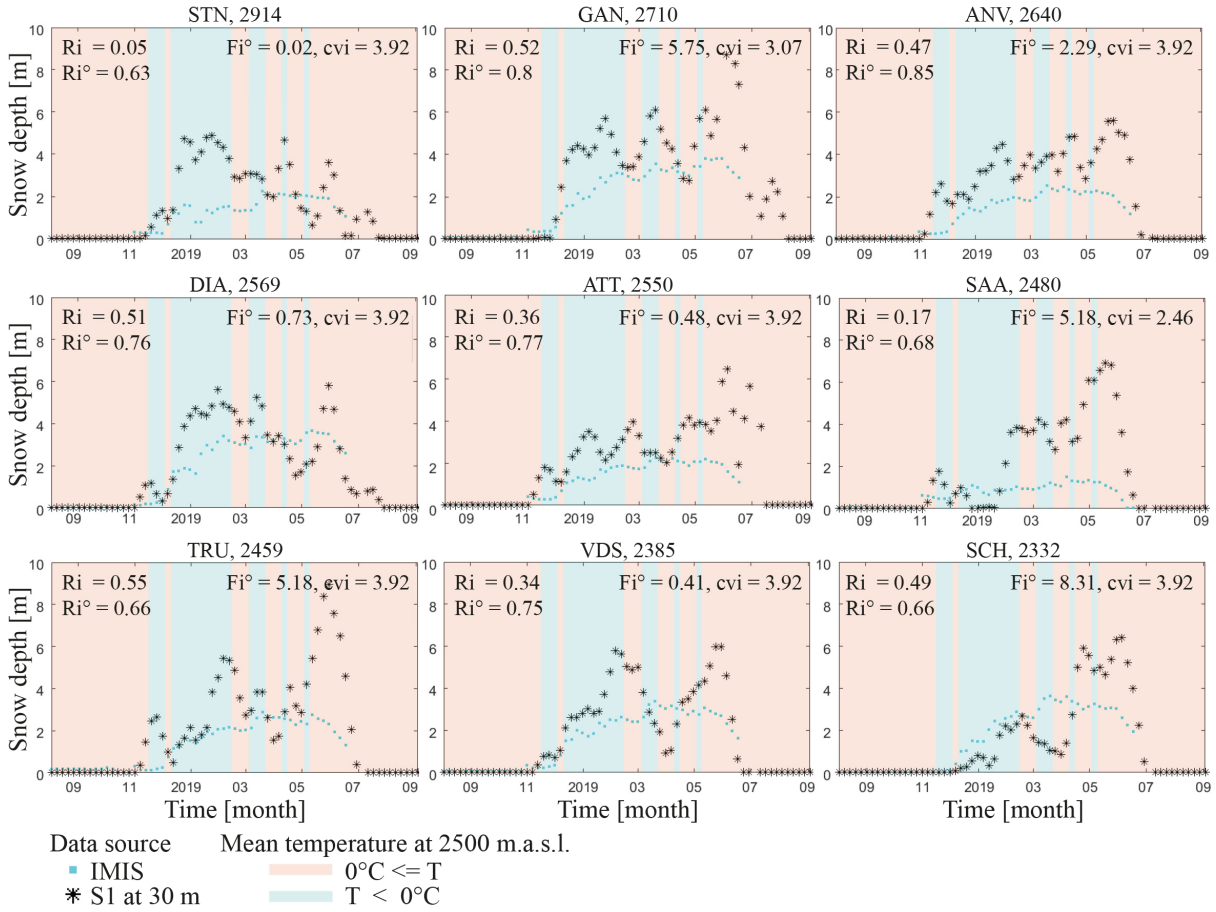

FIGURE 4.14: Snow depth time series retrieved from S1 backscatter at 30 m GSD vs. measurements at IMIS stations (point measurements) in comparison. Each subplot represents an IMIS measurement location; they are sorted by elevation. Top-left boxes depict the achieved Pearson Correlation Coefficient (R_t) between S1 based snow depth retrieval and snow depth measured at local IMIS station (Ri). Top-right boxes display the calculated Granger test results: F-score (F°) and critical value (cv) for corresponding comparisons. In cases where the value $F°$ is higher than the cv a forecasting is suggested. R and F-score values were marked with '°' and were computed across the entire time series including snow free conditions. Those without this marking were calculated solely on data acquired featuring snow cover (masking was based on optical imagery, ExoLabs, 2021)

5 Discussion

Within this chapter, the results described in the previous chapter are described and linked to relevant literature. Challenges as well as opportunities of the performed calculations are presented. A critical view is presented on the executed LRW composite testing (chapter 5.2), before discussing the implementation and validation of wet snow detection and snow depth retrieval (chapter 5.3; 5.4). Finally, challenges of the performed research and possible improvements of the conducted work are introduced (chapter 5.6), before presenting upcoming possibilities in related scientific fields (chapter 5.7).

5.1 Adopted resolution trade-offs

Remote sensing applications are mainly restricted by the adopted trade-offs between resolutions. The focus of this thesis was set on the temporal resolution in between acquisitions and to ensure the possibility of small grid spacings. Time tag of S1 composites could be minimized to 36 h. In-between composite acquisitions six days passed. Thereby, we are very near to approaching the required temporal resolution on a regional scale for snow cover observation as proposed by Malenovský et al. (2012). However, the restricted extent of the test site led to a constrained amount of, especially snow covered, samples available. This presented itself as a drawback during the examination of the influence of land cover and elevation on resulting time series. Due to a lack of available memory and processing power, spatial resolution was only applied to 30 m resolution products, instead of also analyzing the effects on a 10 m grid spacing.

5.2 Local resolution weighting composite time series

Research Question 1:
What opportunities offer multi-track backscatter composites for wet snow mapping in alpine areas?

The potential of multi-track backscatter composite time series (Small et al., 2021) for cryospheric applications was assessed by quantifying their slope dependency of the measured backscatter signal. Suitable potential is met, when East and West slopes feature insignificant differences in backscatter behaviour, which cannot be attributed to external factors.

Hypothesis 1.1:
LRW composites are homogeneous: Variance over time of the S1 LRW image between East and West facing slopes are minimal and found variances can be attributed to acquisition timing.

In case of variances being caused by the timing of acquisition, more melting is expected to be detectable in image parts acquired during the ascending flight track. Descending images are acquired during morning hours (06.34 or 07.34, respectively), whereas ascending images are attained during evening hours (18.20 or 19.20, respectively). The first, therefore, acquires images of a snowpack, which was exposed to less radiation throughout hours before the acquisition than the latter. Ascending images are expected to generally capture snow characteristics, after the snowpack was exposed

to more intense solar radiation and correspondingly warmer temperature conditions. If the timing of the acquisition is influencing the signal such an effect caused by freeze-thaw mechanism should become visible between East and West facing slopes.

Variance between East and West facing slopes have been found to be insignificant. Minimal backscatter was reached by West slopes slightly after the minimal value achieved by East facing regions. Also, the amplitude of decrease in backscatter was found to be of similar characteristics between the two slope directions. Therefore, no heterogeneity was found which could be attributed to the creation of LRW composites. This statement excludes the six prior stated composites, which were discharged and replaced by a mean, due to sensor failure or unavailability.

For this same reason of exposure to solar radiation, stronger signal attenuation in South facing slopes are more frequent, than signal diminution in North facing slopes (Shaw et al., 2020). The lower backscatter values are attributable to a generally more intense and longer exposure to sun-induced radiation (López-Moreno et al., 2013). Such increased exposure has been found to lead to less accumulation and an earlier melt onset in the snowpack (Bender et al., 2020; López-Moreno et al., 2013). This corresponds with the findings within this thesis, where a higher backscatter signal amount was measured in areas oriented towards the North and a below average backscatter was found for South facing slopes. These results further support the validity of multi-track backscatter composites.

Hypothesis 1.2:
VV-polarized backscatter information achieves a more similar trend across slope directions and offers more homogeneous composites than VH-polarized data.

Between VV- and VH-polarization an amplitude difference of around 6 dB was found. By analyzing the temporal change within this ratio (VH/VV), a seasonal trend was detectable: The ratio increased in each aspect - and most so in South facing regions - towards the winter season and declined again during melting. This coincided with the amount of available snow coverage as suggested by Lievens et al. (2019). However, this trend was also visible, when only analyzing snow covered samples.

The mentioned alternating feature, found mainly in VH-polarization, could be linked to a lower noise level and a higher sensibility within that polarization of S1-B, when compared to S1-A (Schmidt et al., 2020; Hajduch et al., 2019). The authors could not find a clear evidence explaining why this behaviour is more evident during 2018 than 2019 or 2020. The summer of 2018 was comparatively hot and dry. This possibly led to a more pronounced signal. The diminution of this behaviour could also have been addressed in a re-calibration between 2018 and 2019. However, it did not influence the results in this thesis, because its effect upon snow covered samples was minimal.

Overall, the HH-polarized data suggested more homogeneous LRW composites, due to sensor differences between S-1A/-1B in VH-polarization. Also, the difference between North and South facing slopes were found larger in VH-polarization, when compared to VV. However, for cryospheric applications the difference in homogeneity was minimal and both polarization states were found applicable.

Hypothesis 1.3:
Elevation and land coverage (especially vegetation) influence the resulting time series and the reliability of this slope dependency approach for LRW homogeneity testing.

Throughout all time series with a statistical relevancy of snow coverage the characteristic loss in backscatter, which indicates snow melt (Saberi et al., 2020; Marin et al., 2020; Hallikainen, 1992), was detected. The timing and magnitude of this backscatter was found to be dependent upon

elevation, land cover and slope orientation (Jäger, 2016; Rohner, 2014). However, a clear distinction between the effect of land cover and elevation was not within the scope of this thesis.

The results supported the findings of previous researchers wherein areas featuring high vegetation activity provide unfeasible backscatter signals for snow applications (Jäger, 2016; Rohner, 2014). North facing slopes have been found to provide more favourable conditions for vegetation to grow (Bennie et al., 2008). This suggested corresponding time series to be more prone to volume scattering attributable to vegetation. Results were calculated by aggregating the land cover classes to corresponding spatial resolutions, the pixel purity was not considered. Mixed pixel effects (see Lillesand et al. (2015)), bias the resulting time series between corresponding land cover classes.

5.3 Comparison of reference image approaches

Research Question 2:

Which approach for the generation of a dry winter reference image achieves highest accuracies in wet snow detection when compared to model based LWC maps?

Hypothesis 2:

Creating a median composite image over the winter months relevantly improves wet snow mapping compared to a single composite or a median of three based approach, when compared to liquid water content maps.

Change detection using reference image approaches is used in diverse land cover observation applications of a hydrological nature. It is used to assess the characteristics of snowpacks (e.g. Schellenberger et al. (2012) and Nagler et al. (2000)), to observe flooding events (Clement et al., 2018) or to estimate the degree of soil moisture (Pulliainen et al., 1996). In this thesis, the validity of a reference image was assessed by comparing the resulting wet snow maps to the modelled liquid water content (LWC) of snow maps. Performing a validation on the application requires a discussion of the performed approaches used during the application.

The applied wet snow detection algorithm was first suggested by Rott et al. (1995) and has since been applied in multiple studies (see review by Tsai et al. (2019)). Its simplicity and broad applicability allows the algorithm to remain state-of-the-art wet snow detection (Tsai et al., 2019), with an adjustment of the threshold to -2 dB (Nagler et al., 2016).

Reference images can be created by using dry winter or snow-free summer backscatter information (Nagler et al., 2000). In multiple applications of this method, soil moisture was found to degrade the accuracy of snow mapping (e.g. Schellenberger et al., 2012). To minimize this effect, Pettinato et al. (2014) suggested the usage of dry winter reference images to be preferable over summer scenes. The results by Jäger (2016) indicated best performance by a so-called improved winter reference scene. Hereby, a dry winter composite was supplemented by using summer backscatter data, where wet snow contamination was present. Rohner (2014) found the temporal offset of the reference image in comparison to the observed scene to increase the inaccuracies. A widely discussed drawback of the approach by Rott et al. (1995) is its insensitivity towards dry snow detection (Koskinen et al., 1997). This led to non-circumventable errors of omission in diverse studies, where wet snow detection was validated using optical imagery (Jäger, 2016).

In this thesis, we combined the findings of these studies by creating a winter season reference image. By allowing to condense backscatter information over three months over a test site, which features relatively small climatic differences (in contrast to the study of e.g. Jäger (2016), whose test site covered the entire alpine area), all pixel-samples were covered at least once during dry or no snow cover conditions. By using the winter season approach, void gaps could be eliminated on account of

the sufficient data supplementation. By including the extent of snow cover by optical imagery into the snow detection algorithm, a differentiation between dry snow and no snow became possible. The produced image was set in comparison to images in an already applied single composite reference image approach (e.g. Small et al. (2021) and Rüetschi et al. (2019)) as well as a median of three.

The validation was performed by comparing wet snow maps to modelled LWC maps (similar to the validation conducted by Marin et al. (2020)). This allowed to minimize the effect of errors due to the lossless transmission of C-band microwave frequency through dry snow. When digitizing LWC into binary maps, a threshold was determined by using an iterative process. Thereby, the most favourable trade-off between errors of commission and errors of omission was striven for, resulting in best performance, also indicated by the highest overall accuracy (OA). However, while the threshold of -2 dB for wet snow mapping from SAR is already well established (Nagler et al., 2018) and its robustness proved to be reliable (Tsai et al., 2019), the definition of the threshold for the liquid water amount required for the possible detection by C-band SAR, had to the knowledge of the authors not yet been established.

The calculated statistical values differ in their significance concerning the here performed study of wet snow analysis. The validation using modelled LWC data allowed to have a more meaningful OA than previous studies (e.g. Jäger (2016)), as dry snow areas were also excluded in the reference data. User's and producer's accuracy and corresponding error of omission and commission were of equal relevance and an analysis of the combination suggested an applicable understanding of the outcome. However, the κ was of relatively low relevance, for it is strongly dependent on the count of detections in either data set (LWC or S1).

The meaningfulness of the statistical measures is dependent on the amount of samples available. This lead to high fluctuations in errors of omission and commission during summer, when snow cover was limited - especially in the 1000 m resolution. A comparison of the behaviour of statistical measures over time allowed to examine the corresponding significance. Therefore, inter-comparison across various statistical measures was required to accurately quantify the performance.

κ indicates the performance of the wet snow classifier based on S1 in comparison to a random wet snow classifier. The resulting value is therewith highly dependent on the class of wet snow to be present in the reference data, otherwise κ is automatically zero, as no wet snow was classified correctly in either random classifier or S1 based classification. Between September and February, however, very little to no wet snow was present in LWC due to the model reset (see chapter 2.4). This resulted in a mean and median κ to be low.

Errors of omission were highly seasonal. This was traced back to the reset of the LWC model each September. With no wet snow in the reference validation, errors of exclusion consequently remained zero. The majority of errors of exclusion amounted in spring and encompassed regions of correctly classified wet snow. This effect indicated a possible enhancement of the results by further adjusting the threshold of LWC. On the other hand, it stands in accordance to the findings of Nagler et al. (2000) indicating that C-band SAR tends to underestimate the presence of wet snow, where snow coverage is discontinuous.

Errors of commission were mainly found in altitudes higher than the correctly classified wet snow. This indicated S1 to be able to detect wet snow already prior to its appearance based on the LWC model. This might be another effect attributable to the validation data set. The LWC model worked on run-off data. It lagged initial snow melt due to the percolation throughout the snowpack (Winstral et al., 2019). This melting in the top layer of the snowpack, however, interacted with S1 information, thereby reacting faster. With the proceeding melting season, the error of commission wandered into higher elevation zones, where S1 again enabled the detection of the snow melt earlier than the model based mask indicated.

The dispersion pattern of errors in relation to their aspect indicated no clear dependency. The errors of omission assembled the general aspect distribution of available pixels. Also, the distribution of errors of commission suggested no clear cardinal direction to be of relevance. The strong differences in amplitudes suggested the diverse slopes' time series to be more likely prone to errors of commission than others.

Discrepancies between VV- and VH-polarized information were mainly found during summer. The increase in the error of omission in VV-polarization was found to be restricted to the land cover class of bare soil. Further analysis could include the results of cross-correlation differences.

The comparison of reference image approaches over time and space indicated results standing in agreement to literature (e.g. Nagler et al. (2016)). For selected applications featuring a restricted time, a single composite reference image might be sufficient and be preferred in certain studies due to its simplicity, speed and minimal processing costs. However, as already found by other authors, the approach of using multiple images (Pettinato et al., 2014) or composites (Jäger, 2016) for the reference image generation achieved higher accuracies than a single composite reference image.

The changes in statistical measures over time differed negligibly between the median of three acquisitions featuring the coldest conditions and a median over three winter months. Both approaches were able to cover all image samples at least once during dry or no-snow conditions and so remove all gaps caused by wet snow contamination within the reference image. However, a slight improvement was achieved by using more than three composites. Moreover, a decrease in accuracy was found when increasing the time offset between acquisition and reference image by using the single composite reference image approach. The winter season approach indicated the strongest robustness also towards this effect.

5.4 Snow depth retrieval

Research Question 3:
Are multi-track backscatter composites sensitive to snow depth when applying the method of Lievens et al. (2019)?

Hypothesis 3.1:
By applying the method of Lievens et al. (2019) a correlation between snow depth and the VH/VV-backscatter difference is achieved.

Diverse studies suggested inconclusive results, when examining a possible link between snow depth and radar measurements. These studies mainly focused on single polarization states (Rutter et al., 2019; Shi et al., 2000) or radiometry (Tedesco et al., 2010; Grody, 2008) at X- and Ku-band. Also, approaches for snow depth extraction were attempted based on interferometric techniques (Varade et al., 2020; D. Li et al., 2017). Lievens et al. (2019) were the first to assess a correlation between the polarization ratio at C-band SAR and snow depth. While the search for physical explanations to the found correlation are still ongoing, the retrieval is based on the idea of building up a snowpack in form of a recursive function over time, so performing multi-temporal change detection.

After masking out snow free conditions, correlation was found to be moderate (after McHugh (2012)). The best performance of snow depth retrieval from S1 was found to be at converging spatial resolutions. However, the statistical results did not indicate applicable stability of the performed retrieval. This is in accordance with current radiative transfer models and the understanding of snow backscatter behaviour (D. Li et al., 2017; Rees, 2006), albeit in contrast to the findings of Lievens et al. (2019). In the following, multiple aspects are discussed, which could have led to this difference in the statistical outcome.

During processing, diverse aspects were altered to the approach suggested by Lievens et al. (2019). The main difference was the used spatial resolution. By exchanging σ_T° to γ_c° convention, a higher temporal and spatial resolution was achieved.

Lievens et al. (2019) suggested an exclusion of wet snow pixels, as their impact on retrieval was not yet fully understood. Lievens et al. (2021) argue that wet snow contamination results in an under-estimation of snow depth due to the absorbing characteristics of water. However, by masking out samples possibly influenced by wet snow, an insignificant amount of samples remained, when analyzing the complete melting cycle. As a result, we refrained to mask out wet snow, so accepting a possible underestimation of the snow depth.

De facto, the expected decrease in snow depth during above freezing point temperature conditions was found across all used GSDs. The effect of such melting events biased snow depth retrieval at 1000 m scale to an extent, which emphasized to mask out wet snow in future analyses of snow depth retrieval (see Fig. 4.12, Lievens et al., 2019). However, at 30 m GSD a general overestimation during temperatures below freezing point and a higher accordance between IMIS station measurements and S1 retrieval during conditions of wet snow was found (see Fig. 4.14). Across all spatial resolutions, a strong and sudden increase in snow depth after the last event of cold winter conditions was detected, which was not found in either reference data set. This dependency on the warming temperatures suggested the retrieval being biased by melting effects.

The difference in under- and over-estimation at diverse spatial resolutions between IMIS snow depth measurements and S1 retrieved information could also be attributable to point measurements not automatically replicating the mean snow depth value within the corresponding grid spacing of S1 (Lievens et al., 2021; Egli et al., 2010). Especially so, as the IMIS measurements are characteristically performed on a wind-protected plain (SLF, 2021b), whereas larger footprints by satellite measurements likely include more mountainous terrain.

The locations of IMIS stations are displayed in Fig. 5.1. The results of two stations indicated erraneous retrievals: GAN and DIA. While contemporaneous sudden changes in snow depth between IMIS and S1 could be found, the correlation coefficient indicates unfeasible results at 1000 m during the first snow season. Backscatter at these two stations was most likely biased due to glacial run off, as they are situated just below the Glaciers *Milibachgletscher* and *Glacier de Tsanfleuron*. Additionally, the linkage to temperatures rising above zero indicated melting and/or run off to be the cause. On higher resolutions, such as 100 and 30 m, this effect could be better accounted for. The station STN is also situated near a glacier, however, the glacier is smaller in size and its run off system already developed. This relation may have also influenced the results at the STN station, which was found to resulte in the worst statistical measures.

Further inquiries should include the location of grid spacing. Especially, the location of the GAN station could be prone to errors due to the pixel size and location definition: the mountain ridge is in near vicinity of the station and the North side of the mountain is characterized by steep terrain (see Fig. 5.1). Such terrain effects possibly influenced the backscatter signal and biased the retrieval.

The snow detection algorithm applied is based on a recursive snow index. When calculating this snow index into snow depth, vegetation density information was used in combination of parameters a and b. Throughout this thesis, these parameters were assumed constant as described in Lievens et al. (2019). Lievens et al. (2021) proposed an optimization of the algorithm also by adjusting the parameter b, which was not implemented during this project. However, as all of the selected locations were situated above the tree line and hence in sparsely vegetated zones, parameter b affects the achieved statistics barely (compare Fig. 5.1).

Between S1 and SLF model based snow depth retrieval, a moderate correlation was detected. Hereby, the S1 snow depth maximum is (with the exception of the GAN and DIA location) al-

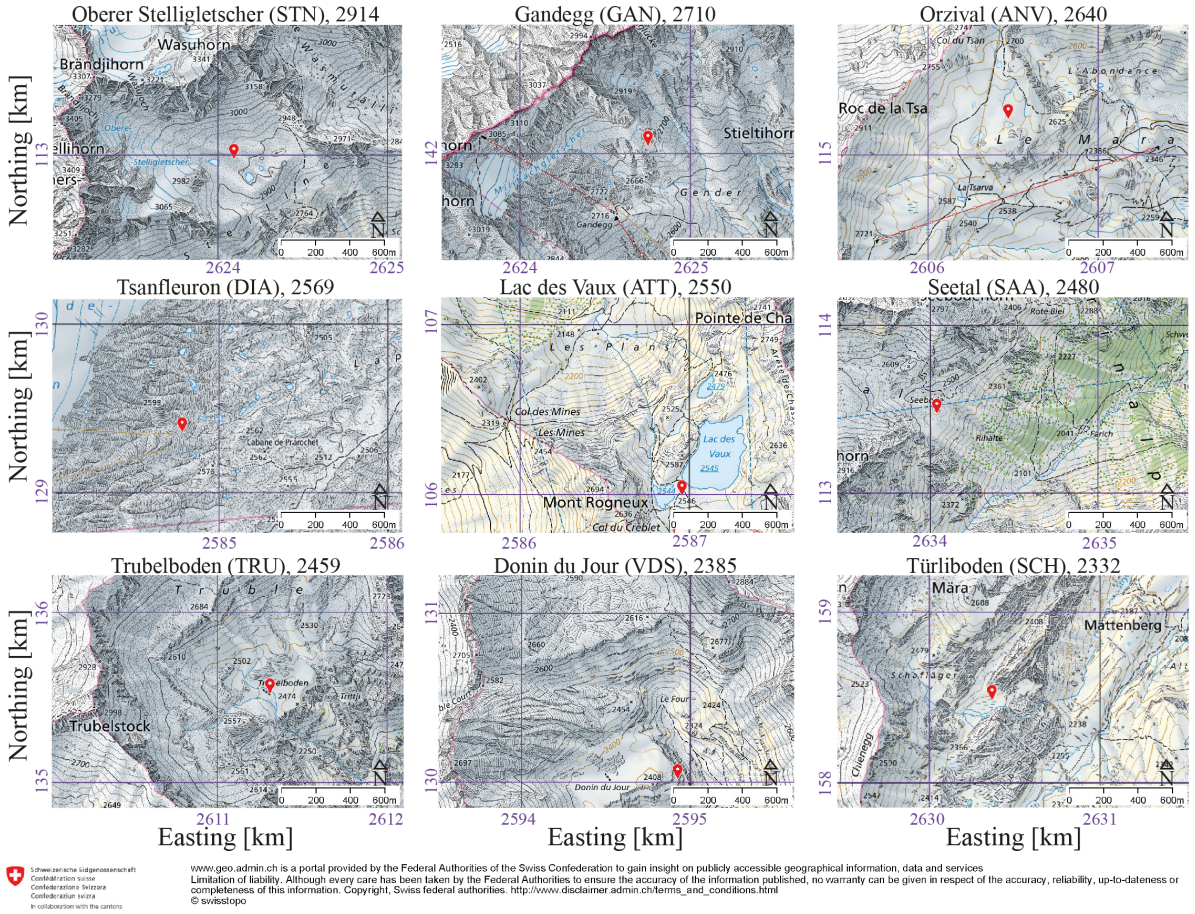

FIGURE 5.1: Locations of IMIS snow stations (red marker) superimposed on the map of Switzerland by the Swiss Confederation.

ways reached earlier using S1 detection than the SWE model. This was to be expected, as the SLF model is based on run off data (Winstral et al., 2019). As discussed earlier, this leads to a delay in snow depth retrieval, as the melting must first percolate through the snowpack before it is incorporated in the model.

Correlation was assessed once across the full time series and once by only considering actual snow cover information. In accordance to the results by Lievens et al. (2019), the achieved correlation statistics decreased when excluding snow free composites. However, the degree of the decrease in amplitude diverged. While the temporal correlation results between point measurements and S1 retrievals presented in Lievens et al. (2019) decreased from a mean of 0.77 to 0.65, the mean values in this thesis decreased from 0.63 to 0.32 at 1000 m GSD. This amplitude difference may be related to the selected broadness of the test site or to the approach of masking out snow free areas. Whereas Lievens et al. (2019) discharged all information when snow depth values equalled zero, the performed masking in this theses was based on snow coverage from optical imagery. We will base further discussion on the correlations measured after masking out no snow conditions as this indicated a better measure of the performance of snow depth retrieval from S1.

Generally, higher correlation values were achieved when spatial resolutions were converging and thereby reducing the gulf between the resolutions. This stands in contrast to the results of Lievens et al. (2021), where increasing resolution (1000 to 300 to 100 m) resulted in a decrease in the achieved correlation coefficient. Lievens et al. (2021) offer three explanations for their decline in accuracy, namely i) increasing speckle noise, ii) geolocation and geometric distortions and iii) local

heterogeneity and snow variables. By using γ_c° convention two of these aspects were better accounted for: speckle noise by using multi-track images (Rüetschi et al., 2019) as well as geometric distortions by using local resolution weighting (Small, 2012).

Hence, while no stable correlation was detected based on the performed approach, multi-track backscatter composites did allow to increase accuracy measures with increasing spatial resolution, whereas the usage of single-track images in σ° conventions resulted in a decrease in accuracy (Lievens et al., 2021).

> Hypothesis 3.2:
> By applying the Granger test a forecasting chain between IMIS snow depth measurements, snow depth retrieved from S1 and snow depth approximated from a snow water equivalent model is found.

A Granger forecasting test between measured IMIS snow depth and snow depth retrieved from S1 was run. However, the test indicated the forecasting relation to be minimal below a maximum time delay of 20 days. The achieved scores varied highly across locations and were heavily dependent on the choice of the maximum allowed lag. The main merit of the Granger approach is to account for lagged (delayed) impacts (Feldman et al., 2020). The impact of in-situ measurements of snow depth on S1, however, is comparatively rapid and could, thereby, make the usage of the Granger test invalid. Based on the achieved results, the null-hypothesis was kept, which indicated no Granger forecasting S1 snow depth from IMIS measurements. However, the significance of this test for this application was minimal when compared to the correlation coefficient (R_t).

By using the Granger test to find a forecasting relation between S1 snow depth and snow depth from the SLF model, which includes percolation effects, the expected offset (Winstral et al., 2019; Jonas et al., 2009) could be better accounted for. Maximum time lag was set to 30 days allowing for the one month offset due to percolation though the snowpack, and which was set in correspondence with T. Jonas (contact person at SLF concerning LWC model). A Granger forecasting relation was thereby found between snow depth from S1 to model based snow depth extraction, allowing to reject the null-hypothesis and accept the working hypothesis.

The results of the conducted Granger forecasting tests indicated a possible feasibility of snow depth retrieval from S1, as they were able to forecast snow depth retrieved from SWE data. However, this forecasting relation includes the complete time series. For the remaining data, after having masked out information during no snow coverage, it did not suffice to allow for the required time lag and still solving the equation. The weight of this forecasting relation statistics correspondingly undercuts the weight of the correlation analysis.

5.5 Additional factors

Cryospheric ecosystems interact in a complex manner with microwave frequencies and diverse multi-scattering effects occur due to the present mountainous terrain. Synthesizing the usage of the γ° convention with the creation of LRW composites allowed to disentangle some scattering mechanisms. However, diverse other factors would be of interest to further dissolve the complex interaction chains. For example the magnitude of the soil interaction on wet snow detection at 30 m spatial resolution or the influence of snowpack characteristics such as snow density and mixed pixel effects on wet snow detection and snow depth retrieval. Moreover, causation between precipitation events and snow depth retrieved from S1 could be examined. Following up on and exploiting the effect of such factors might be a focus for further research.

5.6 Limitations and potentials for further research

Diverse aspects of this thesis might be set as foci of further research projects. A follow-up project might 1) further examine the effect of the difference in noise levels between S1-A and -B in VH-polarization and determine factors influencing the magnitude of this feature. Also, in such a framework, the challenges and opportunities of cross-ratio (VH/VV) LRW composites for cryospheric applications could be addressed. Moreover, 2) an assessment of the signal to noise ratio at diverse spatial resolutions could be attempted. Thereby, the study could also exploit the possibility to generate 10 m resolved LRW composites from S1. Validation of e.g. snow maps or snow depth retrieval could then be performed using corresponding point measurements. Additionally, a follow-up project might include 3) performance assessment of wet snow mapping based on the VH/VV-polarization difference and a comparison of the best performing γ_c° reference image generation approach found by Jäger (2016) to the here presented winter season reference composite. Furthermore, 4) an optimization of the performed validation process of snow depth retrieval should be attempted by making use of a prolongued IMIS data set. Here, the new snow index algorithm presented in Lievens et al. (2021) should be implemented. Thereby, its feasibility over forested areas should be further examined and the effect of wet snow investigated. Additionally, 5) instead of performing validation on modelled SWE data solely at certain locations, a comprehensive map is suggested, which features spatio-temporal information on the performance of S1 based snow depth retrieval in comparison to model based data.

5.7 Outlook

Already, researchers are creating a tower based S1 C-band sensor replica to exploit further possibilities of data assimilation from S1 and to push forward the knowledge and understanding of the opportunities of C-band SAR in connection to snow observation from space (Lievens et al., 2020). These measurements will allow to conduct extensive studies to improve calibration procedures and to enable optimization of algorithm parameters (already partly addressed in Lievens et al. (2021), which is currently in review).

Future research could examine the feasibility of a synthesis between C-band and shorter waved X-band SAR LRW composites to account for diverse snowpack characteristics including snow depth (Shi et al., 2000). By exploiting such a synergy, accurate and gap free weekly images over snowpacks could become possible in the near future. Such enhancements would enable upcoming software developers to create high-resolution and user-friendly maps, which allow practical applications and offer a new basis for further enhancements in avalanche forecasting and warning systems.

The "new space" era offers further possibilities to extend the observation of cryospheric ecosystems (Small et al., 2021). Even more so by making use of the upcoming wide area analysis-ready radar backscatter composites, which allow to combine even larger constellations of satellites than hitherto possible (Small et al., 2021). As a start, a follow-up scientific project might make use of the recently launched RADARSAT constellation mission (launched on 12.05.2019, Government of Canada, 2020). By combining C-band information from the RADARSAT mission and measurements from the ongoing tower-based research in the Rocky Mountains (Lievens et al., 2020), extensive dry snow research will become possible.

6 Conclusions

In this thesis we examined possible challenges and opportunities offered by multi-track backscatter composites for cryospheric applications. First, we assessed the homogeneity of LRW composites and investigated their degree of usability for wet snow mapping in alpine areas. Secondly, we identified a stable approach for producing a dry snow reference image and mapped wet snow occurrences. Thirdly, we investigated the feasibility of snow depth retrieval from γ° S1-backscatter composites.

The achieved results indicated LRW composites to be homogeneous. The slope dependent changes in backscatter were found to be due to external factors, rather than to the temporal offset of the image acquisition used for the generation of the composite. External factors shown to influence the measured backscatter amplitude were polarization state, land cover type and elevation as well as slope exposition in relation to solar radiation.

We evolved a dry snow reference image approach by introducing a method to create a dry winter season reference image. By stacking multiple composites together speckle noise was minimized and effects caused by the temporal offset were suppressed. By performing the validation using LWC maps, a meaningful comparison between wet snow maps was achieved. A comparison of the statistical measures supported the need for such a method of creating a median across multiple composites, especially for multi-season analyses.

A possible feasibility of Sentinel-1 images using the γ_c° convention for snow depth retrieval was found inconclusive. By validating the retrieved results with both IMIS snow depth measurements and SWE maps, we minimized the effect of the gulf between the multiple resolutions. By not only investigating the correlation, but also examining the degree of Granger forecasting the relationships, we were able to account for the model based lag in SWE data. We found a moderate to good correlation between S1 and IMIS as well as S1 and SWE. The latter also indicated a forecasting relation and so suggested a possible causation. However, this result must be treated with caution as the assessment of the forecasting relation also included snow free conditions. The achieved results of both statistical measures improved with converging spatial resolutions.

The usage of multi-track backscatter composites enabled to evolve the extraction of wet snow locations and snow depth information from Sentinel-1 backscatter. With their usage, we achieved shorter time tags, smaller time gaps in-between acquisitions and higher spatial resolution imaging and corresponding retrievals. Hence, multi-track backscatter composites offer a highly promising approach to cost-effectively improve data assimilation for cryospheric applications. Further studies on the topic of snow depth retrieval and especially aspirations after a physical explanation of this linkage between SAR backscatter ratio and snow depth are encouraged.

References

Arslan, A. N. (2006). *Microwave models of snow characteristics Remote Sensing* (Doctoral dissertation, Helsinki University of Technology).

Baghdadi, N., Gauthier, Y., & Bernier, M. (1997). Capability of multitemporal ERS-1 data for wet-snow mapping. *Remote Sensing of Environment*, *60*(2), 174–186. doi:10.1016/S0034-4257(96)00180-0

Bender, E., Lehning, M., & Fiddes, J. (2020). Changes in Climatology, Snow Cover, and Ground Temperatures at High Alpine Locations. *Frontiers in Earth Science*, *8*(May), 1–17. doi:10.3389/feart.2020.00100

Bennie, J., Huntley, B., Wiltshire, A., Hill, M. O., & Baxter, R. (2008). Slope, aspect and climate: Spatially explicit and implicit models of topographic microclimate in chalk grassland. *Ecological Modelling*, *216*(1), 47–59. doi:10.1016/j.ecolmodel.2008.04.010

Bernier, M., & Fortin, J. P. (1992). Potential of ERS-1 data for snow cover monitoring. In *International geoscience and remote sensing symposium (igarss)*. doi:10.1109/IGARSS.1992.578800

Burgin, M., Tabatabaeenejad, A., & Moghaddam, M. (2012). A generalized radar scattering model for multispecies forests with multilayer subsurface soil. In *International geoscience and remote sensing symposium (igarss)* (July, pp. 5817–5819). doi:10.1109/IGARSS.2012.6352287

Chandler, n. (2021). Granger Cause Test: Matlab file exchange. Retrieved from https://www.mathworks.com/matlabcentral/fileexchange/25467-granger-causality-test

Clement, M. A., Kilsby, C. G., & Moore, P. (2018). Multi-temporal synthetic aperture radar flood mapping using change detection. *Journal of Flood Risk Management*, *11*(2), 152–168. doi:10.1111/jfr3.12303

Daly, C., Conklin, D. R., & Unsworth, M. H. (2009). Local atmospheric decoupling in complex topography alters climate change impacts. *International Journal of Climatology*. doi:10.1002/joc.2007

Derrick, T. R., Bates, B. T., & Dufek, J. S. (1993). Evaluation of time-series data sets using the Pearson product-moment correlation coefficient. *Official Journal of the American College of Sports Medicine*. doi:n.a.

Dietz, A. J., Kuenzer, C., Gessner, U., & Dech, S. (2012). Remote sensing of snow - a review of available methods. *International Journal of Remote Sensing*, *33*(13), 4094–4134. doi:10.1080/01431161.2011.640964

Egli, L., Jonas, T., & Bettems, J. M. (2010). A virtual network for estimating daily new snow water equivalent and snow depth in the Swiss Alps. *Annals of Glaciology*, *51*(54), 32–38. doi:10.3189/172756410791386427

ESA. (2021). Sentinel Missions. Date accessed: 2021-03-13. Retrieved from https://sentinel.esa.int/web/sentinel/missions

Essery, R., Morin, S., Lejeune, Y., & B Ménard, C. (2013). A comparison of 1701 snow models using observations from an alpine site. *Advances in Water Resources*, *55*, 131–148. doi:10.1016/j.advwatres.2012.07.013

European Environment Agency. (2017). High Resolution Layer Forest: Product Specifications Document. *Copernicus Land Monitoring Service*, 38. Retrieved from https://land.copernicus.eu/user-corner/technical-library/hrl-forest

European Environment Agency. (2018a). CORINE Land Cover. Date accessed: 2021-03-13. Retrieved from https://land.copernicus.eu/pan-european/corine-land-cover

European Environment Agency. (2018b). Tree Cover Density 2018. Date accessed: 2021-03-13. Retrieved from https://land.copernicus.eu/pan-european/high-resolution-layers/forests/tree-cover-density/status-maps/tree-cover-density-2018?tab=metadata

ExoLabs. (2021). Snow Cover. Date accessed: 2021-03-13. Retrieved from https://exolabs-ch.gitbook.io/cosmos/snow-cover

Feldman, A. F., Short Gianotti, D. J., Trigo, I. F., Salvucci, G. D., & Entekhabi, D. (2020). Land-Atmosphere Drivers of Landscape-Scale Plant Water Content Loss. *Geophysical Research Letters*, *47*(22). doi:10.1029/2020GL090331

Fortin, J. P., & Bernier, M. (1995). Results from model comparisons with ERS-1 and field data for snow water equivalent estimation. In *International geoscience and remote sensing symposium (igarss)* (Vol. 3, pp. 2176–2178). doi:10.1109/igarss.1995.524140

Gao, L., Bernhardt, M., & Schulz, K. (2012). Elevation correction of ERA-Interim temperature data in complex terrain. *Hydrology and Earth System Sciences*, *16*(12), 4661–4673. doi:10.5194/hess-16-4661-2012

GLAMOS. (2010). Swiss glaciers. Date accessed: 2021-03-13. Retrieved from https://www.glamos.ch/en/#/C14%2F10

Government of Canada. (2020). RADARSAT Constellation Mission (RCM). Date accessed: 2021-03-13. Retrieved from https://www.asc-csa.gc.ca/eng/satellites/radarsat/default.asp

Granger, C. W. J. (1969). Investigating Causal Relations by Econometric Models and Cross-spectral Methods. *Econometrica*, *37*(3), 424. doi:10.2307/1912791

Grody, N. (2008). Relationship between snow parameters and microwave satellite measurements: Theory compared with advanced microwave sounding unit observations from 23 to 150 GHz. *Journal of Geophysical Research Atmospheres*, *113*(22), 1–17. doi:10.1029/2007JD009685

Guneriussen, T. (1997). Backscattering properties of a wet snow cover derived from DEM corrected ERS-1 SAR data. *International Journal of Remote Sensing*, *18*(2), 375–392. doi:10.1080/014311697219123

Hajduch, G., & Miranda, N. (2019). S-1A & S-1B Annual Performance Report for 2018. *Mission Report*, *DI-MPC-APR*(1.2). Retrieved from https://sentinel.esa.int/documents/247904/0/Sentinel-1-Annual-Performance-Report-2018.pdf/

Hallikainen, M. (1992). Review of the microwave dielectric and extinction properties of sea ice and snow. In *International geoscience and remote sensing symposium (igarss)* (Vol. 2, *December*, pp. 961–965). doi:10.1109/IGARSS.1992.578309

Howell, S. E., Small, D., Rohner, C., Mahmud, M. S., Yackel, J. J., & Brady, M. (2019). Estimating melt onset over Arctic sea ice from time series multi-sensor Sentinel-1 and RADARSAT-2 backscatter. *Remote Sensing of Environment*, *229*, 48–59. doi:10.1016/j.rse.2019.04.031

Ihlen, V., & Zanter, K. (2019a). Landsat 7 (L7) Data Users Handbook. *USGS Landsat User Services*, *7, Version*(November), 151.

Ihlen, V., & Zanter, K. (2019b). Landsat 8 (L8) Data Users Handbook. *USGS Landsat User Services*, *8, Version*(June), 97.

Jäger, D. (2016). Wide-area wet snow mapping of the Alps based on Sentinel-1 multi-track radar backscatter composites. University of Zurich.

Jonas, T., Marty, C., & Magnusson, J. (2009). Estimating the snow water equivalent from snow depth measurements in the Swiss Alps. *Journal of Hydrology*, *378*(1-2), 161–167. doi:10.1016/j.jhydrol.2009.09.021

Koch, F., Henkel, P., Appel, F., Schmid, L., Bach, H., Lamm, M., ... Mauser, W. (2019). Retrieval of Snow Water Equivalent, Liquid Water Content, and Snow Height of Dry and Wet Snow by Combining GPS Signal Attenuation and Time Delay. *Water Resources Research*, *55*(5), 4465–4487. doi:10.1029/2018WR024431

Koskinen, J. T., Pulliainen, J. T., & Hallikainen, M. T. (1997). The use of ERS-1 sar data in snow melt monitoring. *IEEE Transactions on Geoscience and Remote Sensing*, *35*(3), 601–610. doi:10.1109/36.581975

Largeron, C., Dumont, M., Morin, S., Boone, A., Lafaysse, M., Metref, S., ... Margulis, S. A. (2020). Toward Snow Cover Estimation in Mountainous Areas Using Modern Data Assimilation Methods: A Review. *Frontiers in Earth Science*, *8*(September). doi:10.3389/feart.2020.00325

Lehning, M., Bartelt, P., Brown, B., Fierz, C., & Satyawali, P. (2002). A physical SNOWPACK model for the Swiss avalanche warning Part II. Snow microstructure. *Cold Regions Science and Technology*, *35*(3), 147–167. doi:n.a.

Lehning, M., Bartelt, P., Brown, B., Russi, T., Stöckli, U., & Zimmerli, M. (1999). SNOWPACK model calculations for avalanche warning based upon a new network of weather and snow stations. *Cold Regions Science and Technology*, *30*(1-3), 145–157. doi:10.1016/S0165-232X(99)00022-1

Li, D., Durand, M., & Margulis, S. A. (2017). Estimating snow water equivalent in a Sierra Nevada watershed via spaceborne radiance data assimilation. *Water Resources Research RESEARCH*, *53*, 647–671. doi:10.1002/2016WR018878

Li, H., Wang, Z., He, G., & Man, W. (2017). Estimating snow depth and snow water equivalence using repeat-pass interferometric SAR in the northern piedmont region of the Tianshan Mountains. *Journal of Sensors*, *2017*(April). doi:10.1155/2017/8739598

Lievens, H., Brangers, I., Marshall, H.-p., Jonas, T., Olefs, M., & De Lannoy, G. J. (2021). Sentinel-1 snow depth retrieval at sub-kilometer resolution over the European Alps. *The Cryosphere*, *Preprint*(12 March). doi:10.5194/tc-2021-74

Lievens, H., Demuzere, M., Marshall, H.-p., Reichle, R. H., Brangers, I., Rosnay, P. D., ... De Lannoy, G. J. (2019). Snow depth variability in the Northern Hemisphere mountains observed from space. *Nature Communications*, *10*(4629), 1–33. doi:10.1038/s41467-019-12566-y

Lievens, H., Demuzere, M., Marshall, H.-p., Reichle, R. H., Brangers, I., Rosnay, P. D., ... De Lannoy, G. J. (2020). Snow depth observations from Sentinel-1 over the Northern Hemisphere mountain ranges The importance of snow.

Lillesand, T. M., Kiefer, R. W., & Chipman, J. W. (2015). *Remote sensing and image interpretation* (seventh). USA: Courier Westford.

López-Moreno, J. I., Pomeroy, J. W., Revuelto, J., & Vicente-Serrano, S. M. (2013). Response of snow processes to climate change: Spatial variability in a small basin in the Spanish Pyrenees. *Hydrological Processes*, *27*(18), 2637–2650. doi:10.1002/hyp.9408

Lyu, H., Mccoll, K. A., Li, X., Derksen, C., Berg, A., Black, T. A., ... Entekhabi, D. (2017). Remote Sensing of Environment Validation of the SMAP freeze / thaw product using categorical triple collocation. *Remote Sensing of Environment*, *205*(2018), 329–337. doi:10.1016/j.rse.2017.12.007

Macelloni, G., Brogioni, M., Montomoli, F., & Fontanelli, G. (2012). Effect of forests on the retrieval of snow parameters from backscatter measurements. *European Journal of Remote Sensing*, *45*(1), 121–132. doi:10.5721/EuJRS20124512

Malenovský, Z., Rott, H., Cihlar, J., Schaepman, M. E., García-Santos, G., Fernandes, R., & Berger, M. (2012). Sentinels for science: Potential of Sentinel-1, -2, and -3 missions for scientific observations of ocean, cryosphere, and land. *Remote Sensing of Environment*, *120*, 91–101. doi:10.1016/j.rse.2011.09.026

MapTilerTeam. (2019). EPSG:3035. Date accessed: 2021-03-13. Retrieved from http://epsg.io/3035

Marin, C., Bertoldi, G., Premier, V., Callegari, M., Brida, C., Hürkamp, K., ... Notarnicola, C. (2020). Use of Sentinel-1 radar observations to evaluate snowmelt dynamics in alpine regions. *Cryosphere*, *14*(3), 935–956. doi:10.5194/tc-14-935-2020

MathWorks. (2021). polarhistogram. Date accessed: 2021-03-13. Retrieved from https://ch.mathworks.com/help/matlab/ref/polarhistogram.html#d123e1024746

McHugh, M. L. (2012). Interrater reliability: the kappa statistic. *Biochemia Medica*, *22*(3), 276–282. doi:n.a.

Meadows, P., Vincent, P., & Hajduch, G. (2020). MPC-S1: S-1A & S-1B Annual Performance Report for 2019. *European Union's Copernicus Program*, *DI-MPC-APR*(MPC-0460).

MeteoBlue. (2021). Climate Bernese Alps. Date accessed: 2021-03-13. Retrieved from https://www.meteoblue.com/en/weather/historyclimate/climatemodelled/bernese-alps_switzerland_2661549

Meteoswiss Climatology. (2017). Documentation of MeteoSwiss Grid-Data Products Daily Mean , Minimum and Maximum Temperature : TabsD , TminD , TmaxD, 4–7.

Moeser, D., Mazzotti, G., Helbig, N., & Jonas, T. (2016). Water Resources Research. *Water Resources Research*, *5*(3), 1208–1226. doi:10.1111/j.1752-1688.1969.tb04897.x

Nagler, T., & Rott, H. (2000). Retrieval of wet snow by means of multitemporal SAR data. *IEEE Transactions on Geoscience and Remote Sensing*, *38*(2 I), 754–765. doi:10.1109/36.842004

Nagler, T., Rott, H., Ossowska, J., Schwaizer, G., Small, D., Malnes, E., ... Pinnock, S. (2018). Snow cover monitoring by synergistic use of sentinel-3 SLSTR and sentinel-1 SAR data. In *International geoscience and remote sensing symposium (igarss)* (pp. 8727–8730). doi:10.1109/IGARSS.2018.8518203

Nagler, T., Rott, H., Ripper, E., Bippus, G., & Hetzenecker, M. (2016). Advancements for snowmelt monitoring by means of Sentinel-1 SAR. *Remote Sensing*, *8*(4), 1–17. doi:10.3390/rs8040348

NASA. (1986). *Report of the EOS data panel*. Tech. Rep. Technical Memorandum 87777. Washington, D.C. USA. Retrieved from https://ntrs.nasa.gov/citations/19860021622

NASA. (2021a). About Terra. Date accessed: 2021-03-13. Retrieved from https://terra.nasa.gov/about

NASA. (2021b). Aqua: Project Science. Date accessed: 2021-03-13. Retrieved from https://aqua.nasa.gov/

NASA. (2021c). Landsat Science. Date accessed: 2021-03-13. Retrieved from https://landsat.gsfc.nasa.gov/landsat-8/mission-details

NASA. (2021d). MODIS: Moderate resolution imaging spectroradiometer. Date accessed: 2021-03-13. Retrieved from https://modis.gsfc.nasa.gov/about/specifications.php

Núñez-Casillas, L., Arbelo, M., Moreno-Ruiz, J. A., Hernández-Leal, P. A., Barreto, A., & Alonso-Benito, A. (2009). Relationship between sea regions with high thermal variability and wildfires from 1981 to 2008. In *International geoscience and remote sensing symposium (igarss)* (Vol. 1, pp. 236–239). doi:10.1109/IGARSS.2009.5416897

Pettinato, S., Santi, E., Paloscia, S., Aiazzi, B., & Garzelli, A. (2014). Snow cover area identification by using a change detection method applied to COSMO-SkyMed images. *Journal of Applied Remote Sensing*, *8*(1). doi:10.1117/1.JRS.8.084684

Piesbergen, J., Holecz, F., & Haefner, H. (1995). Snow cover monitoring using multitemporal ERS-1 SAR data. *International Geoscience and Remote Sensing Symposium (IGARSS)*, *3*, 1750–1752. doi:10.1109/igarss.1995.524015

Pulliainen, J. T., Mikkelä, P. J., Hallikainen, M. T., & Ikonen, J. P. (1996). Seasonal dynamics of cband backscatter of boreal forests with applications to biomass and soil moisture estimation. *IEEE Transactions on Geoscience and Remote Sensing*, *34*(3), 758770. doi:10.1109/36.499781

Rees, G. W. (2006). *Remote sensing of snow and ice* (1st Editio) (Boca Raton, Ed.). CRC Press: Taylos {\&} Francis Group.

Roebroeck, A. (2015). *Granger Causality*. doi:10.1016/B978-0-12-397025-1.00337-7

Rohner, C. (2014). Relating Snow Wetness Information Gained from the Intercantonal Measurement and Information System Stations in Switzerland to Envisat ASAR Backscatter. University of Zurich.

Rott, H., & Nagler, T. (1995). Monitoring temporal dynamics of snowmelt with ERS-1 SAR. *International Geoscience and Remote Sensing Symposium (IGARSS)*, *3*(1992), 1747–1749. doi:10.1109/IGARSS.1995.524014

Rüetschi, M., Small, D., & Waser, L. T. (2019). Rapid detection of windthrows using Sentinel-1 C-band SAR data. *Remote Sensing*, *11*(2), 1–23. doi:10.3390/rs11020115

Rutter, N., J. Sandells, M., Derksen, C., King, J., Toose, P., Wake, L., ... Sturm, M. (2019). Effect of snow microstructure variability on Ku-band radar snow water equivalent retrievals. *The Cryosphere*, *13*(11), 3045–3059. doi:10.5194/tc-13-3045-2019

Saberi, N., Kelly, R., Flemming, M., & Li, Q. (2020). Review of snow water equivalent retrieval methods using spaceborne passive microwave radiometry. *International Journal of Remote Sensing*, *41*(3), 996–1018. doi:10.1080/01431161.2019.1654144

Savitzky, A., & Golay, M. J. (1964). Smoothing and Differentiation of Data by Simplified Least Squares Procedures. *Analytical Chemistry*, *36*(8), 1639–1643. doi:10.1021/ac60214a048

Schellenberger, T., Ventura, B., Zebisch, M., & Notarnicola, C. (2012). Wet snow cover mapping algorithm based on multitemporal COSMO-skyMed X-band SAR images. *IEEE Journal of Selected Topics in Applied Earth Observations and Remote Sensing*, *5*(3), 1045–1053. doi:10.1109/JSTARS.2012.2190720

Schmidt, K., Schwerdt, M., Miranda, N., & Reimann, J. (2020). Radiometric comparison within the Sentinel-1 SAR constellation over a wide backscatter range. *Remote Sensing*, *12*(5), 1–19. doi:10.3390/rs12050854

Seager, R., Kushnir, Y., Nakamura, J., Ting, M., & Naik, N. (2010). Northern Hemisphere winter snow anomalies: ENSO, NAO and the winter of 2009/10. *Geophysical Research Letters*, *37*(14). doi:10.1029/2010GL043830

Sedgwick, P. (2012). Pearson's correlation coefficient. *BMJ (Online)*, *345*(7864), 1–2. doi:10.1136/bmj.e4483

Shaw, T. E., Gascoin, S., Mendoza, P. A., Pellicciotti, F., & McPhee, J. (2020). Snow Depth Patterns in a High Mountain Andean Catchment from Satellite Optical Tristereoscopic Remote Sensing. *Water Resources Research*, *56*(2), 1–23. doi:10.1029/2019WR024880

Shi, J., & Dozier, J. (2000). Estimation of Snow Water Equivalence Using SIR-C/X-SAR, Part II: Inferring Snow Depth and Particle. *IEEE TRANSACTIONS ON GEOSCIENCE AND REMOTE SENSING*, *38*(6), 2475–2488. doi:10.1109/36.885196

Singh, S. K., Kulkarni, A. V., & Chaudhary, B. S. (2010). Hyperspectral analysis of snow reflectance to understand the effects of contamination and grain size. *Annals of Glaciology*, *51*(54), 83–88. doi:10.3189/172756410791386535

SLF. (2021a). Description of automated stations. Date accessed: 2021-03-13. Retrieved from https://www.slf.ch/en/avalanche-bulletin-and-snow-situation/measured-values/description-of-automated-stations.html

SLF. (2021b). WSL Institute for Snow and Avalanche Research SLF. Date accessed: 2021-03-13. Retrieved from https://www.slf.ch/en/index.html

Small, D. (2011). Flattening gamma: Radiometric terrain correction for SAR imagery. *IEEE Transactions on Geoscience and Remote Sensing*, *49*(8), 3081–3093. doi:10.1109/TGRS.2011.2120616

Small, D. (2012). SAR backscatter multitemporal compositing via local resolution weighting. In *Igarss 2012* (pp. 4521–4524). doi:10.1109/IGARSS.2012.6350465

Small, D., Rohner, C., Miranda, N., Ruetschi, M., & Schaepman, M. E. (2021). Wide-Area Analysis-Ready Radar Backscatter Composites. *IEEE Transactions on Geoscience and Remote Sensing*, *future iss*(available online). doi:10.1109/tgrs.2021.3055562

Swisstopo. (2018). swissALTI3D: Das hoch aufgelöste Terrainmodell der Schweiz. *Produktinformation*, 17. Retrieved from https://www.sg.ch/bauen/geoinformation/gi/geodaten/alti/_jcr_content/Par/sgch_accordion_list/AccordionListPar/sgch_accordion/AccordionPar/sgch_

downloadlist / DownloadListPar / sgch _ download _ copy. ocFile / Swisstopo _ SwissALTI3D _ Produktbeschreibung.pdf

Tedesco, M., & Narvekar, P. S. (2010). Assessment of the NASA AMSR-E SWE Product. *IEEE Journal of Selected Topics in Applied Earth Observations and Remote Sensing*, *3*(1), 141–159. doi:10.1109/JSTARS.2010.2040462

Truckenbrodt, J., Freemantle, T., Williams, C., Jones, T., Small, D., Dubois, C., ... Giuliani, G. (2019). Towards sentinel-1 SAR analysis-ready data: A best practices assessment on preparing backscatter data for the cube. *Data*, *4*(3). doi:10.3390/data4030093

Tsai, Y. L. S., Dietz, A., Oppelt, N., & Kuenzer, C. (2019). Remote sensing of snow cover using spaceborne SAR: A review. *Remote Sensing*, *11*(12). doi:10.3390/rs11121456

Varade, D., Maurya, A. K., Dikshit, O., Singh, G., & Manickam, S. (2020). Snow depth in Dhundi: an estimate based on weighted bias corrected differential phase observations of dual polarimetric bi-temporal Sentinel-1 data. *International Journal of Remote Sensing*, *41*(8), 3031–3053. doi:10.1080/01431161.2019.1698076

Viera, A. J., & Garrett, J. M. (2005). Understanding interobserver agreement: the kappa statistic. *Family Medicine*, *37*(5), 360–363. doi:n.a.

Vögtli, M., Small, D., & de Jong, R. (2018). Land surface dynamics of the Canadian Arctic Archipelago and adjacent Greenland observed using optical and SAR time series Land surface dynamics of the Canadian Arctic Archipelago and adjacent Greenland observed using optical and SAR time series. University of Zurich.

Vreugdenhil, M., Navacchi, C., Bauer-Marschallinger, B., Hahn, S., Steele-Dunne, S., Pfeil, I., ... Wagner, W. (2020). Sentinel-1 cross ratio and vegetation optical depth: A comparison over Europe. *Remote Sensing*, *12*(20), 1–19. doi:10.3390/rs12203404

Wendleder, A., Dietz, A. J., & Schork, K. (2018). Mapping snow cover extent using optical and SAR data. In *International geoscience and remote sensing symposium* (pp. 5104–5107). doi:10.1109/IGARSS.2018.8518374

Winstral, A., Magnusson, J., Schirmer, M., & Jonas, T. (2019). The Bias-Detecting Ensemble: A New and Efficient Technique for Dynamically Incorporating Observations Into Physics-Based, Multilayer Snow Models. *Water Resources Research*, *55*(1), 613–631. doi:10.1029/2018WR024521

Wulf, H., Sassik, B., Milani, G., & Leiterer, R. (2020). High-resolution snow depth monitoring for entire mountain ranges. In *7th swiss conference on data science, sds 2020* (pp. 41–46). doi:10.1109/SDS49233.2020.00008

Würzer, S., & Jonas, T. (2018). *Spatio-temporal aspects of snowpack runoff formation during rain on snow*. doi:10.1002/hyp.13240

Zhou, C., & Zheng, L. (2017). Mapping radar glacier zones and dry snow line in the antarctic peninsula using Sentinel-1 images. *Remote Sensing*, *9*(11), 1–19. doi:10.3390/rs9111171

A Appendix

A.1 Time series at 100 m GSD

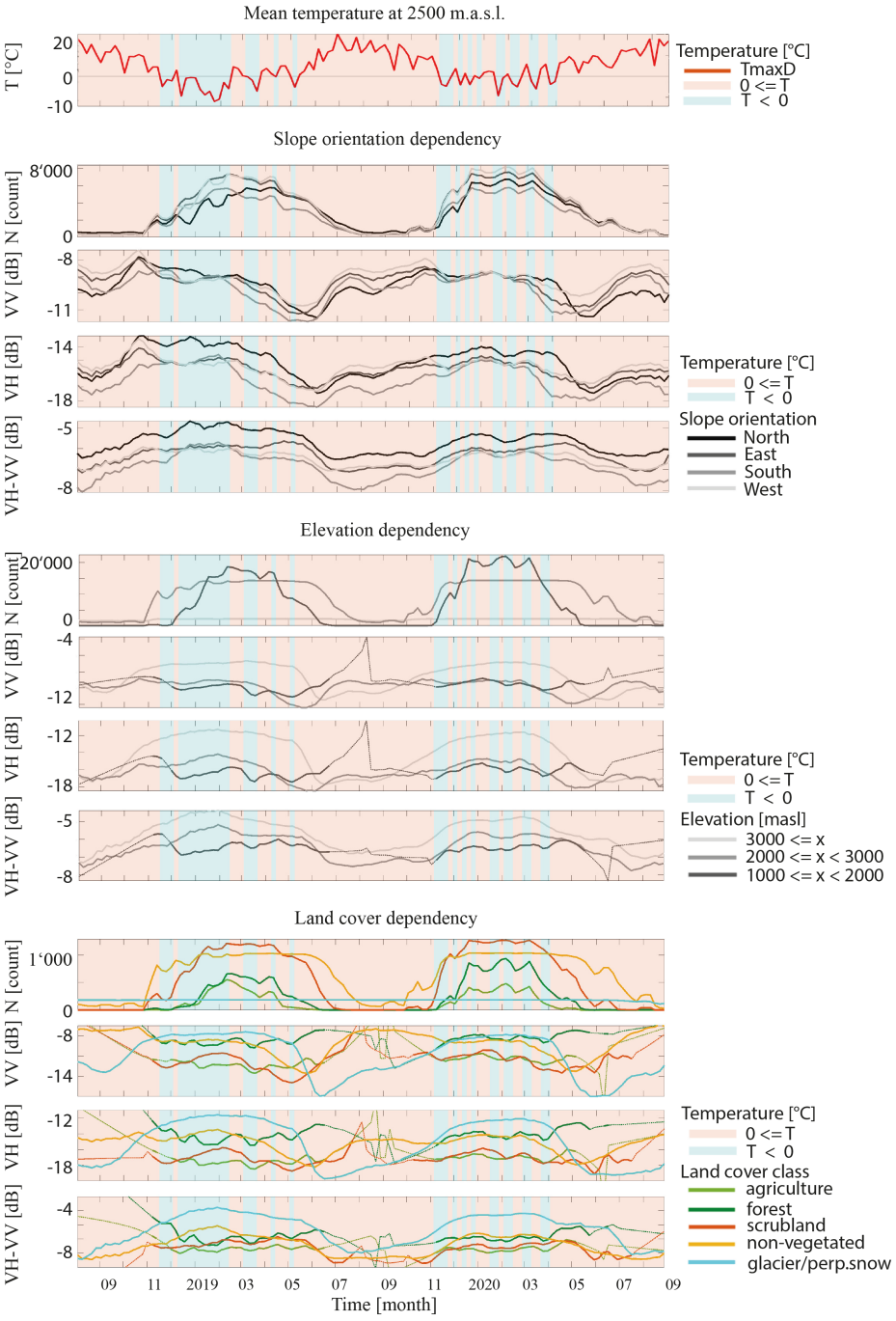

FIGURE A.1: Mean time series (Sept. 2018 to Sept. 2020) of S1 backscatter for snow-covered pixels in dependency of 1) aspect orientation (subplots ii-v), 2) elevation (subplots vi-ix) and 3) land cover class (subplots x-xiii) at 100 m GSD. First subplot shows the mean 2500 m temperature over time. The shading for all subplots is based on this temperature in relation to freezing point during the S1 acquisitions.

A.2 Median of three reference images at 30 and 1000 m GSD

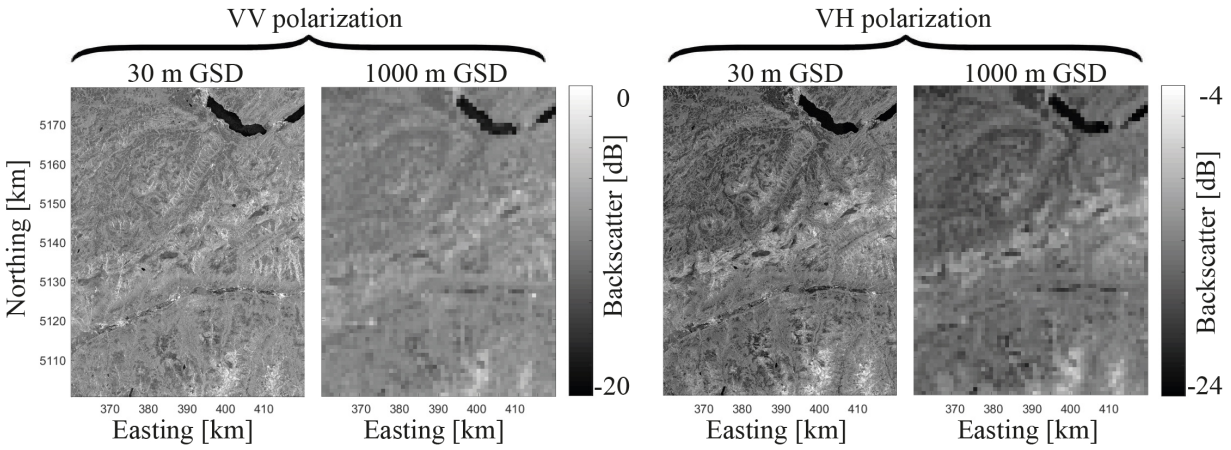

FIGURE A.2: Reference images based on median of three approach. The displayed examples show VV- and VH-polarization at 30 and 1000 m GSD.

A.3 Reference images at 100 m GSD

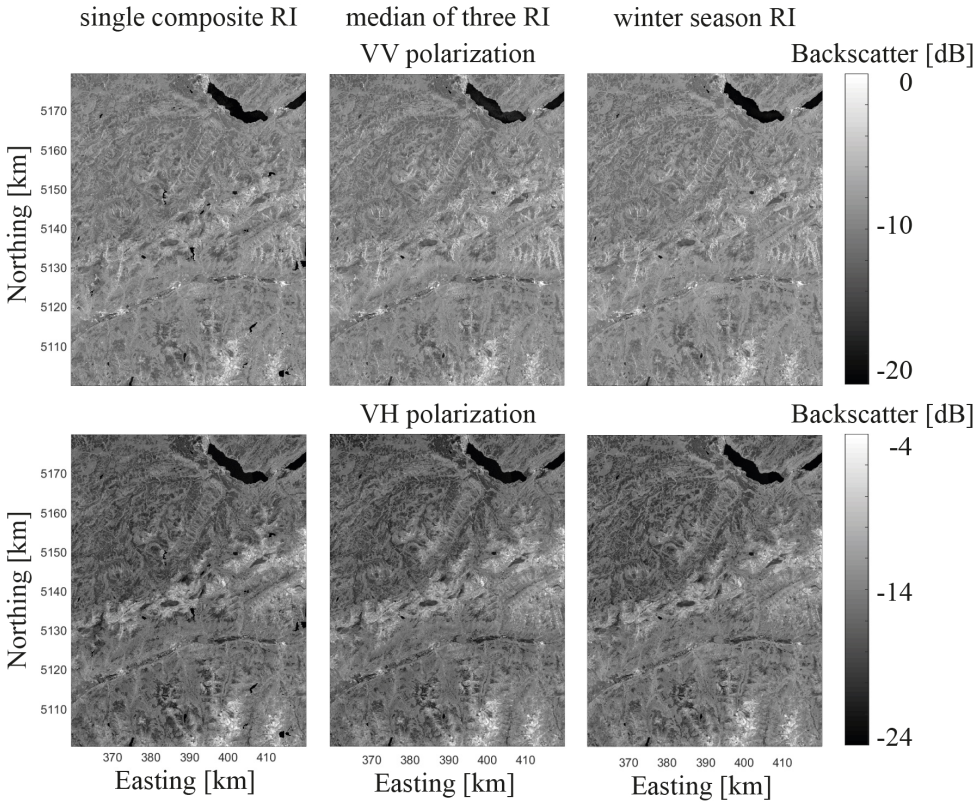

FIGURE A.3: Reference images based on a single composite, median of three and median of winter season approach. The displayed examples show VV- and VH-polarization at 100 m GSD.

A.4 Statistics at 1000 m GSD at VV-polarization

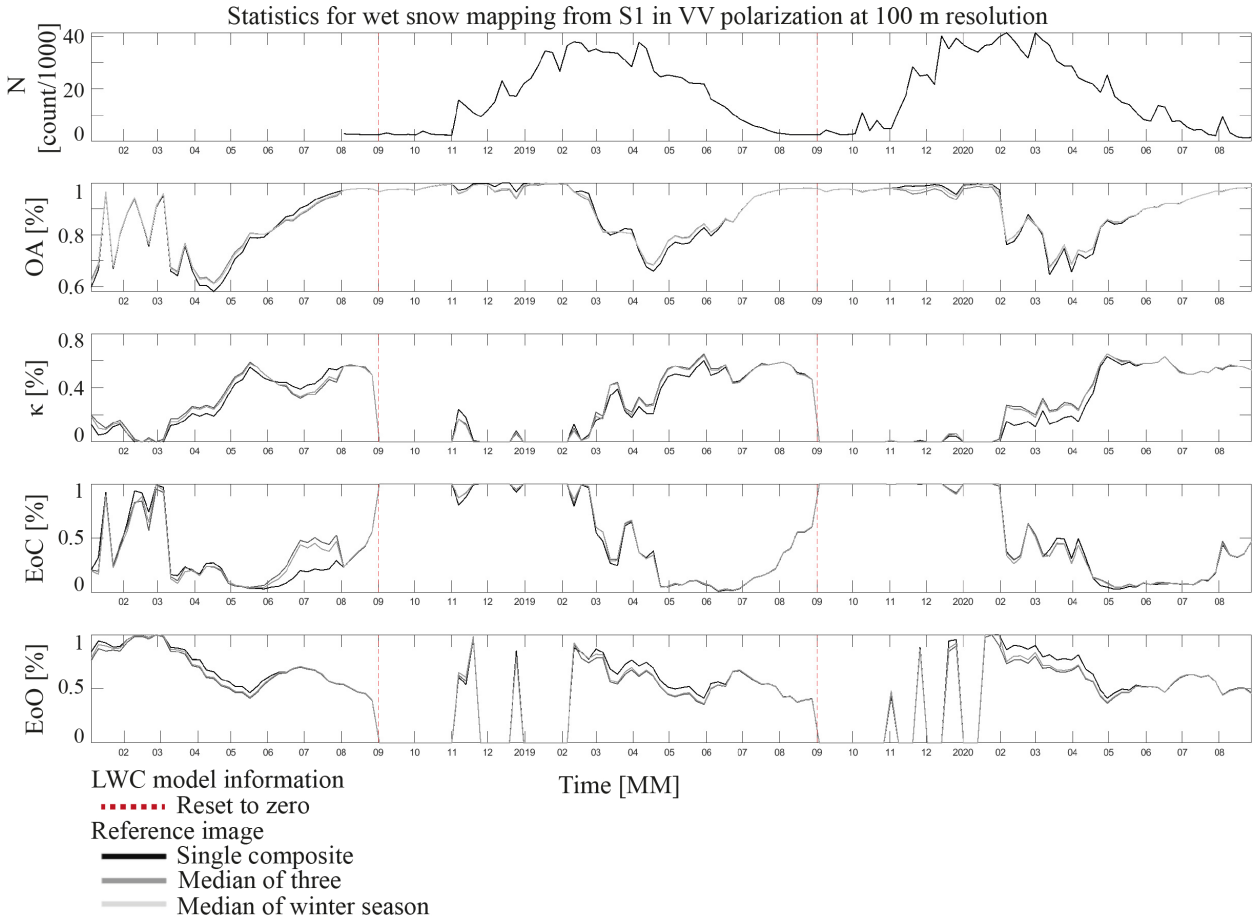

FIGURE A.4: Achieved statistics over time in VV mode in comparison to the number of snow covered pixels from optical imagery at 100 m GSD. Displayed are the temporal behaviours of the overall accuracy (OA), Cohen's kappa coefficient (κ), error of omission (EoO) and error of commission (EoC) at 1000 m GSD using VV-polarized S1 data for wet snow retrieval.

A.5 Statistics at 1000 m GSD at VH-polarization

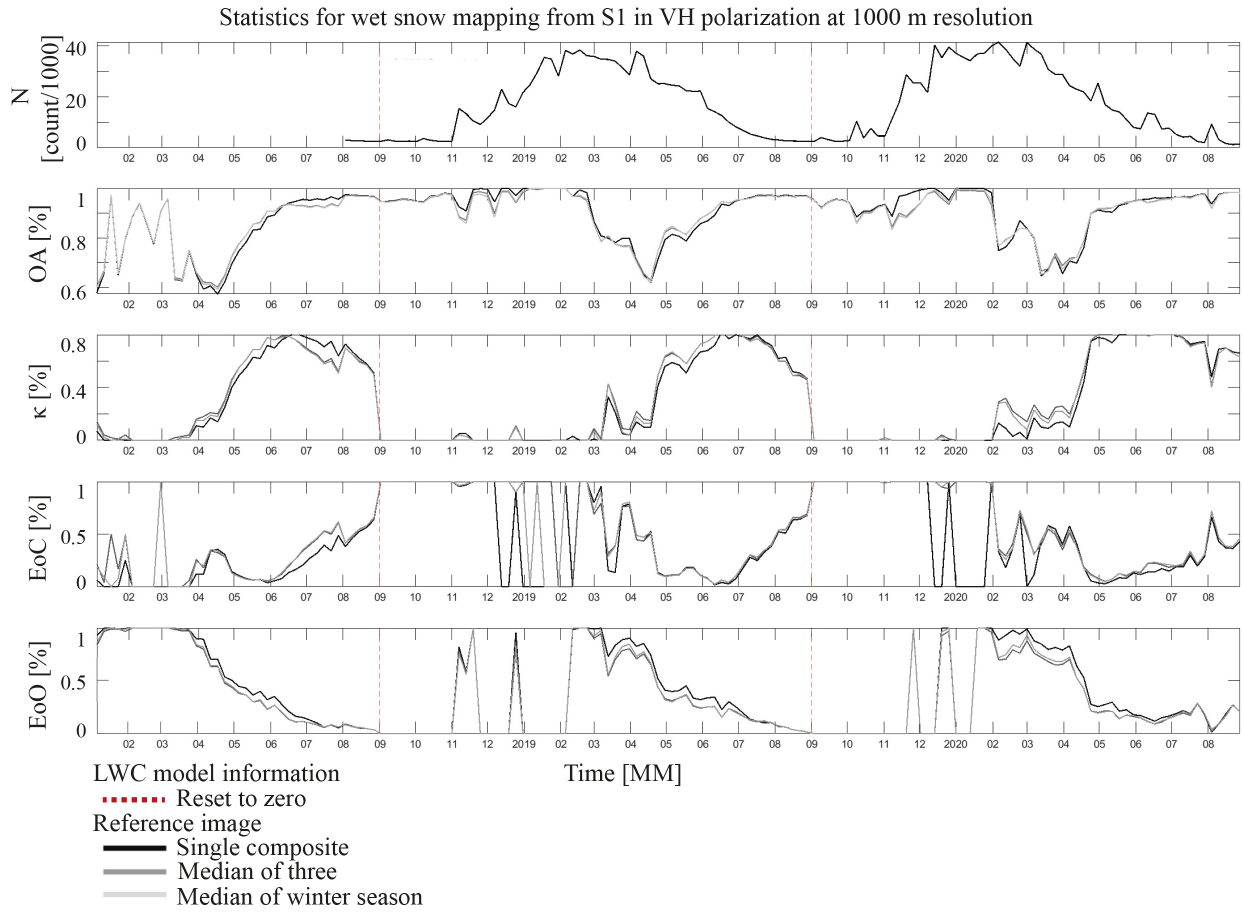

FIGURE A.5: Achieved statistics over time based on VH LRW composites in comparison to the number of snow covered pixels from optical imagery at 1000 m GSD. Displayed are the temporal behaviours of the overall accuracy (OA), Cohen's Kappa coefficient (κ), error of omission (EoO) and error of commission (EoC) at 1000 m GSD.

A.6 Snow depth retrieval at 1000 m GSD including snow free composites

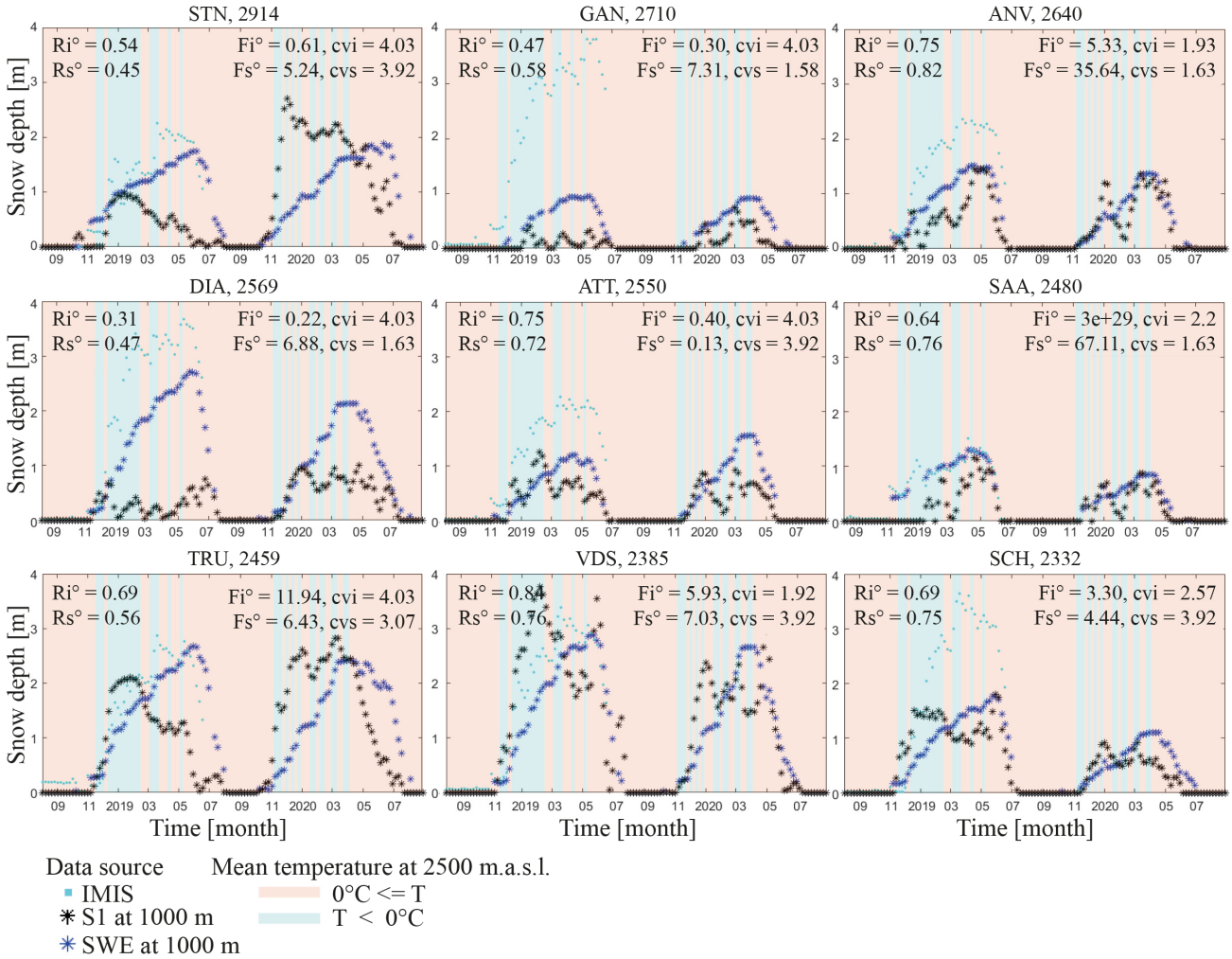

FIGURE A.6: Snow depth time series retrieved from S1 backscatter, calculated from intermediate snow water equivalent estimate (both at 1000 m GSD) vs. values measured at IMIS stations (point measurements) in comparison. Each subplot represents an IMIS measurement location (station short name, elevation in m.a.s.l.): Stations are sorted by elevation. The shading colour indicates the daily maximum temperature at 2500 m.a.s.l. in relation to freezing point (red above, blue below, more information see 2.8). Top-left boxes depict the achieved Pearson Correlation Coefficients between the S1-based snow depth retrieval and the local snow depth measured at the IMIS station (Ri), and to snow depth calculated from SWE (Rs; SLF, 2021b). Top-right boxes display the calculated Granger test: F-score ($F°$) and critical value (cv) for corresponding comparisons. As marked by $°$ R and F values were calculated across the entire time series including snow free images (mask was based on optical imagery ExoLabs, 2021).

A.7 Snow depth retrieval at 100 m GSD including snow free composites

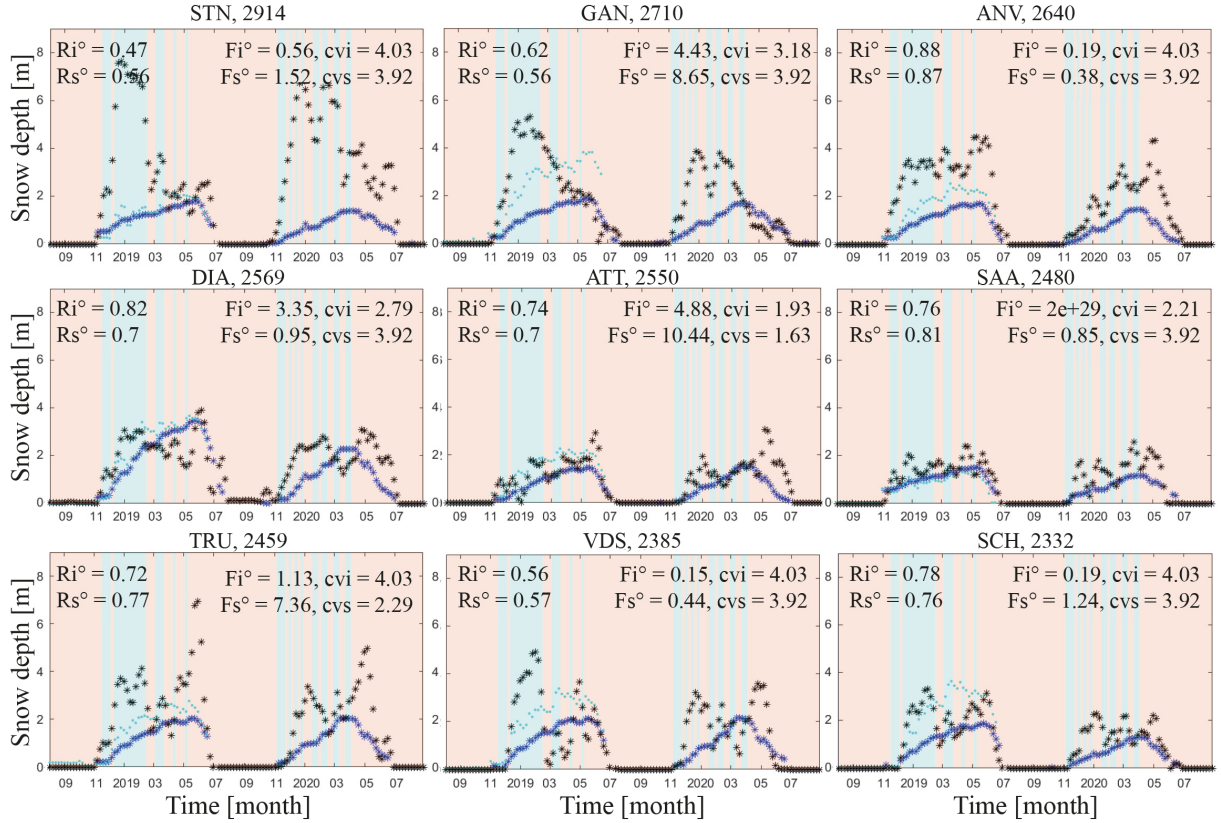

FIGURE A.7: Snow depth time series retrieved from S1 backscatter, calculated from intermediate snow water equivalent estimate (both at 1000 m GSD) vs. values measured at IMIS stations (point measurements) in comparison. Each subplot represents an IMIS measurement location (station short name, elevation in m.a.s.l.): Stations are sorted by elevation. The shading colour indicates the daily maximum temperature at 2500 m.a.s.l. in relation to freezing point (red above, blue below, more information see 2.8). Top-left boxes depict the achieved Pearson Correlation Coefficients between the S1-based snow depth retrieval and the local snow depth measured at the IMIS station (Ri), and to snow depth calculated from SWE (Rs; SLF, 2021b) including zero values. Top-right boxes display the calculated Granger test: F-score ($F°$) and critical value (cv) for corresponding comparisons. As marked by $°$ R and F values were calculated across the entire time series including snow free images (mask was based on optical imagery ExoLabs, 2021).

Personal Declaration

I hereby declare that the submitted thesis is the result of my own, independent work. All external sources are explicitly acknowledged in the thesis.

Place, Date
Staefa, March 30, 2021

Signature